CHEMICAL AND STATISTICAL SOOT MODELING

A DISSERTATION
SUBMITTED TO THE DEPARTMENT OF MECHANICAL ENGINEERING
AND THE COMMITTEE ON GRADUATE STUDIES
OF STANFORD UNIVERSITY
IN PARTIAL FULFILLMENT OF THE REQUIREMENTS
FOR THE DEGREE OF
DOCTOR OF PHILOSOPHY

Guillaume Blanquart

March 2008

I certify that I have read this dissertation and that, in my opinion, it is fully adequate in scope and quality as a dissertation for the degree of Doctor of Philosophy.

(Heinz Pitsch) Principal Adviser

I certify that I have read this dissertation and that, in my opinion, it is fully adequate in scope and quality as a dissertation for the degree of Doctor of Philosophy.

(Rodney O. Fox)

I certify that I have read this dissertation and that, in my opinion, it is fully adequate in scope and quality as a dissertation for the degree of Doctor of Philosophy.

(Ronald K. Hanson)

Approved for the University Committee on Graduate Studies.

Acknowledgement

First, I would like to thank my advisor Professor Pitsch for his support and guidance in my research. Then, I would like to thank the members of my reading committee, Professor Hanson and Professor Fox, for their comments. Finally, I would like to acknowledge the financial support from the Department of Energy under its Advanced Simulation and Computing (DOE-ASC) program.

Abstract

The combustion of pretroleum based fuels like kerosene, gasoline, or diesel leads to the formation of several kind of pollutants. Among them, soot particles are particularly bad for their severe consequences on human health. Over the past decades, strict regulations have been placed on car and aircraft engines in order to limit these particulate matter emissions. Designing low emission engines requires the use of predictive soot models which can be applied to the combustion of real fuels.

Towards this goal, the present work addresses the formation of soot particles both from a chemical and statistical point of view. As a first step, a chemical model is developed to describe the formation of soot precursors from the combustion of several components typically found in surrogates, including *n*-heptane, iso-octane, benzene, and toluene. The same mechanism is also used to predict the formation of large Polycyclic Aromatic Hydrocarbons (PAH) up to cyclopenta[cd]pyrene ($C_{18}H_{10}$).

Then, a new soot model which represents soot particles as fractal aggregates is used. In this model, a soot particle is described by three variables: its volume (V), its surface area (S), and the number of hydrogen sites on the surface (H). The Direct Quadrature Method of Moments (DQMOM) is used as a precise representation of the population of soot particles which includes small spherical particles and large aggregates. This model is shown to predict accurately the formation of soot in a wide range of flames including premixed and counterflow diffusion flames, low and high temperature flames and for a wide range of fuels from ethylene to iso-octane. Finally,

this model predicts several aggregate properties like the primary particle diameter and gives insight into the reactivity of the soot surface.

Contents

List of Tables

List of Figures

Chapter 1

Introduction

The transportation of people and goods across countries remains highly dependent upon the combustion of petroleum based fuels. Aircraft engines are powered with kerosene fuels, while car and truck engines are using gasoline or diesel fuels. The combustion of these petroleum based fuels leads to the formation of several kinds of pollutants, among which are soot particles. These black particles are known to be the source of severe health problems. For instance, they can cause heart diseases or lung cancer. Because of their adverse effects on human health, severe resctrictions have been placed upon particulate matter (PM) emissions from car or aircraft engines. Future regulations will limit even more the emission of poluttants from these engines, and will require the engine manufacturers to provide detailed information on the particulate matter produced by these engines.

These particles are not only formed in automotive and aircraft engines, but also in industrial furnaces and in fires. They are usually the sign of incomplete and inefficient combustion. Sometimes, soot particles might even be a key operating component of certain furnaces, where soot enhances heat transfer. A better description of the combustion of these fuels and the mechanisms leading to the formation of soot particles is required to reduce more efficiently soot emmissions in engines or other industrial

devices.

1.1 Combustion of Real Fuels

The fuels used both in aircraft (kerosene) and car engines (gasoline and diesel) are composed of a multitude of different molecular components. These components vary in molecular weight and exhibit very different structures. Modeling all the physical and chemical properties of real fuels is challenging as the entire detailed molecular composition of these fuels is not fully known. As a consequence, real fuels are represented typically by surrogates [34]. In this approach, a blend of simple hydrocarbons molecules is used, which could reproduce certain physical properties, such as boiling points and liquid density, or chemical properties, such as ignition delay times, laminar burning velocities, or the formation of pollutants, of the real fuels. Among these species, are linear alkanes like *n*-heptane (C_7H_{16}), *n*-decane ($C_{10}H_{22}$), branched alkanes like iso-octane (C_8H_{19}), cyclic alkanes like cyclohexane (C_6H_{12}), and aromatics like benzene (C_6H_6), toluene (C_7H_8), or naphthalene (C_8H_{10}).

Soot constitutes one of the main pollutants produced in the combustion of fuels like diesel, gasoline, or kerosene. Formulating a kerosene surrogate to describe the formation of soot particles remains a major challenge as limited experimental measurements of soot have been performed in kerosene flames. In fact, most of the soot measurements have been performed with single component fuels like *n*-heptane [7, 81, 1, 41]. Other soot measurements include flames with iso-octane [7], *n*-decane [43], benzene [185, 3], or toluene [186, 1]. On the other hand, several experimental measurements have been focused on analyzing the effects of additives on the sooting point [139] or the yield sooting indices [113]. For instance, aromatic species (like benzene and toluene) were found to produce more soot than aliphatic species (like *n*-heptane and iso-octane). The effects of oxygenated additives like dimethyl-ether

(DME), acetone, butanal, and pentanone have been investigated recently by Hong et *al.* [77]. However, direct experimental measurements of soot yield in kerosene flames are scarce. Recently, Honnet et *al.* [78] have measured soot volume fraction in counterflow diffusion flames of kerosene with different strain rates. They compared their experimental data with numerical simulations using *n*-decane and trimethylbenzene as a surrogate.

1.2 Underlying Chemistry

Modeling soot formation from the combustion of these different fuel components generally relies on using a detailed chemical mechanism coupled with a soot model [5, 111]. The chemical mechanism, depicted in Fig. 1.1 describes the decomposition of the different molecular components, the oxidation of the smaller species, and the formation of larger hydrocarbon molecules. Among these larger hydrocarbon molecules, Polycyclic Aromatic Hydrocarbons (PAH) play a major role, as they are generally assumed to be soot precursors [161, 201].

Most models consider that these incipient molecules originate in benzene and grow by addition of carbon atoms following the H-abstraction C_2H_2-addition (HACA) mechanism [59]. The same mechanism is usually used to represent the chemical reactions taking place on the surface of the soot particles. In this framework, benzene molecules are very important as precursors for larger PAHs. At the same time, acetylene species play a major role as the main building block for the growth of both PAH molecules and soot particles. Recently, new experimental [113] and numerical [117, 42] studies have suggested the importance of propargyl (C_3H_3) and allyl radicals (C_3H_5) in the formation of benzene and the growth of larger PAH molecules. Because of their importance to soot formation, these species are referred to as soot precursors. Understanding the formation mechanisms of these soot precursors from

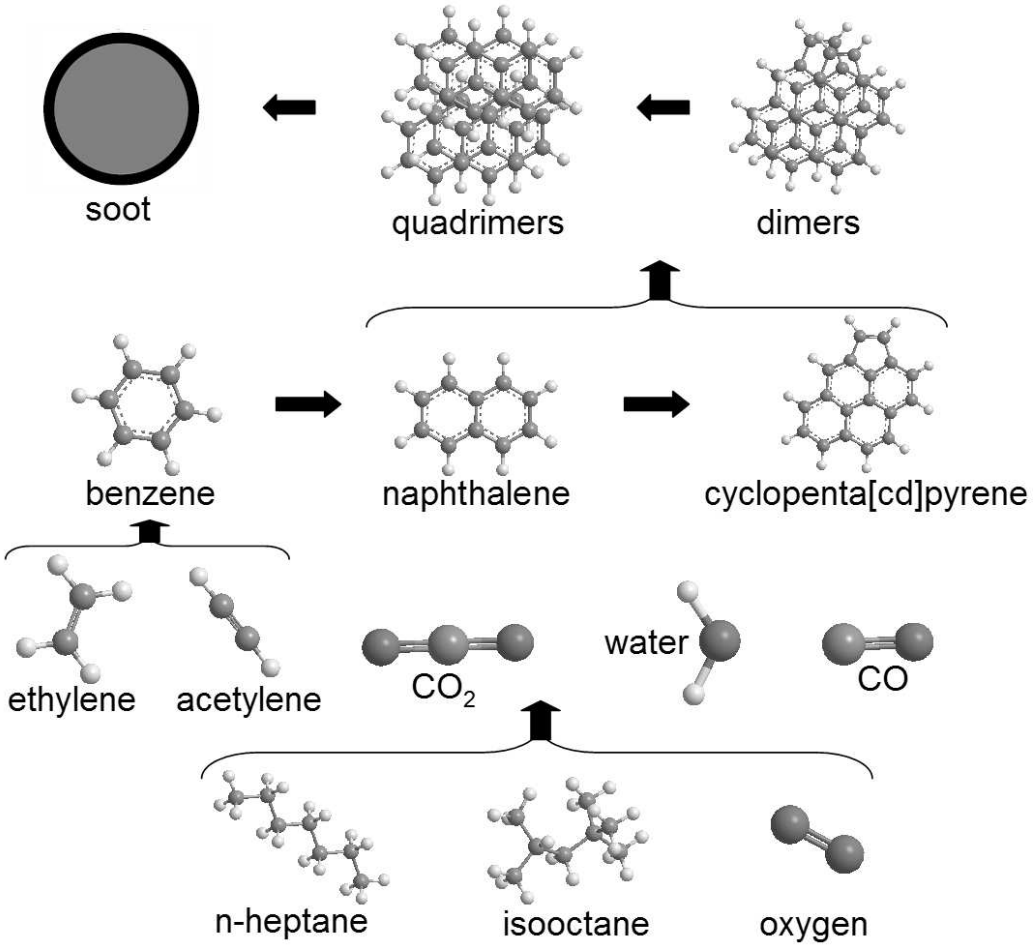

Figure 1.1: Sketch of the main pathways from the fuel components to the formation of the first soot particle.

the combustion of real fuels is very important in modeling soot formation.

One of the purposes of the present work is to develop a unique chemical mechanism for high temperature combustion of both small and larger hydrocarbons while predicting soot precursors with good accuracy. The mechanism focuses on smaller hydrocarbons like methane (CH_4), acetylene (C_2H_2), ethylene (C_2H_4) and ethane (C_2H_6) as most of the modeling of soot formation has been performed with these fuels. Additional hydrocarbons like propyne (C_3H_4), propene (C_3H_6), propane (C_3H_8) and butadiene (C_4H_6) are also considered as their decomposition will lead to radicals (propargyl C_3H_3, allyl C_3H_5 and butadienyl C_4H_5) involved in the formation of the first aromatic ring. Finally, two alkanes, one normal (*n*-heptane) and one branched (iso-octane) as well as two aromatic species (benzene and toluene) are chosen as representative candidates of components found in surrogate fuels.

1.3 Polycyclic Aromatic Hydrocarbons

The same chemical mechanism used to describe combustion of the fuel and the formation of benzene is used to represent the growth of larger hydrocarbons. During the growth by chemical reactions, additional six-membered rings as well as new five-membered rings are formed. These five-membered ring molecules, commonly referred to as cyclopentafused PAH (CP-PAH), are formed generally by direct cyclization after addition of acetylene (C_2H_2) on radicals like naphthyl. However, the same reaction of acetylene addition can also lead to stable ethynyl-substituted aromatics. In a flame, an equilibrium is established quickly between the CP-PAH and the ethynyl-substituted aromatics. Recent work by Marsh and Wornat [110] shows that CP-PAH should be formed preferentially in comparison to the ethynyl-substituted aromatics when the path is available. Also, branching ratios have been found to be largely in favor of the direct cyclization reaction at high temperature and for a wide

range of pressures [154]. Those results suggest that the main path from benzene to higher PAH involves the formation of acenaphthylene and other CP-PAH. While the path to form acenaphthylene from naphthalene was included in some of the recent soot mechanisms [5], growth beyond acenaphthylene to form larger CP-PAH (like acephenanthrylene or cyclopenta[cd]pyrene) was not considered. However, adding this path to existing reaction mechanisms is not straightforward because of the lack of kinetics and thermodynamic properties.

Similar to the combustion of the different fuels and the formation of soot precursors, the evolution of PAH from benzene up to the nucleation into soot particles is typically described using detailed chemical kinetic reaction mechanisms. Modeling soot formation therefore requires the knowledge of the underlying PAH chemistry, which itself relies on the thermodynamic properties of the aromatic species. A quite comprehensive database of thermodynamic properties of PAH has been developed by Wang and Frenklach [196]. They used the AM1 level of theory with additional group corrections to predict the enthalpies of formation. While their database is already extensive, it does not include cyclopentafused molecules above acenaphthylene ($C_{12}H_8$). Wang and Frenklach [196] also noted some inaccuracies in predictions of the vibrational frequencies used for the computation of heat capacities and entropies. Finally, the planarity of some of the molecules was not discussed, and corrections for internal degrees of rotation (hindered rotors) were not included.

To overcome the other above-mentioned shortcomings, a new database for thermodynamic properties of PAH is developed and is available in the Appendix. This database expands the range of molecules considered by Wang and Frenklach [196], and includes molecules both with and without five-membered rings. These species are chosen on the basis of their relevance for soot formation mechanisms.

1.4 Soot Particles

Experimental observations [98, 82] suggest that soot particles are aggregates, and are composed of a certain number of small spherical particles, called primary particles. These primary particles are arranged in ways to produce fractal shaped soot aggregates. These aggregates are formed from the mutual collision of spherical soot particles or other soot aggregates.

The fractal dimension of soot aggregates has been studied in detail both experimentally and numerically. This fractal dimension describes how fast the size of an aggregate increases with increasing number of primary particles. If n is the number of spheres composing the aggregate, the size of the aggregate is proportional to n^{1/D_f}. Mitchell and Frenklach [123, 124] studied the coagulation of spherical particles onto a so called collector particle. The work was performed in the free molecular regime with the incoming candidate particles having random ballistic trajectories characteristic of small particles (or large Knudsen number Kn $\gg 1$). The results showed that in the limit of no surface reaction, the aggregates have a very compact structure with a rather high fractal dimension $D_f \approx 2.97$, close to the results of the early work of Meakin et *al.* [114] ($D_f \approx 3.09$). However, the fractal dimension determined by these simulations is much higher than any of the experimental values, which range from 1.6 to 1.9 [98, 82]. In fact, the assumption that every collision leads to an aggregate might not be valid. The colliding particles used in those simulations were very small, with diameters of only a few nanometers and below. Recent experimental studies of soot morpholgy and composition [204] suggest that such small soot particles have a liquid-like character. This would imply that the collision of two small soot particles will lead to the formation of a larger spherical particle, rather than an aggregate consisting of two spheres.

More recently, high fidelity simulations of cluster-cluster aggregation were performed [104, 159]. Schmid et al. [159] considered coagulation and sintering in the so-called Diffusion Limited Cluster Aggregation (DLCA) regime, which is equivalent to the continuum regime characterized by Brownian random diffusion (small Knudsen number Kn $\ll$1). They found that in the limit of no sintering, the fractal dimension reaches a value close to $D_f \approx 1.86$. Köylü *et al.* [98] studied the fractal dimension of soot aggregates from turbulent non-premixed flames of acetylene, propylene, ethylene, and propane. Their measurements for the fractal properties of soot yield $D_f = 1.82$. A more recent analysis of soot fractal properties in JP-8 pool fires [82] revealed slightly lower values for the fractal dimension $1.68 < D_f < 1.72$. Most of the experimental measurements were performed on relatively large soot aggregates with primary particle diameters ranging from 20 to 70 nm, and number of primary particles reaching hundreds or thousands.

Over the years, several attempts have been made to model soot aggregates. The transition from small spherical particles to larger aggregates with more complex structure is typically described in an empirical way by specifying the diameter where this transition occurs [5, 88]. Below that presumed threshold diameter, soot particles are assumed to be spherical, while beyond this diameter, they are assumed to be aggregates. This approach of aggregation is limited, as it cannot accurately describe a typical population of soot particles, where small spherical particles and large aggregates coexist [204]. Recently, Balthasar and Frenklach [9] and Patterson and Kraft [141] introduced a model representing soot aggregates by their surface and volume. The aggregate morphology is typically described with a shape descriptor variable. This model has been formulated in the framework of Monte-Carlo (MC) simulations in order to simulate with great accuracy the entire population of soot particles. While this model allows for a better description of soot particles, a coherent coagulation model which spans the full spectrum from coalescence to aggregation is difficult to

formulate. This approach remains promising and great emphasis should be placed upon comparing the diameters of the primary particles with experiments.

During its formation, the aggregate shape of a soot particle is affected by the addition of mass onto the surface through chemical reactions. The concept of active surface sites has been applied by Frenklach and Wang [59] to describe the reactivity of the surface in the HACA mechanism. It has since been used in different soot models in the description of soot mass growth by heterogeneous surface reactions. Most soot models assume a given density of sites per unit soot surface (about $\chi \approx 2.3 \times 10^{19}\,\mathrm{m}^{-2}$), and introduce a parameter α, which describes the fraction of active sites. Appel *et al.* [5] expressed the parameter α as a decreasing function of the local temperature and the first size moment of the soot particle distribution. The fit was empirically determined from a least square approach. More recently, Singh *et al.* [176] introduced an equation for the number of active sites per surface area. This relaxation equation assumes that the surface reactivity starts at $\chi_0 = 2.3 \times 10^{19}\,\mathrm{m}^{-2}$ in the inception zone and decreases with residence time in the flame towards a limiting value of $\chi_\infty = 4.6 \times 10^{18}\,\mathrm{m}^{-2}$. The surface reactivity of the first soot particles appear to be overpredicted by this model, as a rough estimation for a pyrene dimer gives $\chi_{\mathrm{dimer}} = 8 \times 10^{18}\,\mathrm{m}^{-2}$. A more detailed description of the reactivity of the surface of soot particles is needed to predict with good accuracy soot concentrations and properties in a large diversity of flames. Furthermore, small spherical and large soot aggregates might not exhibit the same reactivity towards chemical reactions.

A consistent representation of the Particle Size Distribution Function (PSDF) of soot is necessary for an accurate prediction of the soot volume fraction or aggregate properties. Monte-Carlo (MC) simulations has been shown to predict with good accuracy the full PSDF of soot [176, 175]. Results from DSMC also compared favorably with experimental measurements of the PSDF from laminar ethylene flames [205, 206]. However, the inherent cost of using DSMC for such simulations renders impossible

its use for 3D or even 1D simulations. Recently, Marchisio and Fox [108] applied the Direct Quadrature Method of Moments to soot formation. Rather than assuming the full form of the PSDF or simulating it completely, this method approximates the PSDF by a series of delta functions. This method proved to be effective in predicting the main moments of the PSDF, such as the volume, the surface area, and the number density. Furthermore, this method was found to be inexpensive in comparison to DSMC.

In this work, a new soot model is presented that introduces a more general description of the PSDF, and which therefore allows for addressing several of the issues mentioned above. The model describes a soot particle with three independent parameters, the particle volume, the particle surface, and the number of hydrogenated surface sites. This model provides

- a coherent aggregation model with a particular treatment of sphere-sphere and sphere-cluster collisions,
- a more detailed description of the surface reactivity of soot particles,
- and a statistical representation of soot particles, which allows for bimodal particle size distribution functions.

1.5 Temperature Effects on Soot

The formation of soot particles depends on a wide range of parameters including temperature, pressure, and fuel type. Temperature plays a particularly important role among these parameters. Several experimental measurements, both in laminar premixed flames [17, 18, 206] and in shock tubes [90, 96, 77], have shown that soot volume fraction exhibits a so-called "bell shaped" curve as a function of temperature. At low temperatures, soot volume fraction increases with increasing temperature.

Then, beyond a certain threshold temperature, the soot volume fraction decreases as the temperature is further increased. This threshold temperature has been found to be a function of the fuel and ranges from about 1575 K for benzene/air ($\phi = 1.85$) [17], up to 1750 K for heptane/O_2/Ar ($\phi = 5.0$) [77].

Over the years, several models have been developed to interpret the temperature dependance of the soot volume fraction. Early on, surface reactions were identified as crucial in predicting the soot volume fraction decay at high temperature. To accurately predict soot volume fraction for a series of laminar premixed flames, Kazakov and Frenklach [89] introduced a parameter α that multiplies the rate of growth by surface reactions. This parameter, interpretated as the ratio of active sites to the total number of sites found on the surface of a soot particle, was originally fitted as a function of the flame temperature. Later, Appel *et al.* [5] further refined the dependence of α on the flame properties. They were able to predict the soot volume fraction for a large set of laminar premixed flames by fitting α as a function not only of the flame temperature but also of the size of a soot particle. Other attempts [35, 111] considered the reaction of acetylene addition in the HACA mechanism to be reversible. The competition of the subsequent ring closure with the reverse reaction introduces a new temperature dependence characterized by the difference in the activation energy of both reactions. As a consequence, the effective rate of mass addition is reduced at high temperatures.

Several experimental measurements have been performed on laminar premixed flames in both the low and high temperature regimes to analyze the differences in soot formation. Zhao *et al.* [204] found that soot particles formed from low temperature flames exhibit a small carbon-to-hydrogen ratio (C/H) close to that of typical PAH molecules found in flames (from C/H = 1 for benzene to C/H = 1.6 for pyrene). Harris and Weiner [69] measured the carbon-to-hydrogen ratio in flames with higher

temperatures. They found that the particles became more carbonized (larger C/H ratio) with higher residence time in the flame. Measurements of the carbon-to-hydrogen ratio of soot particles have also been performed in turbulent flames. Jensen *et al.* [83] studied soot morphology and chemistry in liquid pool fires. They found that the C/H ratio increases from C/H = 4 (at 2 m above the pool) to about C/H = 8 (at 4 m above the pool). They postulated that carbonization of soot particles could have been caused by going through high temperature regions.

One of the final goals of the present work is to analyze the effects of temperature on soot formation. This analysis will be performed with the detailed soot model mentioned previously. This model is enhanced by a model for the C/H ratio of the soot particles, and will try to explain some of the experimental findings both at low and high temperatures.

Chapter 2

Chemical model

The description of combustion processes like the decomposition of the different fuel components, the oxidation of the smaller hydrocarbon species and the formation of large Polycyclic Aromatic Hydrocarbons (PAH), relies on the use of a detailed chemical kinetic mechanism. This mechanism is composed of a large set of elementary reactions. These different reactions may represent the fragmentation of a molecule, the recombination of two radicals, or the exchange of one or several atoms between two chemical species. Each of these reactions is assigned a rate constant which describes the rate of change of the different species concentration due to the given reaction.

Also part of the chemical model, the thermodynamic properties describe the evolution of the enthalpy of the chemical species with temperature. These properties are used to compute the heat realease and the equilibrium constant of the different reactions. This last part is of particular importance for PAH molecules as it is crucial to accurately represent the relative distribution of the different PAH species with temperature. In fact, the thermodynamic properties of PAH molecules describe how energetically favorable the different reaction pathways are, and thus will influence significantly the chemical model.

The present section is structured as follows. First, as the entire chemical model

relies on thermodynamic properties, the thermodynamic properties of all PAH species under considerations are revisited and recomputed. Then, in the second section, the chemical mechanism is presented. Finally, the full chemical model is tested against a large set of experimental cases in order to validate its ability to predict soot precursors.

2.1 Thermodynamic Properties of PAH

In this section, a new database for thermodynamic properties of PAH is developped. This database expands the range of molecules considered by Wang and Frenklach [196], and includes molecules both with and without five-membered rings. The species are chosen on the basis of their relevance for soot formation mechanisms.

The thermodynamic properties like heat capacity (C_p°), entropy (S°), or heat of formation ($\Delta_f H^\circ$) of a chemical species depend on the geometric structure of the given species. Here, ab initio quantum calculations are used to find the optimum geometric structure corresponding to the ground state of that species.

Geometric structures are first optimized at various levels of theory and with various basis sets. The shapes of the molecules as well as their planarity are discussed. Molecules with internal degrees of freedom are further analyzed, and torsional potentials are derived. From the best optimized geometric structure (B3LYP/6-31++G(d,p)), thermodynamic properties such as heat capacity and entropy are derived. Then, the enthalpies of formation of these species are computed with the mixed method G3MP2//B3. Finally, a group correction is applied to improve the accuracy of the computed energies.

2.1.1 Geometric Structures

Computational Method

The geometric molecular structures are optimized iteratively, with each iteration using an increased level of theory to refine the solution toward the optimum. The first optimization uses the Hartree Fock (HF) method and the 6-31G(d) basis set. The HF method is the simplest ab initio calculation that can be performed. However, it is not accurate enough for the computation of vibrational frequencies.

Next, the B3LYP [12, 105] functional is used with the same basis set. This functional accounts for some electron correlation through empirical correlation terms and has been widely used for optimization of geometric structures. While the functional might not be accurate enough for the prediction of the energy barrier between geometric structures, the results are usually considered reliable enough for the computation of the thermodynamic properties, such as heat capacity, entropy, and energy content. Finally, the 6-311++G(d,p) basis set [71], which includes diffuse and polarization functions, is used with B3LYP to ensure even more accurate predictions of the properties.

To ascertain the quality of the proposed method (B3LYP functional with 6-311++G(d,p) basis set), the benzene molecule is studied in greater detail. The geometric structure of this representative aromatic species is optimized using the Møller-Plesset perturbation formalism (MP2), which represents the logical next step in the refinement of the level of theory. This level of theory combined with the Dunning correlation consistent basis sets (cc-pVDZ, cc-pVTZ, and cc-pVQZ) offers predictions of higher fidelity for the C-H and C-C bond lengths in the benzene molecule.

All calculations were performed using the Gaussian 03 computer program [61].

theory	basis set	C − H	C − C
HF	6-31G(d)	1.0755	1.3863
B3LYP	6-31G(d)	1.0870	1.3968
	6-311++(d,p)	1.0844	1.3947
MP2	cc-pVDZ	1.0952	1.4057
	cc-pVTV	1.0814	1.3937
	cc-pVQZ	1.0808	1.3911
exptl		1.084	1.397

Table 2.1: Bond Length (in Å) for the Benzene Molecule Computed with Various Levels of Theory and Basis Sets.

Results

First, the C − C and C − H bond lengths of the benzene molecule are computed from the various levels of theory. The results are available in Table 2.1 and are compared with experimental data [72]. The HF method clearly underestimates the bond lengths. The MP2 methods converges to values slightly lower than the experimental values as the size of the basis set is increased from cc-pVZD to cc-pVTZ and then cc-pVQZ. On the other hand, the B3LYP functional with the 6-311++(d,p) basis set predicts both the C − H and the C − C bond lengths with good accuracy.

The list of species considered is given in Tables 2.2 and 2.3. Here, only the symmetry group of the molecules is included as geometric structure information. Full geometric structures are available in Appendix A. To simplify discussions of the species, the nomenclature introduced by Frenklach et al. [57] is used. Following this nomenclature, aromatic rings are represented by the letter A. The following subscript corresponds to the number of aromatic rings in the molecule. If the molecule is substituted, the groups are placed thereafter. For example, $A_1C_2H_3$ means one aromatic ring with a vinyl group attached to it.

Most of the PAH are planar under the present conditions and show at least C_s group symmetry at the three levels of theory considered. Because of an internal

Species		Symmetry
Name	Formula	Group
Benzene	A_1	D_{6h}
Phenyl radical	A_1-	C_{2v}
ethynylbenzene	A_1C_2H	C_{2v}
2-ethynylphenyl	A_1C_2H-2	C_s
3-ethynylphenyl	A_1C_2H-3	C_s
4-ethynylphenyl	A_1C_2H-4	C_{2v}
Styrene	$A_1C_2H_3$	C_s
1-phenylvinyl	$i-A_1C_2H_2$	C_{2v}
2-phenylvinyl	$n-A_1C_2H_2$	C_s
1-vinyl-2-phenyl	$A_1C_2H_3*$	C_s
1,2-diethynylbenzene	$A_1(C_2H)_2$	C_{2v}
napthalene	A_2	D_{2h}
1-napthyl	A_2-1	C_s
2-napthyl	A_2-2	C_s
2-ethynylnapthalene	A_2C_2HB	C_s
2-ethynyl-1-napthyl	A_2C_2HB*	C_s
1-ethynylnapthalene	A_2C_2HA	C_s
1-ethynyl-2-napthyl	A_2C_2HA*	C_s
vinylnapthalene	$A_2C_2H_3$	C_1
2-napthylvinyl	$A_2C_2H_2$	C_1
1,2-diethynylnaphthalene	$A_2(C_2H)_2$	C_s
acenaphthylene	A_2R5	C_{2v}
acenaphthyl	A_2R5-	C_s
1-ethynylacenapthylene	A_2R5C_2H	C_s
2-ethynyl-1-acenapthyl	A_2R5C_2H*	C_s
1,2-diethynylacenaphthylene	$A_2R5(C_2H)_2$	C_s
2-acenapthylvinyl	$A_2R5C_2H_2$	C_1
vinylacenapthylene	$A_2R5C_2H_3$	C_1
anthracene	A_3	D_{2h}
phenanphthrene	A_3	C_{2v}
phenanphthryl	A_3-	C_s
1-ethynylphenanphthrene	A_3C_2H	C_s
2-phenanphthrylvinyl	$A_3C_2H_2$	C_1
pyrene	$A_4(C_{16}H_{10})$	D_{2h}
tetracene	$A_4(C_{18}H_{12})$	D_{2h}
chrysene	$A_4(C_{18}H_{12})$	C_{2h}
pyrenyl radical	A_4-	C_s
acephenanphthrylene	A_3R5	C_s
acephenanphthryl	A_3R5-	C_s

Table 2.2: Details of the optimized molecules at B3LYP/6-311++G(d,p)

Species		Symmetry
1-ethynylacephenanphthrene	A_3R5C_2H	C_s
2-acephenanphthrylvinyl	$A_3R5C_2H_2$	C_1
cyclopenta[cd]pyrene	A_4R5	C_s
biphenyl	P_2	D_2
biphenyl radical	P_2-	C_1
perylene	A_5	D_{2h}
Coronene	A_7	D_{6h}

Table 2.3: Details of the optimized molecules at B3LYP/6-311++G(d,p)

degree of freedom, some PAH are not planar. The geometric structure of those molecules will be discussed later. Other PAH are not planar even in the absence of internal degrees of rotation. This is the case for the vinyl-substituted phenanthrene and acephenanthrylene ($A_3C_2H_2$ and $A_3R5C_2H_2$). These molecules require further attention. The lowest-energy optimal structures for these molecules are found to be nonplanar for all levels of theory considered, as shown in Figure 2.1. The optimal structure of vinyl phenanthrene obtained with B3LYP/6-311++G(d,p) exhibits a maximum dihedral angle of about 27°. In fact, both of these molecules have two optimal structures corresponding to a mirror image of one another. An optimal planar structure for those molecules exists, but a vibrational frequency analysis reveals one negative frequency, characteristic of saddle points. The planar structures separate the optimal structures with positive and negative dihedral angles. In the case of vinyl phenanthrene, the energy barrier between these two optimal structures was calculated and was found to be about 28.77 kJ/mol with HF/6-31G(d) and 30.84 kJ/mol with B3LYP/6-311++G(d,p). Using a Boltzmann distribution, one can estimate the equilibrium distribution of vinyl phenanthrene. Under normal flame conditions ($T = 1500\,\mathrm{K}$), the planar structure is barely populated at less than 10%.

In contrast to these structures, the two ethynyl-substituted phenanthrene and acephenanthrylene molecules (A_3C_2H and A_3R5C_2H) are planar for the three levels

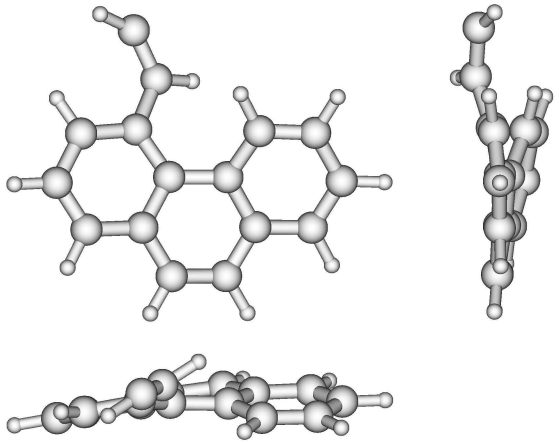

Figure 2.1: Geometric structure of vinyl phenanthrene ($A_3C_2H_2$) optimized with B3LYP//6-311++G(d,p).

of theory considered. Because of the strong nonplanarity of the vinyl-substituted molecules, a greater emphasis was put on the geometric structure of the two ethynyl-substituted molecules. In the attempt to find a nonplanar optimal configuration, several optimizations were performed with different starting points and with different convergence methods. For all simulations, the final optimal point always corresponded to a planar molecule, and it was not possible to recover a configuration similar to the vinyl-substituted molecules. Furthermore, a sensitivity analysis on the optimal structure did not reveal negative frequencies, hence confirming that this optimum was indeed a minimum.

2.1.2 Torsional Potential

Computational Method

Some molecules like the vinyl-substituted PAH exhibit an internal degree of freedom. This internal degree of freedom corresponds to an internal torsion where a section of the molecule can rotate with respect to the rest of the molecule. To better determine

the ground-state torsional angle between these two parts, a more thorough analysis of the torsional potential is required. The intent of the present work is to find reasonable estimates for the ground-state torsional angle as well as the energy barrier to rotation. Functionals like B3LYP are known to be unable to accurately reproduce the torsional potential of molecules like styrene [160, 158]. On the other hand, methods like CC (coupled cluster), while very expensive, have been found to predict quite accurately the torsional potential [160]. An alternative is the second-order Møller-Plesset perturbation formalism (MP2) as this method fills the gap between the inaccurate B3LYP and the very expensive CC methods, and has been used widely for computations of torsional potentials of substituted aromatic hydrocarbons [160, 158, 187].

Both B3LYP and MP2 calculations are performed using the Dunning correlation consistent basis sets. It was found that using the second-order perturbation theory (MP2) with the first Dunning basis set (cc-pVDZ) was a good compromise between accuracy and cost. To quantify the accuracy of this choice, the torsional potential of the styrene molecule is also computed using the next larger Dunning basis set: cc-pVTZ. However, it will be shown later that the small gain in accuracy does not justify the increase in calculation time. As a consequence, the torsional potentials of the other species are only computed at the MP2/cc-pVDZ level of theory.

The torsional potentials were obtained by increasing the torsional angle between the two rotating parts by increments of 15°. For each new configuration, the full geometry was reoptimized with the torsional angle kept frozen. Then, the energy was shifted with respect to the optimal configuration whose energy was set to zero.

Results

Figure 2.2 shows the predicted torsional potential of the styrene molecule ($A_1C_2H_3$) at three levels of theory: B3LYP/cc-pVDZ, MP2/cc-pVDZ, and MP2/cc-pVTZ. Also shown in the figure are the experimental measurements of the torsional potential by

Species formula	Twist angle		Energy barrier	
	B3LYP	MP2	B3LYP	MP2
$A_1C_2H_3$	0	18.8	18.5	13.0
$n - A_1C_2H_2$	0	90.8	21.8	10.8
$A_1C_2H_3*$	0	98.0	22.6	13.6
$A_2C_2H_3$	34.6	42.0	13.5	17.9
$A_2C_2H_2$	36.6	59.7	9.9	21.2
P_2	39.0	43.0	9.1	12.6
P_2-	24.1	90.0	13.0	22.3

Table 2.4: Ground state twist angle (in degrees) and energy barrier to rotation (in kJ/mol) from current B3/cc-pVDZ and MP2/cc-pVDZ calculations.

Caminati et al. [23]. As expected, the second-order perturbation theory predicts the energy barrier as well as the entire shape of the potential more accurately. While the second-order perturbation calculation with the cc-pVDZ basis set is slightly below the experimental measurements, the calculation with the larger cc-pVTZ basis set is slightly above. However, the deviations of those two results from the experimental data are the same, about 0.8 kJ/mol for the configuration where the vinyl group is perpendicular to the aromatic ring. As a consequence, the other torsional potentials are computed only with B3LYP/cc-pVDZ and MP2/cc-pVDZ.

The B3LYP method predicts the styrene molecule to be planar (C_s symmetry group), while the MP2 method both with cc-pVDZ and with cc-pVTZ predicts a nonplanar molecule (C_1 symmetry group). However, the energy difference between the planar and nonplanar configurations is very small, less than 0.2 kJ/mol at the MP2/cc-pVDZ level of theory. Because of this very shallow well, determining the equilibrium twist angle is difficult. Early experimental measurements [23] suggested a planar configuration, while results from recent electron diffraction studies [33] favor the nonplanar molecule with a twist angle of about 27°. The predictions of a nonplanar structure from the present MP2 calculations and other MP2 [125] and CC

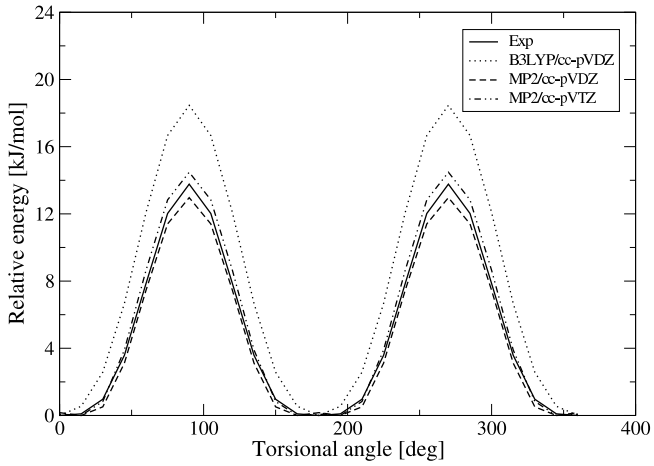

Figure 2.2: Predicted torsional potential of styrene with comparison to experimental measurements[23].

results [158] are consistent with the last experimental observation. However, the prediction of the equilibrium twist angle of the nonplanar molecule is strongly dependent on the level of theory considered for the computation. With second-order perturbation theory (MP2), Moriarty et al. [125] found an equilibrium twist angle of 27.6° with a small basis set (6-31G(d)), while the current simulations predict 18.8° with a medium-size basis set (cc-pVDZ) and 14.9° with a larger basis set (cc-pVTZ). With an even higher level of theory (CC/cc-pVDZ), Sancho-Garca and Prez-Jimnez [158] obtained an angle of about 10.0°. While the molecule always remains nonplanar, the twist angle monotonically decreases as the quality of the method or the size of the basis set increases. From those observations, one could stipulate that the styrene molecule is not planar and that its equilibrium twist angle should be close to 10°. Table 2.4 summarizes the resulting twist angle and energy barrier to rotation with the two methods (B3LYP and MP2 with cc-pVDZ) for different molecules.

Two radicals of the styrene molecule are of special interest: 1-vinyl-2-phenyl

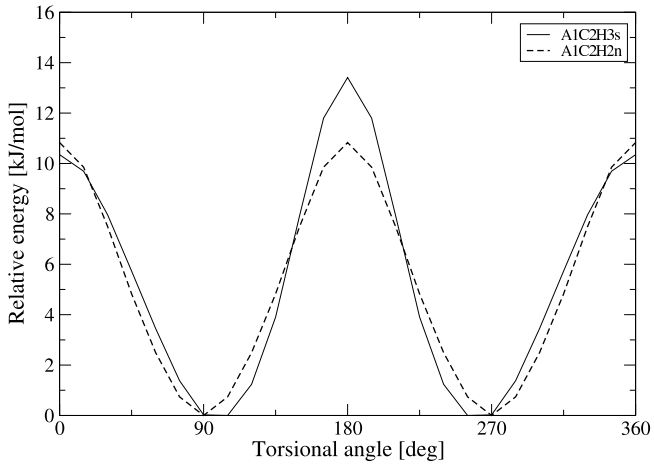

Figure 2.3: Predicted torsional potential of styrene radicals.

($A_1C_2H_3*$) with the radical site on the phenyl group and 2-phenylvinyl ($n-A_1C_2H_2$) with the radical site at the end of the vinyl group. As shown in Figure 2.3, both of these molecules exhibit an energy barrier to rotation similar to styrene. However, the molecules are not planar in their ground states, because of the interaction between the radical site and the rest of the molecule. For the two radicals, the MP2 calculations predict the rotating parts to be nearly orthogonal while the B3LYP method still predicts a planar molecule. For the 2-phenylvinyl, the twist angle is at 89.6° both with MP2/cc-pVDZ and with MP2/cc-pVTZ. The twist angle is slightly larger for 1-vinyl-2-phenyl with a value of 97.9° with MP2/cc-pVDZ and 104.1° with MP2/cc-pVTZ. In those computations, a zero twist angle corresponds to the vinyl group facing the radical site. Once again, it appears that the twist angle is a function of the size of the basis set. Moriarty et al. [125] optimized the geometric structures of 2-phenylvinyl and 1-vinyl-2-phenyl at several levels of theory and with different basis sets. Using small basis sets (from 3-21G to 6-31G(d,p)), they found smaller equilibrium twist angles for the two molecules than the present MP2 calculations: 38.1° for 2-phenylvinyl

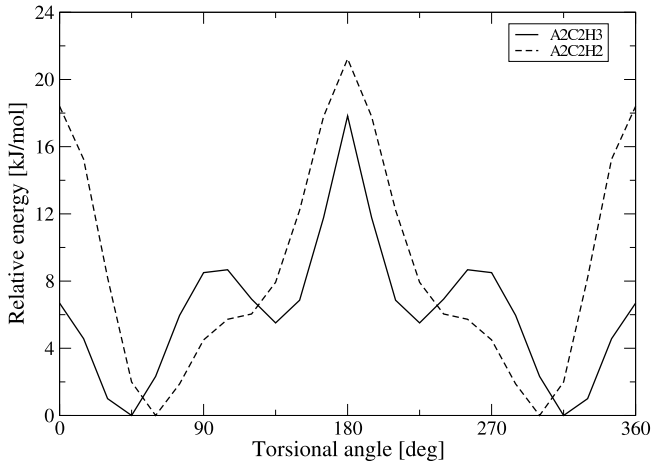

Figure 2.4: Predicted torsional potential of vinylnaphthalene.

and 5.8° for 1-vinyl-2-phenyl with their highest level of theory (MP2/6-31G(d,p)).

Figure 2.4 shows the torsional potential for the vinyl naphthalene molecule ($A_2C_2H_3$) and radical ($A_2C_2H_2$). The starting point, referred to as zero twist angle, corresponds to the configuration where the molecule is planar with the vinyl group pointing away from the second aromatic ring. Because of the strong repulsion of the vinyl group with the second aromatic ring, neither of the molecules are predicted to be planar, even at the B3LYP level of theory. Since the molecule and the radical are not symmetric with respect to the rotation, the torsional potential does not exhibit the same periodic multiwell shape that was observed from the styrene molecule and radicals. The potential rather goes through several local minima and maxima.

Finally, Figure 2.5 shows the torsional potential for the biphenyl molecule and radical. The figure also shows the experimental potential measured by Bastiansen et al. [10]. Experimental results [4] indicate a twist angle of about 44.4°, in very good agreement with the present MP2 computation (43.0°). The energy barrier to rotation was found from experiments to be around 6.0 ± 0.5 kJ/mol for the planar

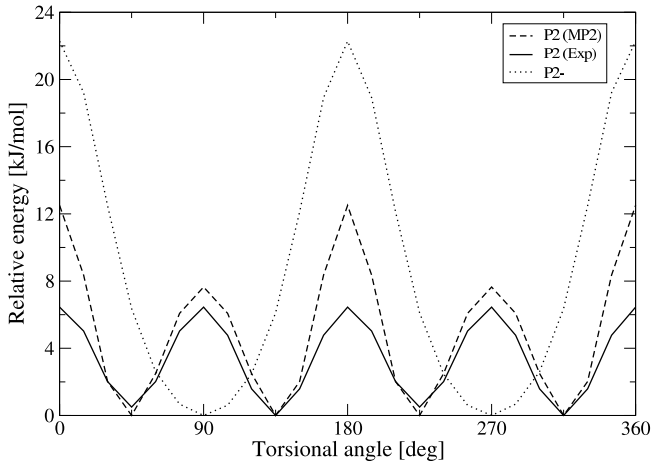

Figure 2.5: Predicted torsional potential of biphenyl and biphenyl radical.

and ortho configurations [10, 4, 24]. The MP2 calculations predict an energy barrier of 12.5 kJ/mol for the ortho and 7.7 kJ/mol for the planar configurations. Tsuzuki et al. [187] performed similar MP2 calculations with larger basis sets as well as other methods like MP4 (fourth-order Møller-Plesset perturbation) and CCSD(T) (coupled cluster both single and double substitutions with perturbative estimation of the contributions of triple excitations). With these quite costly levels of theory, they were able to reproduce the energy barrier at 90°, but not the one at 0°. A more thorough analysis of this torsional potential with more accurate methods and larger basis sets should be considered to resolve these discrepancies.

2.1.3 Thermodynamic Properties

As mentioned earlier, the geometric structures and vibrational frequencies for all stationary points considered here were calculated using the B3LYP functional [12, 105]

Species name	Species formula	Number of frequencies
Ethylene	C_2H_4	12
Propargyl radical	C_3H_3	3
Propyne	C_3H_4	10
Allene	C_3H_4	11
Cyclopropene	C_3H_4	15
Phenyl radical	C_6H_5	26
Benzene	C_6H_6	20
Fulvene	C_6H_6	26
Styrene	C_6H_8	38

Table 2.5: List of species selected to compute the scaling factor applied to the theoretical vibrational frequencies.

and the 6-311++G(d,p) basis set [71]. To improve the accuracy of the thermodynamic properties, such as specific heat capacity and entropy, the vibrational frequencies were rescaled using a common scaling factor. This scaling factor was evaluated from a least-squares approach by comparing experimental and computed frequencies as described by Scott and Radom [162]. A set of relevant molecules has been selected (Table 2.5), whose experimental vibrational frequencies were taken from the Computational Chemistry Comparison and Benchmark Database (NIST) [26]. The set of molecules has been selected from the C_2, C_3, and C_6 species to represent the most important structural groups for the investigated PAH for which experimental data are available. The fitted scaling factor for the computed vibrational frequencies with respect to their experimental frequencies is 0.96626, with a relative uncertainty of ± 0.0102. The heat capacity $C_p^\circ(T)$, entropy $S^\circ(T)$, and thermal energy content $H^\circ(T) - H^\circ(0)$ were computed using the rescaled vibrational frequencies and the moments of inertia. Table 2.6 summarizes the thermodynamic properties for all species.

Some of the molecules have one internal degree of rotation. This internal rotation is treated as a hindered rotor rather than as a free rotor for better prediction

Species formula	C_p°	S°	ΔH°
A_1	83.5	269.9	14.4
A_1-	82.0	289.8	14.4
A_1C_2H	117.6	329.8	19.9
A_1C_2H-2	116.0	341.4	19.9
A_1C_2H-3	116.0	340.7	19.8
A_1C_2H-4	115.9	334.7	19.8
$A_1C_2H_3$	120.8	345.7	20.4
$i-A_1C_2H_2$	124.7	350.0	21.5
$n-A_1C_2H_2$	123.0	350.1	21.0
$A_1C_2H_3*$	121.1	357.1	20.9
$A_1(C_2H)_2$	152.0	374.7	25.6
A_2	134.4	335.3	21.1
A_2-1	132.8	352.3	21.0
A_2-2	133.0	352.1	21.0
A_2C_2HB	168.7	392.0	26.8
A_2C_2HB*	166.9	398.4	26.9
A_2C_2HA	168.5	391.0	26.8
A_2C_2HA*	166.8	396.9	26.8
$A_2C_2H_3$	176.5	405.9	28.2
$A_2C_2H_2$	174.9	410.4	28.0
$A_2(C_2H)_2$	202.9	435.3	32.7
A_2R5	154.7	359.9	23.5
A_2R5-	152.5	370.7	23.4

Species formula	C_p°	S°	ΔH°
A_2R5C_2H	188.6	410.1	29.3
A_2R5C_2H*	186.9	416.4	29.3
$A_2R5(C_2H)_2$	223.3	454.6	35.3
$A_2R5C_2H_2$	195.2	429.1	30.6
$A_2R5C_2H_3$	196.7	424.5	30.8
A_3	185.9	391.7	28.3
A_3	185.5	398.5	28.3
A_3-	183.6	408.6	28.2
A_3C_2H	219.7	454.1	34.2
$A_3C_2H_2$	222.4	455.9	34.4
$A_4(C_{16}H_{10})$	203.8	402.9	30.1
$A_4(C_{18}H_{12})$	237.7	448.2	35.6
$A_4(C_{18}H_{12})$	236.9	456.5	35.7
A_4-	201.9	419.8	30.0
A_3R5	205.7	422.0	30.8
A_3R5-	203.9	427.2	30.7
A_3R5C_2H	239.8	467.0	36.6
$A_3R5C_2H_2$	240.5	472.3	36.7
A_4R5	224.0	433.0	32.7
P_2	167.6	397.5	26.9
P_2-	165.0	406.8	26.8
A_5	255.6	469.2	38.0
A_7	287.9	472.0	41.2

Table 2.6: Thermodynamic properties of PAH molecules at 298K. Heat capacities and entropies are in J/mol/K, enthalpies are in kJ/mol.

of the thermodynamic properties. Correcting the thermodynamic properties for hindered rotors requires the computation of the torsional potential of the molecule. The torsional potentials for some of these molecules were presented in the previous section. Due to the inherent cost of the computations, the torsional potentials were only evaluated for a set of molecules whose rotating tops are representative of those typically found in PAH. Then, it is assumed that two molecules with identical rotating tops have identical torsional potentials. For instance, the torsional potentials of the molecules $A_2C_2H_2$ and $A_2R5C_2H_2$ are assumed to be identical, because the rotating tops are the same. However, the rotating top found in those two molecules ($A_2C_2H_2$ and $A_2R5C_2H_2$) is different from the one found in $n-A_1C_2H_2$ because of the presence of the second aromatic group. This restriction is justified by the localized interaction between the vinyl group and the closest atoms of the remaining part of the molecule.

To simplify the treatment of the internal rotation as hindered rotors, Pitzer et al. [150] originally assumed that the torsional potential follows the relation

$$V(\phi) = \frac{1}{2} V_0 \left(1 - \cos(n\phi)\right) \tag{2.1}$$

with V_0 the barrier to rotation, n the number of wells of the potential, and $\phi = 0$ the location of the minimum. However, it can be observed in Figures 2.2-2.5 that the torsional potentials of several of the PAH do not follow this relation. In fact, this restriction is equivalent to considering only the most energetic mode in the Fourier series expansion of the torsional potential function. In a more accurate approach by Lay et al. [94], the potential function is decomposed into its Fourier modes

$$V(\phi) = a_o + \sum_k a_k \cos(k\phi) + \sum_k b_k \sin(k\phi) \tag{2.2}$$

Then, an approximate Hamiltonian matrix is formed by evaluating the Hamiltonian

Species	Degeneracy		C_p°			S°		
formula	σ	p	No Corr.	Free Rot.	Hind. Rot.	No Corr.	Free Rot.	Hind. Rot.
$A_1C_2H_3$	1	2	121.9	117.7	120.8	355.4	350.1	345.7
$n - A_1C_2H_2$	1	2	121.9	117.8	123.0	348.7	354.9	350.1
$A_1C_2H_3*$	1	1	120.1	116.0	121.1	349.2	362.3	357.1
$A_2C_2H_3$	1	1	172.7	168.6	176.5	397.7	411.8	405.9
$A_2C_2H_2$	1	1	172.3	168.2	174.9	404.2	417.6	410.4
P_2	2	2	167.0	162.9	167.5	385.1	402.0	397.5
P_2-	1	2	165.5	161.4	165.0	404.7	413.3	406.8

Table 2.7: Comparison of heat capacity and entropy with and without correction for internal rotations. Corrections include free rotor and hindered rotor. The symmetry number of the rotating top (σ) and the periodicity of the potential are also given. Heat capacities and entropies are in J/mol/K.

operator on a given set of wave functions of free rotation (100 wave functions were used). The energy levels of a molecule are obtained by diagonalization of the Hamiltonian matrix. Then, the thermodynamic properties are evaluated from these energy levels. A Fortran program, ROTATOR [94], is used for the discretization of the Hamiltonian operator and calculation of the energy levels. Finally, the degeneracy of the energy levels is included in the partition function by considering the ratio of the periodicity of the potential to the symmetry number of the rotating top.

Table 2.7 lists the heat capacity and entropy for some of the molecules with internal degree of rotation. Three sets of thermodynamic properties have been computed. In the first set, the internal rotation was treated as a simple vibration, thus equivalent to not applying any corrections. In the second set, the internal rotation was treated as a free rotors, while a correction for hindered rotor was used in the last set. Pitzer [149] measured the entropy for the styrene molecule at 298 K and obtained $S^\circ = 345.1 \pm 2.1$ kJ/mol. The entropy predicted without correction ($S^\circ = 355.4$ kJ/mol) is clearly overestimated, as is the entropy with correction for free rotor ($S^\circ = 350.1$ kJ/mol). On the other hand, correcting for hindered rotor leads to

a value of $S^\circ = 345.7\,\mathrm{kJ/mol}$, which is within the margin of error of the experimental value. More recently, Chirico [30] measured the entropy of biphenyl and obtained $S^\circ = 389.7 \pm 0.3\,\mathrm{kJ/mol}$, which is very close to the value of $S^\circ = 391.7\,\mathrm{kJ/mol}$ computed with correction for hindered rotor. Those results emphasize the importance of treating internal degrees of rotation in PAH as hindered rotors, and not only as free rotor.

2.1.4 Enthalpies of Formation

G3MP2//B3 method

The G3(MP2)//B3LYP method has been used to calculate the enthalpies of formation of all considered species. This method is based on ab initio calculations, and empirically based corrections. Full details, the theoretical basis, and a validation of the method can be found in Baboul et al. [6]. Here, only a brief description is provided.

In the first step of the method, the geometries are optimized at the B3LYP/6-31G(d) level. The zero-point energies (ZPE) are obtained from this level and scaled by a factor of 0.96. In the second step, a single-point quadratic configuration interaction with triples is performed using the frozen core approximation, QCISD(T,FC)/6-31G(d). In the third step, a second-order Møller-Plesset perturbation theory computation is done on the original basis set MP2/6-31G(d) and on a larger basis set denoted MP2/G3MP2Large. This last basis set corresponds to 6-311+G(2df,2p) for second-row elements. Finally, the method of Baboul et al. [6] applies a so-called higher-level correction (HLC) to account for remaining deficiencies in the energy calculations. This correction is a linear function of the number of valence electrons (n_α, n_β)

$$E(\mathrm{HLC}) = -\mathrm{An}_\alpha - \mathrm{B}(\mathrm{n}_\alpha - \mathrm{n}_\beta) \tag{2.3}$$

with $n_\alpha > n_\beta$. The values for A and B provided for molecules are $10.041\,\mathrm{mE_h}$ and $4.995\,\mathrm{mE_h}$, respectively. From this, the corrected energy can be expressed as

$$\begin{aligned} E_0\,[\mathrm{G3(MP2)//B3}] =& E(ZPE) + E\,[\mathrm{QCISD(T)/6-31G(d)}] \\ &+ E\,[\mathrm{MP2/G3MP2Large}] - E\,[\mathrm{MP2/6-31G(d)}] \\ &+ E(\mathrm{HLC}) \end{aligned} \tag{2.4}$$

The standard heat of formation is then computed from the decomposition of the different species to hydrogen and carbon atoms in their standard state of reference. The heat of formation and energy content for the hydrogen and carbon atoms were taken from the NIST-JANAF tables [29].

Group Correction

Some differences exist between the enthalpies of formation of the different species calculated previously and their experimental values. In order to improve the prediction of these enthalpies, the group correction method, originally developed by Wang and Frenklach [196], is applied to the G3MP2//B3 computed values. The method is based on the idea that the deviations between computed and experimental enthalpies are systematic and that the errors in the enthalpies of formation of all molecules can be reconstructed from errors attributed to the different structural groups that define the molecules. From this assumption, the values for corrections associated with the structural groups appearing in the considered molecules can be determined. The subsequent evaluation of the corrected enthalpies is straightforward. As a first step, the individual structural groups used in the analysis are defined. Depending on the availability and reliability of experimental data for the molecules containing these groups, different methods will be used for the determination of the group correction values. Each of these will be detailed in the following, and an example for the validity

a) First set of structural groups

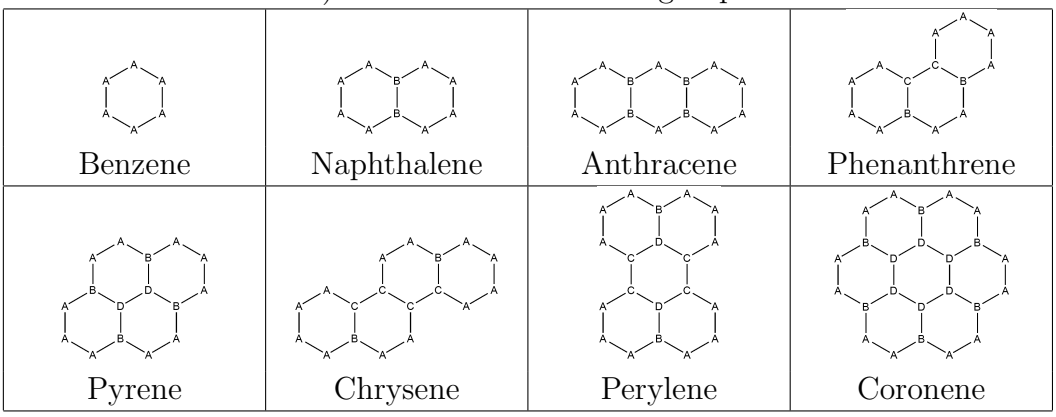

b) Second set of structural groups

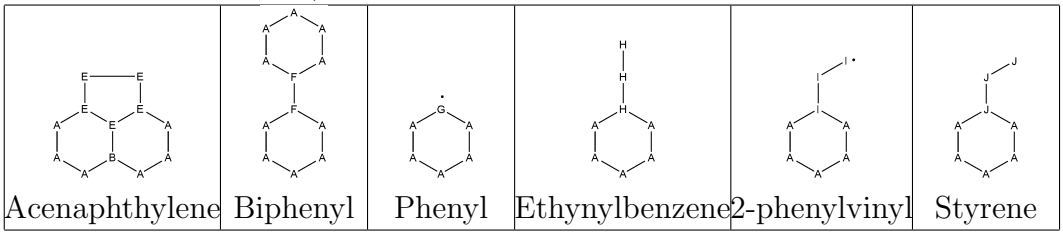

Figure 2.6: Geometric structures and group identification for the selected aromatic species used for determination of group corrections ($A = C_B - H$, $B = C_F - (C_B)_2(C_F)$, $C = C_F - (C_B)(C_F)_2$, $D = C_F - (C_F)_3$).

of the structural group correction approach will be provided.

The structural groups used to define the considered molecules follow the definition of Benson [13] and can be categorized into two sets. The first set consists of four structural groups, which are found in purely aromatic species. This set is given by $A = C_B - H$, $B = C_F - (C_B)_2(C_F)$, $C = C_F - (C_B)(C_F)_2$, and $D = C_F - (C_F)_3$. Figure 2.6 shows the definition of the molecules that will be used below to determine the correction values for these groups. This figure also explains the structure of these four groups more clearly. The second set has six more groups found in substituted aromatics and radicals. This set is given by $E = R5$, and $F = C_P - C_P$, $G = C*$, $H = C - C_2H$, $I = C - C_2H_2$, and $J = C - C_2H_3$. Group E denotes a five-membered ring, such as in acenaphthalene, and group F connects the aromatic rings in biphenyl.

Groups G, H, I, and J are substituted aromatics.

The group correction values of the first set are determined first. This also provides an example for the validity of the approach. The corrections for the second set are discussed thereafter.

The details of the group correction method can be found in Wang and Frenklach [196]. The correction values for the groups are determined by comparing the computed enthalpies of formation for experimentally well characterized species with measured data and optimizing the required corrections for the structural groups by using a least-squares approach. For groups found in purely aromatic species, Wang and Frenklach [196] considered two sets of species in their least-squares method: a short list of five species and a larger list of eleven species. Their results showed that species used in the least-squares minimization have to be chosen carefully, because the energies of some molecules might suffer from large experimental uncertainties. Furthermore, the groups found in different species might not be identical. For these reasons, experimental values for different species cannot always be reproduced simultaneously with good accuracy. Here, an intermediate list of eight species is considered. These eight species are all relevant to soot formation as they are included usually in chemical mechanisms for soot precursors. This set consists of benzene, naphthalene, anthracene, phenanthrene, pyrene, chrysene, perylene, and coronene. Since all these molecules are constructed only from the four groups in the first set described above, only four parameters can be adjusted, and the system is overdetermined. A weighted least-squares minimization with the objective function

$$J(\mathrm{GC_i}) = \sum_{\mathrm{k=1}}^{8} \left(\frac{\Delta_\mathrm{f}\mathrm{H}^\circ_\mathrm{exp} - \Delta_\mathrm{f}\mathrm{H}^\circ_\mathrm{cal} - \sum_{\mathrm{i=1}}^{\mathrm{n_k}} \mathrm{GC_i}}{\sigma_\mathrm{k}} \right)^2 \tag{2.5}$$

was used to determine the correction values $\mathrm{GC_i}$ of the structural group i. The weights σ_k represent the experimental error in the enthalpy of formation of species k at 298 K,

$\Delta_f H^\circ_{\text{exp}}$ are the experimental enthalpies of formation, and $\Delta_f H^\circ_{\text{cal}}$ are the calculated G3(MP2)//B3 enthalpies.

The validity of the structural group correction approach and the accuracy of the values obtained for the first set of groups can be assessed for a simple example that involves only a few species. For this, a set of linear aromatic species of increasing size is considered. These species are benzene (one ring), naphthalene (two rings), anthracene (three rings), and tetracene (four rings). Benzene consists of six $C_B - H$ groups. The three remaining species can be constructed from this by the successive addition of two $C_B - H$ and two $C_F - (C_B)_2(C_F)$ groups for each ring. This implies that the correction for these species can be written as

$$6\text{GC}_\text{A} + 2(r-1)(\text{GC}_\text{A} + \text{GC}_\text{B}) \tag{2.6}$$

where GC_A and GC_B are the correction values for the respective groups, and r is the number of aromatic rings. The correction is hence linear in the number of rings. Figure 2.7 shows the corrections to the computed values that are required to predict the lower and upper bounds of the experimental error margin. The solid line shows the corrections determined from the structural group correction values from the least-squares fitting procedure. It is observed that the linear trend for the corrections is found in the experimental data and that the structural group model provides the required corrections with reasonable accuracy.

While it is possible to find experimental measurements of the enthalpies of formation of different aromatic species with identical structural groups, experimental data are scarce for the substituted aromatics and radicals necessary to determine the correction values for the structures in the second set. Here, one experimental data point for each of the structural groups was chosen. Experimental data are available for acenaphthylene, biphenyl, phenyl, ethynylbenzene, and styrene. These have been

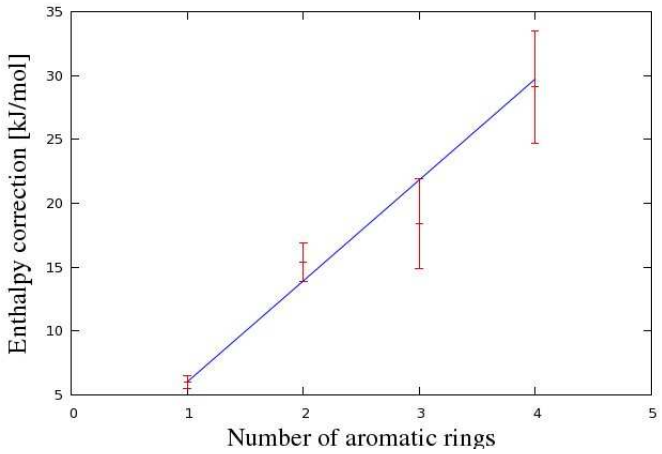

Figure 2.7: Required corrections to the computed enthalpies of formation for linear aromatic species: benzene (one ring), naphthalene (two rings), anthracene (three rings), and tetracene (four rings). Error bars correspond to the experimental uncertainties and the solid line to the group corrections from the present method.

used in combination with the correction values of the first set of groups to determine the corrections for $R5$, $C_P - C_P$, $C*$, $C - C_2H$, and $C - C_2H_3$, respectively. For the remaining group, $C - C_2H_2$, no experimental enthalpies are available. The phenylvinyl radical was used to determine the correction for $C - C_2H_2$ and determine the target enthalpy for this species from the experimental value for styrene and the bond dissociation energy (BDE) obtained from the difference in experimental energies of ethylene and vinyl.

Results

The enthalpies of formation of the eight targets used for aromatic species are presented in Table 2.8, while the group corrections are presented in Table 2.9. Most of the enthalpies of formation of the polycyclic aromatic hydrocarbons are taken from Slayden and Liebman [177]. Benzene and naphthalene have well-established enthalpies of formation, which are given as $82.93 \pm 0.5\,\mathrm{kJ/mol}$ [152] and $150.3 \pm 1.5\,\mathrm{kJ/mol}$ [181], respectively.

Group	Correction
$C_B - H$	1.007
$C_F - (C_B)_2(C_F)$	2.939
$C_F - (C_B)(C_F)_2$	0.314
$C_F - (C_F)_3$	1.787
$C*$	−6.476
$C - C_2H$	−6.406
$C - C_2H_2$	−14.336
$C - C_2H_3$	2.564
$R5$	6.538
$C_P - C_P$	8.699

Table 2.8: G3MP2//B3 group correction (in kJ/mol).

		G3MP2//B3	
Species	Exp.	Orig.	GC
Aromatic species			
benzene	82.93 ± 0.5	76.95	82.99
naphthalene	150.3 ± 1.5	134.89	148.83
anthracene	226.7 ± 3.5	208.28	230.11
phenanthrene	201.7 ± 2.9	185.18	201.76
pyrene	225.7 ± 1.2	200.69	226.09
chrysene	263.5 ± 4.5	240.64	259.86
perylene	306.0 ± 0.8	283.32	306.11
coronene	302.0 ± 8.0	251.99	292.43
avg. error		22.11	2.34
Substituted aromatics and radicals			
phenyl	339.7 ± 2.0	341.14	
phenylacetylene	306.6 ± 1.7	307.97	
styrene	146.9 ± 1.0	138.38	
styryl	393.5 ± 7.0	402.80	
acenaphthylene	259.7 ± 4.6	244.18	
biphenyl	182.0 ± 0.7	163.33	

Table 2.9: Standard heat of formation (in kJ/mol) of the target species obtained from experiments (Exp.) and originally calculated with G3(MP2)//B3 (Orig.) used for the calculation of the group corrections (GC in kJ/mol).

New high-precision measurements of the enthalpy of formation of anthracene have been performed recently by Nagano [130]. The enthalpy of combustion was measured to be $\Delta_c H^\circ = -7065.0 \pm 1.1\,\mathrm{kJ/mol}$. This value leads to an enthalpy of formation for the solid phase of $\Delta_f H_s^\circ = 126.7 \pm 2.1\,\mathrm{kJ/mol}$. This value is in good agreement with the previously used value of $127.4 \pm 5.9\,\mathrm{kJ/mol}$ [116]. Using the sublimation enthalpy from Oja and Suuberg [138], the enthalpy of formation for the gas phase is evaluated as $\Delta_f H_g^\circ = 226.7 \pm 3.5\,\mathrm{kJ/mol}$. Similar measurements were performed for phenanthrene [131]. The enthalpy of combustion was established at $\Delta_c H = -7048.7 \pm 0.9\,\mathrm{kJ/mol}$, leading to an enthalpy of formation for the gas phase of $\Delta_f H^\circ = 201.7 \pm 2.9\,\mathrm{kJ/mol}$. This value agrees well with previous measurements [179]. Finally, the enthalpies of formation of chrysene, perylene, and coronene are used as reported by Slayden and Liebman [177].

The G3MP2//B3 method with group correction shows an average deviation between experimental and calculated enthalpies of formation of about $2.34\,\mathrm{kJ/mol}$. This value shows great improvement compared to the results obtained by Wang and Frenklach [196] of 5.9 and $6.3\,\mathrm{kJ/mol}$ for the two sets of target species. To the knowledge of the authors, PAH of the size of coronene have not been computed with such expensive level of theory as G3MP2//B3. Although the configuration of coronene is substantially different from the other target species, the group corrections can also be applied to this molecule with an error within the experimental uncertainty, which demonstrates the efficiency of the method. The standard enthalpies of formation of the other species are reported in Table 2.10.

During the compilation of the sets of target species, three additional molecules were investigated, namely, tetracene ($C_{18}H_{12}$), triphenylene ($C_{18}H_{12}$), and pyracylene ($C_{14}H_8$). However, these molecules were not included in the least-squares approach,

Formula	$0K$	$298K$	$298K + GC$
$A_1C_2H - 2$	592.65	582.95	574.10
$A_1C_2H - 3$	588.39	578.64	569.79
$A_1C_2H - 4$	588.08	578.29	569.44
$i - A_1C_2H_2$	380.58	364.07	354.77
$n - A_1C_2H_2$	419.89	402.80	393.50
$A_1C_2H_3*$	427.99	410.85	410.97
$A_1(C_2H)_2$	553.17	542.84	534.06
$A_2 - 1$	441.98	422.86	429.31
$A_2 - 2$	440.70	421.58	428.03
A_2C_2HB	385.33	365.70	372.22
A_2C_2HB*	678.57	663.19	662.23
A_2C_2HA	383.90	364.20	370.72
A_2C_2HA*	675.71	660.25	659.29
$A_2C_2H_3$	230.09	203.35	218.84
$A_2C_2H_2$	512.51	489.83	488.48
$A_2(C_2H)_2$	613.80	597.87	596.98
A_2R5-	544.17	525.30	533.34
A_2R5C_2H	491.65	472.38	480.49
A_2R5C_2H*	776.91	761.89	762.51
$A_2R5(C_2H)_2$	721.72	706.31	707.00
$A_2R5C_2H_2$	614.17	591.94	592.12
$A_2R5C_2H_3$	335.63	309.33	326.41
A_3-	507.05	482.40	491.49
A_3C_2H	457.98	433.00	442.16
$A_3C_2H_2$	600.64	571.70	572.93
A_4-	547.79	522.87	540.79
A_3R5	314.97	286.62	304.78
A_3R5-	603.82	579.64	590.32
A_3R5C_2H	553.71	529.08	539.83
A_4R5	342.53	313.93	334.38
P_2-	469.22	445.25	456.54

Table 2.10: Standard enthalpies of formation calculated with the G3(MP2)//B3 method with and without group corrections (in kJ/mol).

because of the uncertainty or scarcity of the experimental measurements. Measurements were performed for tetracene using the same methodology as for phenanthrene [131]. The enthalpy of combustion was established at $\Delta_c H^\circ = -9005.1 \pm 1.8\,\mathrm{kJ/mol}$, thus leading to an enthalpy of formation for the gas phase of $\Delta_f H^\circ_h = 331.6 \pm 4.4\,\mathrm{kJ/mol}$. While the value for phenanthrene agrees well with other measurements [179], the value for tetracene is too endothermic. In earlier work, Slayden and Liebman [177] recommended a lower value for the enthalpy of formation for the gas phase of 302 kJ/mol. The present method using G3MP2//B3 predicts an enthalpy of formation of 287.68 kJ/mol without corrections and 317.40 kJ/mol with group corrections. This last value is very close to the arithmetic mean between the larger value of Nagano [131] and the recommended value of Slayden and Liebman [177], 316.8 kJ/mol. This last value was used in Figure 2.7.

The computed enthalpies of formation of triphenylene are $\Delta_f H^\circ = 239.99\,\mathrm{kJ/mol}$ without correction and $\Delta_f H^\circ = 253.96\,\mathrm{kJ/mol}$ with correction. Slayden and Lienman [177] reported an enthalpy of formation of $\Delta_f H^\circ = 265.5 \pm 2.5\,\mathrm{kJ/mol}$. Wang and Frenklach [196] already noticed that obtaining a good agreement between experimental and computed values for this molecule was difficult. They also noticed that the introduction of triphenylene in the least-squares approach would greatly lower the quality of the corrections.

The computed enthalpies of formation of pyracylene are $\Delta_f H^\circ = 409.0\,\mathrm{kJ/mol}$ without correction and $\Delta_f H^\circ = 426.1\,\mathrm{kJ/mol}$ with correction. An experimental measurement of the enthalpy of formation has been reported recently by Diogo et al. [48] with a value of $\Delta_f H^\circ = 409.0 \pm 6.2\,\mathrm{kJ/mol}$. In this specific case, the method seems to perform better without the group corrections. However, as for triphenylene, the lack of repeated measurements with high accuracy justifies the removal of these two species from the least-squares optimization. Furthermore, these species typically do not appear in chemical mechanisms used to simulate soot formation.

2.1.5 Summary

In this section, the geometric structures of all important PAH species have been optimized. From these optimized structures, thermodynamic properties like heat capacity, entropy, and heat of formation have been computed. These thermodynamic properties are crucial for the following devlopment of the chemical mechanism.

2.2 Chemical Mechanism

With detailed thermodynamic properties for all species, it is now possible to develop a chemical mechanism for the combustion of small and large hydrocarbon fuels. The intent of this work is to create a mechanism that can accurately represent the formation of soot precursors from the combustion of fuel components usually found in surrogates. Towards this goal, the mechanism is first constructed for small hydrocarbons like methane (CH_4) and other C_2 fuels. Then, kinetic reactions for larger fuels are added to this mechanism. The next sections present the portion of the mechanism relevant to the combustion of these different fuels.

2.2.1 Small Hydrocarbon Chemistry

One of the best mechanisms for methane combustion to date is the GRI-MECH v3.0 [178]. This mechanism already includes C_2 species like acetylene, ethylene, and ethane and has been shown to give very good results for combustion of natural gas. However, the burning velocities for species like acetylene and ethylene were not correctly represented. In recent studies, Eiteneer and Frenklach [52] have extended and optimized a larger mechanism based on the GRI-MECH v3.0 for the combustion of acetylene. This mechanism, composed of 52 species and 744 reactions, forward and backward reactions being counted separately, is the starting point for the current work.

In the original development of the GRI-MECH v3.0 and the further work of Eiteneer and Frenklach [52], the mechanisms were optimized in order to improve the comparison with experiments. The Arrhenius prefactors of some reactions were adjusted within the experimental uncertainties to better match a series of targets. In the present work, several new reactions have been added and previously present reactions have been updated with newer experimental or computational evaluation of the rate

constants. As a consequence, the rate constants of some of the reactions previously optimized had to be re-evaluated.

Among these reactions, the reaction of hydrogen recombination with methyl radical is very important for its high sensitivity for laminar flame speeds. To improve the overall aggreement with experimental measurements, the rate constant for this reaction has been revised. Recently, the high pressure limit rate constant has been evaluated from high-fidelity quantum calculations by Harding et *al.* [67]. The calculated rate constant has a slight temperature dependence and compares very well with experimental data. The low pressure rate constant was optimized in the successive versions of the GRI-MECH. A new fit to experimental measurements for the low pressure rate constant has been derived and is used.

To improve the ignition delay times of acetylene, Laskin and Wang [102] considered a new pathway for the activation of acetylene. From quantum calculations, they showed that acetylene can isomerize into triplet vinylidene $H_2CC:$ before reacting with molecular oxygen.

$$C_2H_2 + M \leftrightarrows H_2CC: + M \tag{2.7}$$

$$H_2CC: + O_2 \leftrightarrows 3 - CH_2 + CO_2 \tag{2.8}$$

$$\leftrightarrows 2\,HCO \tag{2.9}$$

Another pathway is the direct addition of O_2 onto acetylene as studied by Sheng and Bozzelli [173].

$$C_2H_2 + O_2 \leftrightarrows 2\,HCO \tag{2.10}$$

Similar analysis have been performed for ethylene [194] at high temperatures. Wang considered the $1,2-H$ shift and the $1,1-H_2$ elimination to form triplet vinylidene

as possible pathways for ethylene activation before reaction with molecular oxygen.

$$C_2H_4 + O_2 \rightarrow CH_3 + CO_2 + H \tag{2.11}$$

$$C_2H_4 + M \leftrightarrows H_2CC\colon + H_2 + M \tag{2.12}$$

All these reaction pathways have been included in the mechanism.

Hydrogen addition reactions to acetylene and ethylene to form vinyl and ethyl radicals have been recently recomputed with high fidelity quantum calculations by Miller and Klippenstein [118]

$$C_2H_2 + H\,(+M) \leftrightarrows C_2H_3\,(+M) \tag{2.13}$$

$$C_2H_4 + H\,(+M) \leftrightarrows C_2H_5\,(+M) \tag{2.14}$$

and were directly included in the mechanism. Similar quantum calculations have been performed for the reaction of hydroxyl radical with acetylene and ethylene [167, 169]. While the reaction with acetylene was found to yield the same products as in the original GRI-MECH,

$$C_2H_2 + OH \leftrightarrows C_2H + H_2O \tag{2.15}$$

$$\leftrightarrows HCCOH + H \tag{2.16}$$

$$\leftrightarrows CH_2CO + H \tag{2.17}$$

$$\leftrightarrows CH_3 + CO \tag{2.18}$$

the reaction with ethylene leads to the formation of C_2H_5O with a significant branching ratio at moderate temperatures.

$$C_2H_4 + OH \leftrightarrows C_2H_3 + H_2O \tag{2.19}$$

$$\leftrightarrows C_2H_5O \tag{2.20}$$

This species can also be formed by O-abstraction from HO_2 by ethyl radical [107]

$$C_2H_5 + HO_2 \leftrightarrows C_2H_5O + OH \tag{2.21}$$

or by direct addition of oxygen atoms onto ethyl radicals.

$$C_2H_5 + O \leftrightarrows C_2H_5O \tag{2.22}$$

The high pressure limit of the rate constant for this reaction has been calculated by Harding et *al.* [68]. In the same work, the high pressure rate constant for the oxygen atom addition to methyl and vinyl radicals were also computed. These values were used in the mechanism. The ethoxy radical can decompose following two pathways [37]

$$C_2H_5O \leftrightarrows CH_3CHO + H \tag{2.23}$$

$$\leftrightarrows CH_3 + CH_2O \tag{2.24}$$

The reaction of oxygen atoms with ethylene has been recently analyzed by Nguyen

et *al.* [134]. Three main product channels were considered.

$$C_2H_4 + O \leftrightarrows CH_2CHO + H \tag{2.25}$$

$$\leftrightarrows 3-CH_2 + CH_2O \tag{2.26}$$

$$\leftrightarrows CH_3 + HCO \tag{2.27}$$

The individual rate constants have been fitted between 300 K and 2000 K based on the total rate constants and the individual branching ratios. The decomposition of the vinyloxy radical (CH_2CHO) plays a major role in the combustion of C_2 species. Recently, Senosiain et *al.* [168] calculated the rate constants for the following pathways

$$CH_2CHO \leftrightarrows CH_3 + CO \tag{2.28}$$

$$\leftrightarrows CH_2CO + H \tag{2.29}$$

Several H-abstraction reactions have also been reconsidered in the light of more recent work. For instance, the rates of the reactions of ethyl radicals with molecular oxygen and methyl radicals were taken from recent quantum simulations [119, 209]

$$C_2H_5 + CH_3 \leftrightarrows C_2H_4 + CH_4 \tag{2.30}$$

$$C_2H_5 + O_2 \leftrightarrows C_2H_4 + HO_2 \tag{2.31}$$

Miller et *al.* [119] showed that the reaction of ethyl radicals with molecular oxygen can simply be modeled by the H-abstraction path at high temperatures. The direct addition of O_2 onto the radical occurs only at low temperatures. Most of the H-abstraction reactions from ethane have been updated with more recent values [91, 99,

25, 11]

$$C_2H_6 + H \leftrightarrows C_2H_5 + H_2 \tag{2.32}$$

$$C_2H_6 + OH \leftrightarrows C_2H_5 + H_2O \tag{2.33}$$

$$C_2H_6 + H_2O \leftrightarrows C_2H_5 + H_2O_2 \tag{2.34}$$

$$C_2H_6 + CH_3 \leftrightarrows C_2H_5 + CH_4 \tag{2.35}$$

Finally, the reaction of decomposition of ethane has been reinvestigated recently using shock tube experiments [137].

$$C_2H_6\,(+M) \leftrightarrows 2\,CH_3\,(+M) \tag{2.36}$$

The new rate constant has been used in the mechanism.

2.2.2 C_3 and C_4 Chemistry

While the orginal GRI-MECH v3.0 already included a skeleton mechanism for the combustion of propane, the mechanism did not include the formation of smaller C_3 species like propene (C_3H_6), propyne ($HCCCH_3$) and allene (CH_2CCH_2). The mechanism developed by Eiteneer and Frenklach [52] already includes propene, the C_3H_4 isomers, and most of the high temperature reactions important for C_3 species. This mechanism has been supplemented by a C_4 submechanism taken from Hidaka et *al.* [74] and Laskin et *al.* [103]. Some of the reactions have been updated while others have been added to account for more recent data. Only a brief description of the main reactions will be given here.

C_3 Chemistry

The formation of C_3 species from small hydrocarbons is achieved through a series of reactions. Davis et *al.* [46] proposed the methyl addition to acetylene which leads to the formation of both C_3H_4 and C_3H_5 isomers

$$C_2H_2 + CH_3 \leftrightarrows p-C_3H_4 + H \tag{2.37}$$

$$\leftrightarrows a-C_3H_4 + H \tag{2.38}$$

$$\leftrightarrows a-C_3H_5 \tag{2.39}$$

$$\leftrightarrows s-C_3H_5 \tag{2.40}$$

$$\leftrightarrows t-C_3H_5 \tag{2.41}$$

Blitz et *al.* [15] observed the formation of propargyl radicals from the reaction of acetylene with triplet methylene radicals

$$C_2H_2 + 3-CH_2 \leftrightarrows C_3H_3 + H \tag{2.42}$$

Stoliarov et *al.* [180] studied the C_3H_6 potential energy surface and considered several reactions

$$C_3H_6 \leftrightarrows C_2H_3 + CH_3 \tag{2.43}$$

$$C_3H_6 \leftrightarrows a-C_3H_5 + H \tag{2.44}$$

$$C_2H_3 + CH_3 \leftrightarrows a-C_3H_5 + H \tag{2.45}$$

The rate constants for these later reactions were fitted at P = 1.33 bar in the temperature range 500 K-2400 K. More recently, Oehlschlaeger et *al.* [137] measured from shock tube experiments the rate constant of the propane decomposition to ethyl and

methyl radicals

$$C_3H_8\,(+M) \leftrightarrows C_2H_5 + CH_3\,(+M) \tag{2.46}$$

Recently, the C_3H_4 potential energy surface has been investigated by Miller and Klippenstein [120]. Four main reactions have been considered and the rate constants from [120] are used in the current mechanism

$$C_3H_3 + H \leftrightarrows C_3H_2 + H_2 \tag{2.47}$$

$$\leftrightarrows p\text{-}C_3H_4 \tag{2.48}$$

$$\leftrightarrows a\text{-}C_3H_4 \tag{2.49}$$

$$a\text{-}C_3H_4 \leftrightarrows p\text{-}C_3H_4 \tag{2.50}$$

The most stable form of C_3H_2 resulting from the above reactions was found to be the triplet form. The reaction of propargyl radical with molecular oxygen has been calculated theoretically by Hahn et *al.* [66]. The master equation calculations, in agreement with experiments, suggest that the reaction proceeds as

$$C_3H_3 + O_2 \leftrightarrows CH_2CO + HCO \tag{2.51}$$

at high temperature. The reactions of propargyl radicals with other oxygenated species are unknown and were therefore estimated from similar reactions with acetylene and ethylene. For instance, the following reactions were considered

$$C_3H_3 + OH \leftrightarrows C_2H_3CHO \tag{2.52}$$

$$C_3H_3 + OH \leftrightarrows C_2H_4 + CO \tag{2.53}$$

$$C_3H_3 + OH \leftrightarrows C_3H_2 + H_2O \tag{2.54}$$

$$C_3H_3 + OH \leftrightarrows CH_2O + C_2H_2 \tag{2.55}$$

C_4 Chemistry

The formation of C_4 species from smaller hydrocarbons is achieved through a series of reactions. The reaction of addition of ethynyl on acetylene was already included in the mechanism from Eiteneer and Frenklach [52]. Three possible products were considered

$$C_2H_2 + C_2H \leftrightarrows n-C_4H_3 \tag{2.56}$$

$$\leftrightarrows i-C_4H_3 \tag{2.57}$$

$$\leftrightarrows C_4H_2 + H \tag{2.58}$$

The rate constants for the formation of the C_4H_3 isomers showed a strong temperature dependence. Ceursters et *al.* [28] observed that the addition of ethynyl radicals on acetylene does not exhibit any temperature dependence in the temperature range $295\,\mathrm{K} < \mathrm{T} < 800\,\mathrm{K}$. Furthermore, they found from CCSD(T) calculations that the addition to form $n-C_4H_3$ is barrier-less, thus justifying the absence of temperature dependence. Therefore, only the addition reaction to form $n-C_4H_3$ was considered in the present mechanism and the rate constant measured by Ceursters et *al.* [28] has been used.

The direct addition of hydrogen atoms onto diacetylene molecules has been studied with high quality quantum simulations by Miller and Klippenstein [121]

$$C_4H_2 + H \leftrightarrows n-C_4H_3 \tag{2.59}$$

$$C_4H_2 + H \leftrightarrows i-C_4H_3 \tag{2.60}$$

Recently, Senosiain et *al.* [166] studied the reaction of hydroxyl radical with diacetylene. In addition to the hydrogen abstraction path, they found that the reaction could

lead to the formation of two stable species C_3H_3 and C_4H_2O. In the current mechanism, the second minor pathway (C_4H_2O) has been lumped with the first (C_3H_3) as the reaction of decomposition of C_4H_2O are unknown

$$C_4H_2 + OH \leftrightarrows C_4H + H_2O \tag{2.61}$$

$$\leftrightarrows C_3H_3 + CO \tag{2.62}$$

Reactions of simple radicals (H, OH, O) with diacetylene and vinylacetylene have been updated by considering similar reactions with acetylene and ethylene molecules.

Most of the reactions forming other C_4 species have been updated in light of recent quantum simulations. For instance, Miller et *al.* [122] studied the reaction of addition of acetylene with vinyl radicals. They found that this reaction proceeds first through the formation of the $n-C_4H_5$ radicals

$$C_2H_3 + C_2H_3 \leftrightarrows n-C_4H_5 \tag{2.63}$$

The reaction of vinyl addition onto ethylene has been studied by Shestov et *al.* [174]

$$C_2H_4 + C_2H_3 \leftrightarrows 1,3-C_4H_6 + H \tag{2.64}$$

The rates of reaction computed from quantum calculations have been used for these two reactions.

Finally, the reactions of molecular oxygen with butadienyl radicals were derived

Name	Formula	$C_p^\circ(298K)$	$S^\circ(298K)$	$\Delta H_f^\circ(298K)$	
Cyclopentadiene	C_5H_6	**76.66**	**274.82**	134.30	Ref. [184]
Cyclopentadienyl	C_5H_5	**80.51**	264.43	261.50	Ref. [184]
Cyclopentadienone	C_5H_4O	**84.18**	**291.26**	55.23	Ref. [195]
Benzoquinone	OC_6H_4O	**109.67**	**324.95**	−115.90	Ref. [53]
Toluene	A_1CH_3	**105.42**	**321.47**	50.00	Ref. [199]
Benzyl	A_1CH_2	**108.44**	**316.61**	207.00	Ref. [199]
Benzaldehyde	A_1CHO	**112.08**	**335.94**	−37.20	Ref. [199]
Alcoxy-benzyl	A_1CH_2O	**116.99**	**359.90**	**122.42**	Iso. Reac.
Cresol radical	OA_1CH_3	**119.22**	**349.13**	**15.23**	Iso. Reac.

Table 2.11: Thermochemical properties of key aromatic species at $T = 298\,\mathrm{K}$ (re-computed quantities in bold). Heat capacity and entropy in J/mol/K and heat of formation in kJ/mol.

from similar reactions with vinyl radical

$$n\text{−}C_4H_5 + O_2 \leftrightarrows C_4H_4 + HO_2 \tag{2.65}$$

$$\rightarrow a\text{−}C_3H_5 + CO + O \tag{2.66}$$

$$\leftrightarrows HCO + C_2H_3CHO \tag{2.67}$$

$$i\text{−}C_4H_5 + O_2 \leftrightarrows C_4H_4 + HO_2 \tag{2.68}$$

2.2.3 Aromatic Chemistry

A base mechanism for the combustion of aromatic species has been derived from the work of Djurisic and Wang [50, 49] for the oxidation of benzene, the work of Zhong and Bozzeli [207, 208] for the oxidation of cyclopentadiene and the work of Oeschlaeger et *al.* [136] for the oxidation of toluene.

Thermochemical properties

The thermochemical properties of most of the species involved in the combustion of cyclopentadiene, benzene, and toluene were taken from the compilation of Burcat and

Ruscic [21]. However, the results showed large sensitivities to the values for some of these species. As a consequence, the thermochemical properties of the most sensitive species have been updated from the literature or from quantum simulations.

The approach used here follows the methodology previously used to derived the thermochemical properties of Polycyclic Aromatic Hydrocarbons (PAH). When experimental measurements of the enthalpies and/or entropies of formation are available, these values were used in place of the G3MP2//B3 predictions. The G3MP2//B3 predicted values show some systematic errors of a few kJ/mol when compared to the experimental data. Therefore, when no experimental values were available, to improve the predictions of the enthalpy of formation, corrections based on isodesmic reactions were applied as previously done by Wang and Brezinsky [195] for cyclopentadiene derivatives. Table 2.11 lists the thermochemical properties of the most sensitive species that were recomputed.

Among these species, the couple cyclopentadiene/cyclopentadienyl radical plays a significant role. The cyclopentadienyl radical is a typical example of a first-order Jahn-Teller distorted molecule. Two stable C_{2v} conformations with almost the same energy can be found: $^2B_1$ and $^2A_2$. Tokmakov et *al.* [184] studied this radical using quantum simulations and estimated the thermodynamic properties of the cyclopentadiene molecule and its radical. A proper consideration of this distortion is necessary to accurately predict the equilibrium constant between the molecule and its radical. For this reason, the thermodynamic properties and the rate constant for the reconversion of cyclopentadienyl into cyclopentadiene were taken from Tokmakov et *al.* [184].

Cyclopentadiene Chemistry

Most of the reactions for the chemistry of cyclopentadiene were taken from the work of Zhong and Bozzelli [207, 208]. However, some key reactions for the cyclopentadiene pyrolysis have been updated. The rate for the reactions of hydrogen atoms with

cyclopentadiene were taken from Roy [156]

$$C_5H_6 + H \leftrightarrows C_5H_5 + H_2 \tag{2.69}$$

$$C_5H_6 + H \leftrightarrows a-C_3H_5 + C_2H_2 \tag{2.70}$$

The rate for the recombination of propargyl radicals with acetylene molecules is taken from Knyazev and Slagle [97]

$$C_3H_3 + C_2H_2 \leftrightarrows C_5H_5 \tag{2.71}$$

The recombination of cyclopentadienyl radicals has been studied recently both experimentally [129] and numerically [93]. Marinov et *al.* [109] suggested that naphthalene was the main product formed from this reaction. Recently, Kislov and Mebel [93] found that this reaction leads to the formation of naphthalene at low temperatures and fulvalene at high temperatures. Their branching ratio together with the total rate constant from Murakami et *al.* [129] has been used for the naphthalene pathway which is of key importance for larger PAH formation

$$C_5H_5 + C_5H_5 \rightarrow C_{10}H_8 + 2H \tag{2.72}$$

The oxidation of cyclopentadiene leads to the formation of several intermediate species like cyclopentadienoxy radicals ($1,3-C_5H_5O$ and $2,4-C_5H_5O$), cyclopentadienone (C_5H_4O), and vinyl ketene (C_4H_4O). Reaction rates for those species were estimated from similar reactions with smaller hydrocarbon molecules.

Benzene Chemistry

In the current mechanism, the formation of benzene molecules occurs following two pathways. The first pathway, originally investigated by Wang and Frenklach [197],

corresponds to the acetylene addition onto C_4H_3 or C_4H_5 radicals. Recently, high fidelity ab-initio calculations have been performed by Senosiain and Miller [170] on the acetylene addition onto the C_4H_5 isomers. The reaction with $n-C_4H_5$ was found to produce mainly benzene and fulvene ($C_5H_4CH_2$)

$$n-C_4H_5 + C_2H_2 \leftrightarrows C_5H_4CH_2 + H \tag{2.73}$$

$$\leftrightarrows C_6H_6 + H \tag{2.74}$$

while the reaction with $i-C_4H_5$ was found to produce mainly fulvene

$$i-C_4H_5 + C_2H_2 \leftrightarrows C_5H_4CH_2 + H \tag{2.75}$$

Other linear C_6H_6 molecules are formed during these reactions especially at higher temperatures ($T > 2000\,\mathrm{K}$), but were not considered in the present mechanism. The reactions of acetylene with the C_4H_3 isomers were assumed to follow the same mechanism as for the C_4H_5 isomers, and produce phenyl and fulvenyl radicals

$$n-C_4H_3 + C_2H_2 \leftrightarrows C_5H_4CH \tag{2.76}$$

$$\leftrightarrows C_6H_5 \tag{2.77}$$

$$i-C_4H_3 + C_2H_2 \leftrightarrows C_5H_4CH \tag{2.78}$$

The second pathway towards the formation of benzene molecules is the self-recombination of propargyl radicals (C_3H_3) or the reaction of propargyl radicals with allyl radicals ($a-C_3H_5$). These resonantly stabilized free radicals (RSFR) are usually found in significant concentrations in flames. Miller and Klippenstein [117] studied the C_6H_6

potential energy surface and found the following reactions to be important

$$C_3H_3 + C_3H_3 \leftrightarrows C_5H_4CH_2 \tag{2.79}$$
$$\leftrightarrows C_6H_6 \tag{2.80}$$
$$\leftrightarrows C_6H_5 + H \tag{2.81}$$
$$C_5H_4CH_2 \leftrightarrows C_6H_6 \tag{2.82}$$
$$\leftrightarrows C_6H_5 + H \tag{2.83}$$

One additional molecule, the 2-ethynyl-1,3-butadiene, was found important. However, this species isomerizes fast into fulvene. Thus, its reaction of formation has been lumped with that of fulvene. Finally, the reaction of propargyl with allyl radicals is assumed to follow

$$C_3H_3 + a-C_3H_5 \rightarrow C_6H_6 + 2H \tag{2.84}$$

This reaction has been assigned the total rate constant of the propagyl recombination at one atmosphere.

The base mechanism for the oxidation of benzene was taken from the work of Djurisic and Wang [50]. Several reactions have been changed and updated in light of newer experimental measurements or ab-initio calculations. For instance, the reaction of benzene with OH radical have been investigated by Tokmakov and Lin [182] and Seta et *al.* [171]

$$C_6H_6 + OH \leftrightarrows C_6H_5 + H_2O \tag{2.85}$$
$$\leftrightarrows C_6H_5OH \tag{2.86}$$

The rate for oxygen addition to benzene is assumed to follow two pathways

$$C_6H_6 + O \leftrightarrows C_6H_5O + H \tag{2.87}$$

$$\leftrightarrows C_6H_5OH \tag{2.88}$$

The total rate constant has been investigated recently by Nguyen et *al.* [133]. However, the branching ratio between the two pathways is not known. Therefore, equipartition was assumed between the two pathways as suggested by Baulch et *al.* [11]. The reaction of decomposition of phenol has been investigated by Xu and Lin [203]

$$C_6H_5OH \leftrightarrows C_6H_5O + H \tag{2.89}$$

$$\leftrightarrows C_5H_6 + CO \tag{2.90}$$

Finally, the rate of phenoxy radical decomposition has been studied experimentally by Murakami et *al.* [128]

$$C_6H_5O \leftrightarrows C_5H_5 + CO \tag{2.91}$$

Toluene Chemistry

Similarly to benzene, the base mechanism for toluene oxidation has been derived from the work of Oehlschlaeger et *al.* [136]. Some reactions have been updated to account for newer results. For instance, the reaction of toluene decomposition has been recently studied by Klippenstein et *al.* [95]

$$C_6H_5CH_3 \leftrightarrows C_6H_5 + CH_3 \tag{2.92}$$

$$\leftrightarrows C_6H_5CH_2 + H \tag{2.93}$$

$$C_6H_5CH_2 + H \leftrightarrows C_6H_5 + CH_3 \tag{2.94}$$

Another key reaction is the decomposition of benzyl. Benzyl is assumed to produce cyclopentadienyl radical and acetylene

$$C_6H_5CH_2 \leftrightarrows C_5H_5 + C_2H_2 \tag{2.95}$$

Other products like a linear C_7H_6 or vinylacetylene (C_4H_4) plus propargyl have been suggested in the literature for the decomposition of the benzyl radical [135, 87]. However, these reactions were not considered in the current mechanism, as the reverse reaction of acetylene addition onto cyclopentadienyl radicals was found to produce the C_7H_7 radical [97]. The reaction rate measured by Oehlschlaeger et *al.* [135] has been used for the reaction of benzyl decomposition.

As a resonantly stabilized free radical (RSFR), the benzyl radical is very stable, and is found in significant concentration in flames. Furthermore, its chemical structure is very similar to that of allyl radicals. As suggested by McEnally et *al.* [112], benzyl radicals can react with propargyl to form naphthalene

$$C_6H_5CH_2 + C_3H_3 \rightarrow C_{10}H_8 + H_2 \tag{2.96}$$

The real product of the above reaction should be a $C_{10}H_{10}$ species. Through fast H-abstraction reactions, this molecule is assumed to transform into naphthalene. The rate of the reaction of allyl radicals with propargyl has been used for this reaction. This pathway was found to be a significant source of naphthalene molecules.

Other reactions relevant to the oxidation of toluene have been updated. The

reaction of OH radical with toluene is assumed to follow three pathways

$$C_6H_5CH_3 + OH \leftrightarrows C_6H_5CH_2 + H_2O \quad (2.97)$$

$$\leftrightarrows C_6H_4CH_3 + H_2O \quad (2.98)$$

$$\leftrightarrows C_6H_5OH + CH_3 \quad (2.99)$$

The rate for H-abstraction from the methyl group of toluene has been taken from Vasudevan et *al.* [190], while the H-abstraction and the H-substitution from the phenyl group were taken from Seta et *al.* [171]. Recently, Choi et *al.* [31] studied the decomposition of the $C_6H_5CH_2O$ radical on the C_7H_7O potential energy surface and considered the following reactions

$$C_6H_5CH_2O \leftrightarrows C_6H_5CHO + H \quad (2.100)$$

$$C_6H_5 + CH_2O \leftrightarrows C_6H_6 + HCO \quad (2.101)$$

$$\leftrightarrows C_6H_5CHO + H \quad (2.102)$$

$$\leftrightarrows C_6H_5CH_2O \quad (2.103)$$

The rates derived by ab-initio calculations were used while the rates for the reaction of C_6H_5CHO were taken from similar reactions with CH_3CHO. Finally, cresol molecules were considered and the rates for the relevant reactions were taken from the chemistry of benzene and phenol molecules.

2.2.4 Large PAH chemistry

In order to be used in soot models, the kinetic scheme is supplemented by a mechanism for the growth of Polycyclic Aromatic Hydrocarbon (PAH) molecules beyond benzene. This mechanism is based on several reactions pathways. The first path corresponds to the HACA mechanism [59]. Aromatic rings composed of six carbon atoms are formed

from the successive addition of two acetylene molecules. The rate of acetylene addition on a radical molecule like phenyl or naphthyl is taken from Kislov and Mebel [92].

The second path is the addition of propargyl radicals on substituted aromatic molecules [42, 112]. For instance, napthalene can be formed by the addition of propargyl on a benzyl radical. The rate of propargyl addition is taken from Miller and Klippenstein [117].

The third path is the addition of vinylacetylene (C_4H_4) on an aromatic radical followed by direct cyclization [126, 2]. The channel entrance rate computed by Aguilera-Iparraguirre and Klopper [2] has been used in the mechanism.

The fourth path corresponds to the recombination of cycloptenadienyl radicals to form naphthalene, or the reaction of cyclopentadienyl and indenyl radicals to form phenanthrene [42].

Finally, the formation of cyclo-pentafused aromatics (CP-PAH) from other PAH molecules has been considered for napthalene, phenanthrene, and pyrene. The reaction rate for the relevant reactions were taken from recent work by Kislov and Mebel [92]. Once formed, these CP-PAH molecules are subject to the exact same reactions than the other PAH molecules.

2.2.5 N-Heptane and Iso-Octane Chemistry

The description of the *n*-heptane and *iso*-octane combustion chemistry has been taken from the Lawrence Livermore National Laboratories (LLNL) mechanisms developed for *n*-heptane by Curran et *al.* [38] and for *iso*-octane by Curran et *al.* [39]. However, these mechanisms are very large and include many species and reactions relevant to the low temperature oxidation of hydrocarbons, that are not important for the high temperature conditions considered in this work. To remove the low temperature chemistry and negligible chemical paths, both the *n*-heptane and *iso*-octane mechanisms were reduced independently using the Directed Relation Graph Method with

Error Propagation (DRGEP) developed by Pepiot-Desjardins and Pitsch [145]. Reduction was performed for the homogeneous, isochoric and adiabatic auto-ignition of mixtures of fuel and air, for temperatures between 1000 and 2000 K, pressures between 1 and 40 bar and equivalence ratios ranging from 0.5 to 2. The targets used for the reduction included the ignition delay time, fuel, oxidizer, and main combustion products. The DRGEP reduction procedure was complemented by appropriate species and reactions lumping, guided by a thorough reaction flux analysis.

Because the resulting skeletal mechanisms have species and reactions in common that are already included in the mechanism developed in the previous sections, the schemes must be combined carefully. The following rules were applied: Any species or reactions not already present in the current mechanism were simply added. Additionally, when identical reactions were available, the reactions of the current mechanism were preferred over the reactions from the skeletal LLNL mechanisms. The resulting final mechanism consists of 151 species and 1658 reactions, forward and backward reactions being counted separately, of which 14 species and 84 reactions come from the *n*-heptane LLNL mechanism and 14 species and 73 reactions from the *iso*-octane LLNL mechanism.

2.3 Validation Results

Laminar burning velocities and ignition delay times were chosen as targets for the validation of the presented chemical mechanism. The combination of these data provides a good test for the developed mechanism. These two cases also represent possible modes of combustion often found in engines: flame front propagation and local thermal ignition. Note that, although the low temperature auto-ignition chemistry for iso-octane and *n*-heptane has been neglected, and consequently will not be

tested here, it is straightforward to extend the mechanism by including the appropriate reactions from the LLNL detailed chemical schemes. All numerical simulations have been performed with the FlameMaster code V3.4 [147]. More details about the FlameMaster code can be found in the Appendix C.

2.3.1 Ignition Delay Times

In order to validate the mechanism over a large range of equivalence ratios, auto-ignition simulations, modeled by isochoric and adiabatic homogeneous reactors, are performed for lean ($\phi = 0.5$), stoichiometric ($\phi = 1.0$), and rich ($\phi = 2.0$) mixtures for conditions and fuels where experimental data are available. Most of the simulations were done around atmospheric pressure, with the exception of those for *n*-heptane and *iso*-octane which were done at much higher pressures (up to 40 bar). When several experimental data sets exist for the same equivalence ratio and pressure, the most recent data set is used.

Small Hydrocarbons

The experimental data for the ignition delay times of small hydrocarbons were taken from Seery and Bowman [163] for methane combustion, from Hidaka et *al.* [73] ($\phi = 2.0$) and Rickard et *al.* [155] ($\phi = 0.5$ and $\phi = 1.0$) for acetylene combustion, from Hidaka et *al.* [75] ($\phi = 0.5$ and $\phi = 2.0$) and Horning [79] ($\phi = 1.0$) for ethylene combustion, and from de Vries et *al.* [47] for ethane combustion.

Figure 2.8 shows the ignition delay times for the small hydrocarbons predicted with the current mechanism. For methane, acetylene, and ethylene, the ignition delay times compare very well with the experimental data. On the other hand, the computed ignition delay times for ethane show slight deviations from the experimental measurements. The overall activation energy predicted by the mechanism is lower

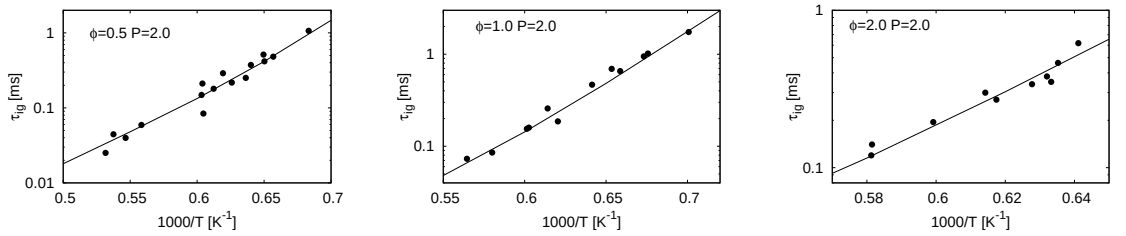

(a) Methane (CH_4)

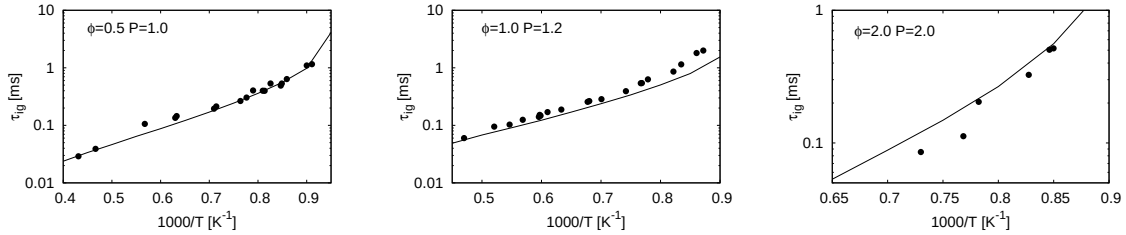

(b) Acetylene (C_2H_2)

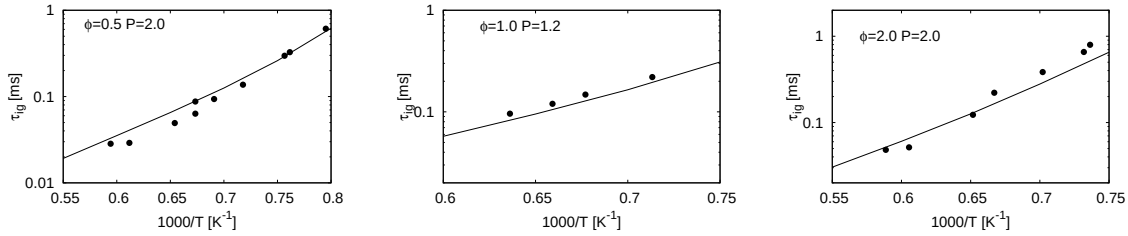

(c) Ethylene (C_2H_4)

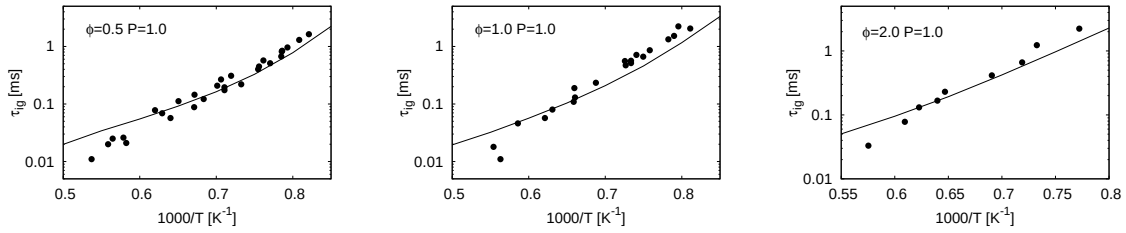

(d) Ethane (C_2H_6)

Figure 2.8: Ignition delay times for small hydrocarbons. References for experimental data are given in the text.

than the measured activation energy. However, the experimental measurements suffer from some scatter and the overall prediction remains very good.

C_3 and C_4 Species

The experimental data for the ignition delay times for C_3 and C_4 species are taken from Curran et *al.* [36] for propyne and allene combustion, from Qin et *al.* [153] for propene combustion, from Brown and Thomas [19] ($\phi = 1.0$) and Burcat et *al.* [20] ($\phi = 0.5$ and $\phi = 2.0$) for propane combustion, and from Libby et *al.* [106] ($\phi = 0.5$ and $\phi = 1.0$) and Fournet et *al.* [55] ($\phi = 1.38$) for butadiene combustion. The ignition delay times for lean and rich propane as well as for rich butadiene mixtures were performed at a slightly higher pressure than the other simulations ($P \approx 10\,\text{bar}$).

Figure 2.9 shows the ignition delay times predicted with the current mechanism. In spite of a short chemical mechanism for the combustion of the C_3 and C_4 species, the comparison of the results of the numerical simulations with the experimental values is very good in almost all cases. Butadiene ignition at high pressure ($P = 10\,\text{bar}$) and rich mixtures show some errors. The rate constants for several reactions relevant to the combustion of butadiene were taken from quantum calculations at atmospheric pressure [198]. These rates might be inaccurate for higher pressures and therefore should be revised for application in high pressure systems.

Aromatics

Experimental data for the ignition delay times for the two aromatic species are taken from Burcat et *al.* [22] for benzene combustion and from Burcat et *al.* [22] ($\phi = 0.33$ and $\phi = 1.0$) and Pengloan [144] ($\phi = 1.5$) for toluene combustion.

Figure 2.10 shows the ignition delay times predicted with the current mechanism. For both benzene and toluene, the ignition delay times for stoichiometric mixtures are in excellent agreement with the experimental measurements. However, there are

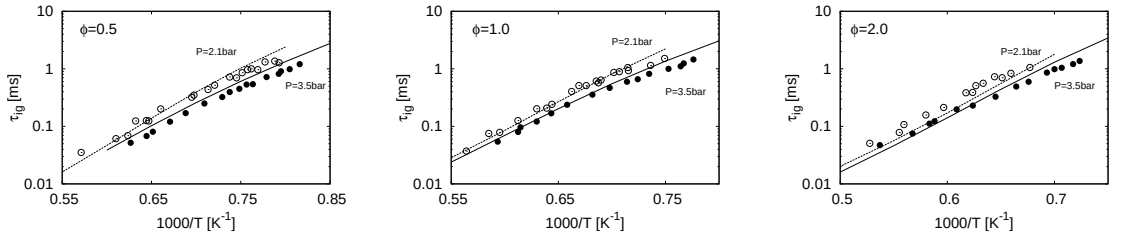

(a) C_3H_4 isomers : propyne (•, –) and allene (◦, ––)

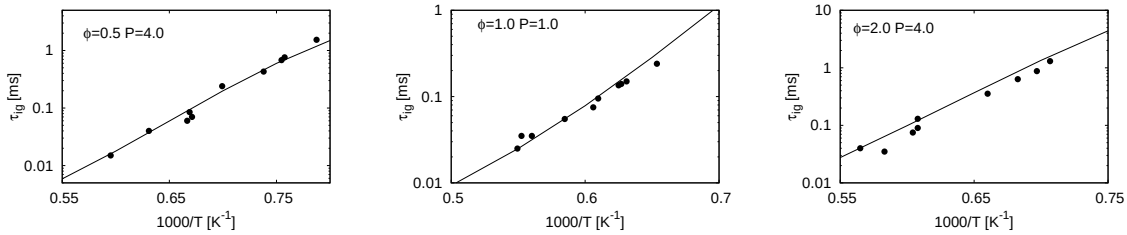

(b) Propene (C_3H_6)

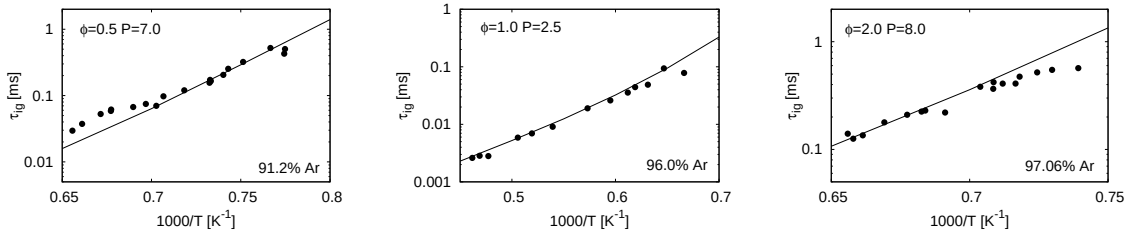

(c) Propane (C_3H_8)

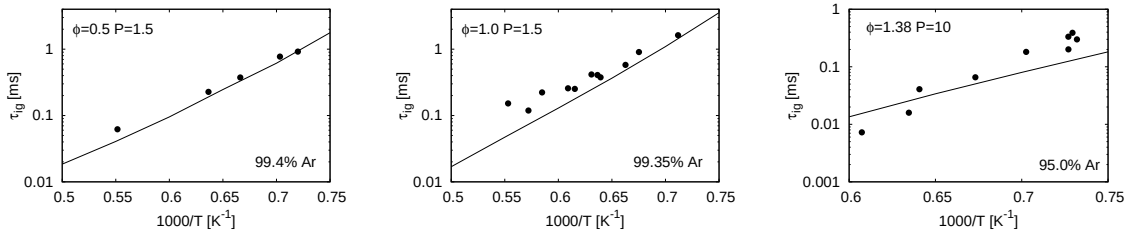

(d) 1,3-Butadiene (C_4H_6)

Figure 2.9: Ignition delay times for C_3 and C_4 hydrocarbons. References for experimental data are given in the text.

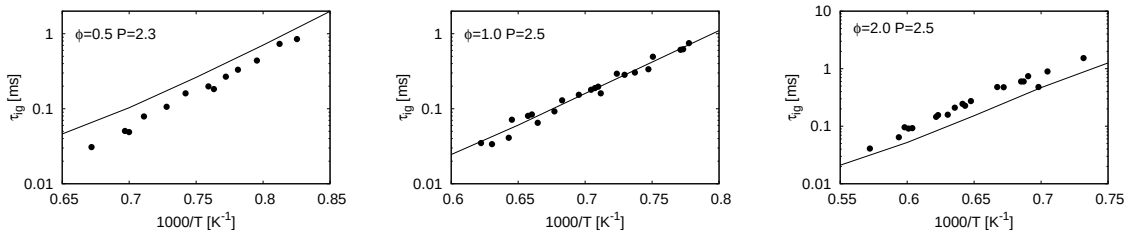

(a) Benzene (A_1)

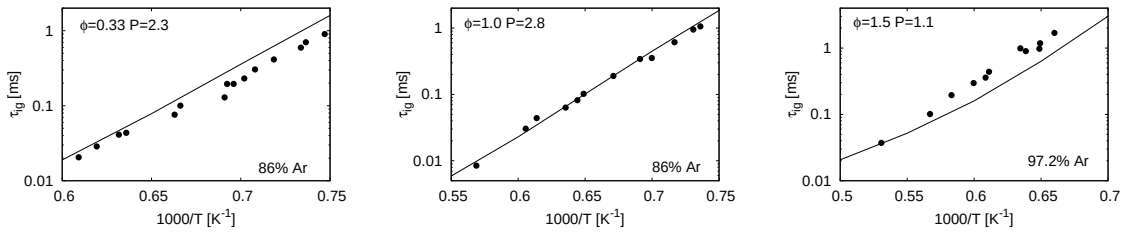

(b) Toluene (A_1CH_3)

Figure 2.10: Ignition delay times for aromatic species. References for experimental data are given in the text.

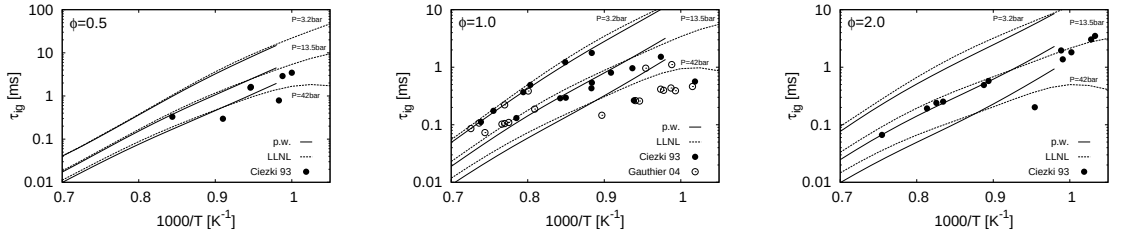

(a) *n*-heptane (C_7H_{16})

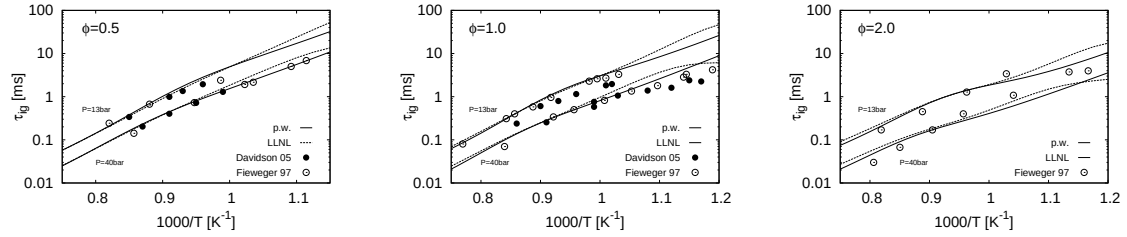

(b) *iso*-octane (C_8H_{18})

Figure 2.11: Ignition delay times for larger alkanes in air. References for experimental data are given in the text.

some errors for lean and rich mixtures. Lean mixtures tend to ignite too late while rich mixtures tend to ignite too early. Altough, the model correctly captures the trend of increasing ignition delay times for richer mixtures, this dependance is found to be too weak for the present chemical scheme. Since toluene exhibits the same tendency as benzene, one could stipulate that these discrepancies originate in the description of the reactions on the aromatic ring. Given the large experimental uncertainties in several key reactions and the lack of conclusive ab-initio calculations, the results remain very good (less than 50% relative error for lean and rich mixtures).

N-Heptane and Iso-Octane

The experimental data for the ignition delay times of *n*-heptane were taken from Ciezki et *al.* [32] and Gauthier et *al.* [62]. The ignition delay times of Gauthier et *al.* [62] were rescaled to $P = 3.2\,\text{bar}$, $P = 13.5\,\text{bar}$, and $P = 42\,\text{bar}$ as suggested in Ref. [62]. For *iso*-octane, the data were taken from Fieweger et *al.* [54] and Davidson et *al.* [44].

Figure 2.11 shows the ignition delay times predicted with the current model and with the original chemical mechanisms from Curran et *al.* [38, 39]. Since the *n*-heptane and *iso*-octane chemistry of the current mechanism comes from the LLNL mechanisms, the ignition delay times are expected to be very close to thsoe predicted with the detailed LLNL mechanisms. Furthermore, as the low temperature chemistry was removed during the chemical reduction, only ignition delay times at high temperatures are shown.

As expected, the ignition delay times for *iso*-octane combustion are in close aggrement with those predicted with the detailed LLNL mechanism. Furthermore, the comparison with experimental measurements is very good. Similar conclusions can be drawn for heptane combustion. For lean mixtures, the ignition delay times predicted with the current mechanism and the LLNL mechanism are the same. As the

equivalence ratio increases, the differences between the two mechanisms increase. It should be noted that these differences arise from the combination of the *n*-heptane and *iso*-octane mechanisms with a different base scheme, and not from the reduction of the original mechanisms. The current mechanism predicts ignition delay times usually lower than the LLNL mechanism. However, these predictions are closer to the experimental measurements, and the error is hence within the predictive accuracy of the original mechanism.

2.3.2 Laminar Burning Velocities

Laminar burning velocities were computed numerically for all fuels where experimental data are available and compared to measurements. Most of the calculations were done at atmospheric pressure and room temperature. Some additional cases were simulated at higher temperatures (up to 450 K) and pressures (up to 25 bar).

Small Hydrocarbons

The experimental values for the laminar burning velocities for small hydrocarbon fuels were taken from several data sets including Vagelopoulos and Egolfopoulos [188], van Maaren et *al.* [189], Hassan et *al.* [70], Egolfopoulos et *al.* [51], Hirasawa et *al.* [76], Rozenchan et *al.* [157], and Jomaas et *al.* [86].

Figure 2.12 shows the burning velocities for methane, acetylene, ethylene, and ethane. The overall agreement with experimental data is excellent for all cases except for acetylene. The burning velocities predicted for lean mixtures lie right between the two experimental data sets. For stoichiometric to rich mixtures, there is a significant scatter in the experimental data points. However, it should be noted that the flame speeds computed with the current mechanism compare relatively well with the latest measurements of Jomaas et *al.* [86].

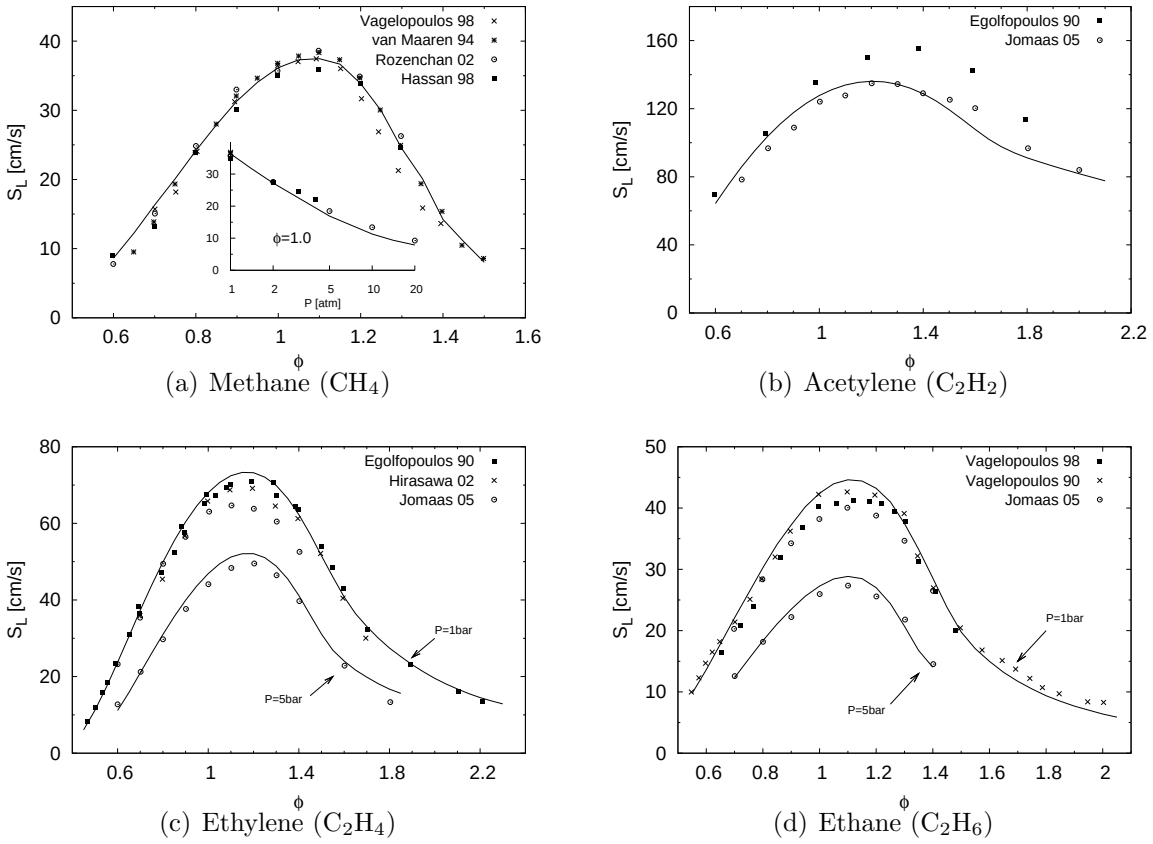

(a) Methane (CH_4)

(b) Acetylene (C_2H_2)

(c) Ethylene (C_2H_4)

(d) Ethane (C_2H_6)

Figure 2.12: Laminar burning velocities of small hydrocarbons. References for experimental data are given in the text.

For the three other fuels (methane, ethylene, and ethane), the comparison with experiment is very good. Combustion of both lean and rich mixtures is correctly represented. The flame speeds of ethane at an equivalence ratio above $\phi = 1.5$ are slightly lower than those measured by Egolfopoulos and Vagelopoulos [51]. However, more recent experimental measurements [188, 86] tend to suggest that these values are slightly over-estimated.

Finally, the effect of pressure on the burning velocities for methane, ethylene, and ethane mixtures is correctly represented. The decrease of the burning speed with pressure is well captured for methane flames.

C_3 and C_4 Species

The burning velocities data of C_3 and C_4 hydrocarbons used here are from several experimental sources: Davis and Law [45], Vagelopoulos and Egolfopoulos [188, 51], and Jomaas et *al.* [86]. With the exception of propyne (18% of O_2 in N_2), all laminar flame speeds were evaluated with air.

Figure 2.13 shows the laminar burning velocities of propyne, propene, propane, and butadiene. The calculated values compare very well with the experimental data for the different fuels but propene and the two pressures considered. In the case of propene, the flame speeds of lean mixtures agree well with the experimental values of Davis and Law [45]. However, experimental data points show for rich mixtures significant scatter. The current mechanism stands between the two experimental data sets of Davis and Law [45] and Jomaas et *al.* [86].

Aromatics

The burning velocities of benzene and toluene are from two data sets. Davis and Law [45] measured the laminar flame speed at atmospheric pressure and room temperature. Johnston and Farrel [85] performed similar measurements at higher pressure

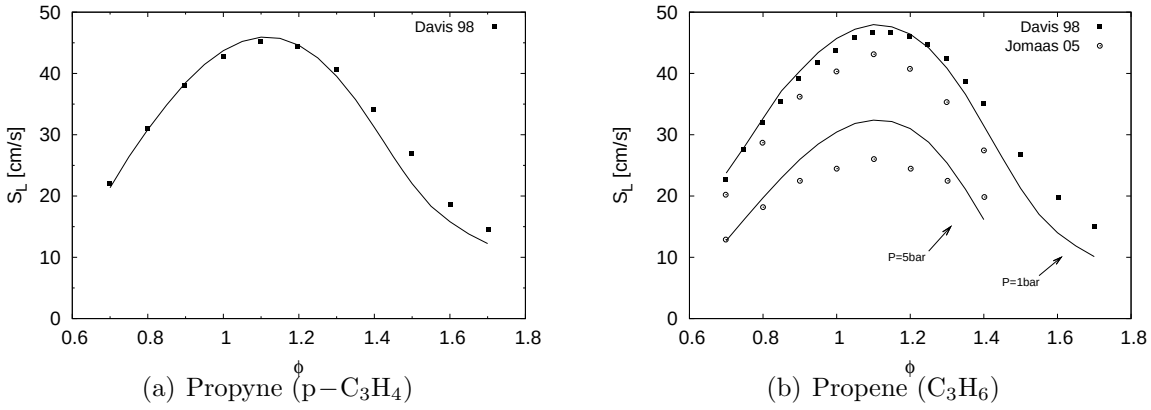

(a) Propyne ($p-C_3H_4$) (b) Propene (C_3H_6)

(c) Propane (C_3H_8) (d) 1,3-Butadiene (C_4H_6)

Figure 2.13: Laminar burning velocities of C_3 and C_4 hydrocarbons. References for experimental data are given in the text.

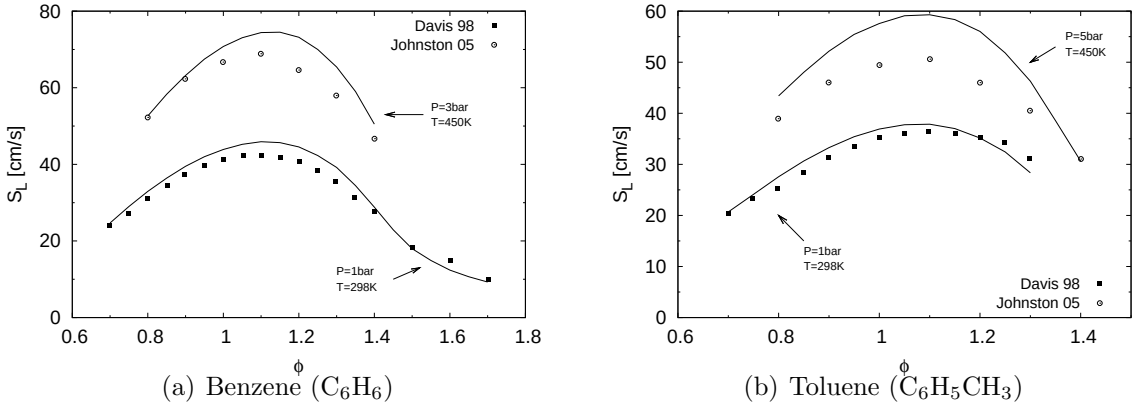

(a) Benzene (C_6H_6) (b) Toluene ($C_6H_5CH_3$)

Figure 2.14: Laminar burning velocities of aromatic hydrocarbons. References for experimental data are given in the text.

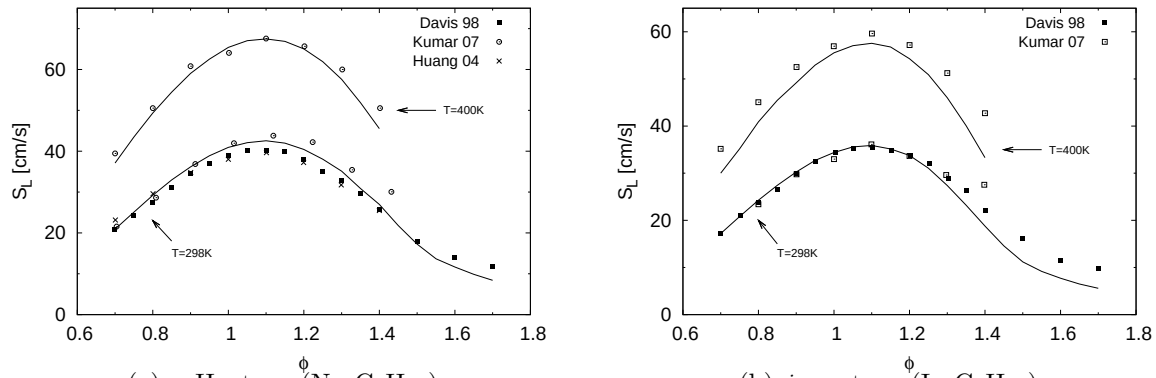

(a) *n*-Heptane ($\mathrm{N-C_7H_{16}}$) (b) *iso*-octane ($\mathrm{I-C_8H_{18}}$)

Figure 2.15: Laminar burning velocities of *n*-heptane and *iso*-octane. References for experimental data are given in the text.

($P = 5\,\mathrm{bar}$) and higher temperature ($T = 450\,\mathrm{K}$), more relevant to engine configurations.

Figure 2.14 shows the comparison of the calculated laminar burning velocities with the experimental data. The comparison both at low and high pressures is very good for benzene. The burning velocities of toluene are accurately predicted for atmospheric conditions, but they are overestimated for higher pressures and temperatures. Further analysis of the pressure dependance of several reactions relevant to toluene oxidation might be required to explain this overprediction.

N-Heptane and Iso-Octane

The laminar burning velocities for *n*-heptane and *iso*-octane combustion were taken from the results of Davis and Law [45], Kumar et *al.* [101], Huang et *al.* [80], and Johnston and Farrell [85]. Recently, measurements of the laminar burning velocities for high pressures (from 10 bar up to 25 bar) and higher temperatures (373 K) have been performed by Jerzembeck et *al.* [84].

Figure 2.15 shows the comparison of the calculated laminar flame speeds with the experimental measurements. The burning velocities of *n*-heptane are predicted

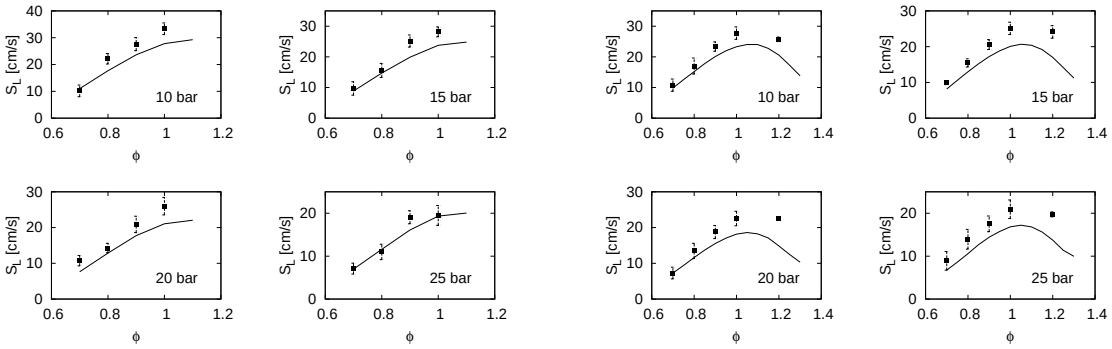

(a) *n*-Heptane ($N-C_7H_{16}$) (b) *iso*-octane ($I-C_8H_{18}$)

Figure 2.16: High pressure laminar burning velocities of *n*-heptane and *iso*-octane ($T = 373\,\mathrm{K}$). Experimental data from Jerzembeck et al. [84].

very accurately for both lean and rich mixtures. The calculated values for *iso*-octane are smaller for rich mixtures when compared to the experimental data of Davis and Law [45]. However, these little discrepancies are not found at higher pressures and temperatures ($T = 450\,\mathrm{K}$ and $P = 3\,\mathrm{bar}$). The increase in the burning velocities due to preheated mixtures ($T = 400\,\mathrm{K}$ and $T = 450\,\mathrm{K}$) is correctly captured for both fuels. Finally, Fig. 2.16 shows the burning velocities predicted for very high pressures from 10 bar to 25 bar. The effects of equivalence ratio and pressure are well captured for *n*-heptane and *iso*-octane mixtures. However, it should be noticed that the predicted burning velocities are consistently smaller than the measured values.

2.4 Soot Precursors in Laminar Flames

In the previous sections, the mechanism has been shown to reproduce the ignition delay times and laminar burning velocities of small and large hydrocarbons with good accuracy. To analyze the capabilities of the mechanism to predict the formation of soot precursors, several laminar premixed and diffusion flames are computed. The emphasis is placed on the prediction of soot precursors like acetylene, allene,

Fuel	ϕ	v_0 [cm/s]	T_0[K]	$T_{\max}$ [K]
n-heptane	1.9	4.98	450	1625
iso-octane	1.9	4.12	450	1772

Table 2.12: Parameters used for the premixed flames of ethylene, *n*-heptane, and *iso*-octane.

propyne, and benzene. A description of the different configurations can be found in Appendix C.

2.4.1 Premixed Flat Flames

Two laminar premixed flat flames are considered: a rich premixed flame of *n*-heptane/air ($\phi = 1.9$) and a rich premixed flame of *iso*-octane/air ($\phi = 1.9$). These two flames were studied experimentally by Bakali et *al.* [8]. Because of unknown heat losses to the burner by conduction and radiation, the temperature profiles were imposed in the calculations. Bakali et *al.* [8] reported the temperature profile measured by thermocouples. However, these temperature measurements suffer from significant uncertainties (about 100 K). As a result, the temperature profiles for the *n*-heptane and *iso*-octane flames were adjusted to match the decay of the fuel and oxydizer profiles. The parameters used for these flames are listed in Table 2.12.

Figures 2.17 and 2.18 show the mole fractions of the different species under consideration. With the temperature profiles adjusted to match the decay of the fuel (*n*-heptane and *iso*-octane) and the oxidizer, the formation of the main products of combustion (CO and CO_2) is correctly reproduced for both flames. The formation of soot precursors like acetylene and benzene compares also very well with experimental data. In both flames, ethylene is formed first directly from the decomposition of the fuel. Then, the ethylene profiles decay as this species is rapidly converted into acetylene. In these alkane flames, the C_3H_4 isomers are formed mainly from the direct decomposition of the fuel through the formation of the allyl radical ($a - C_3H_5$).

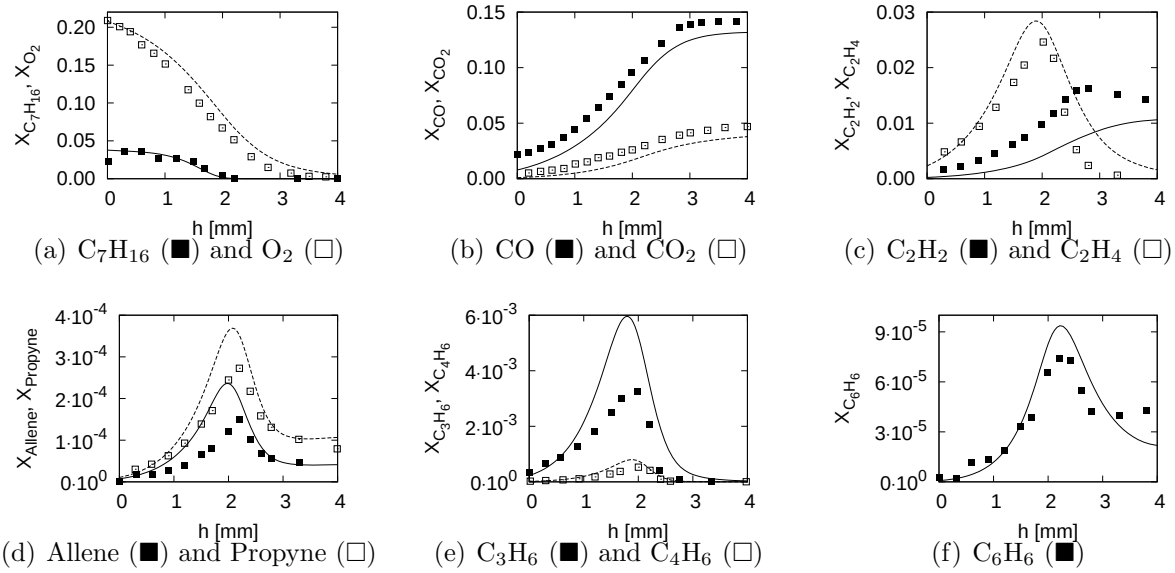

(a) C_7H_{16} (■) and O_2 (□) (b) CO (■) and CO_2 (□) (c) C_2H_2 (■) and C_2H_4 (□)

(d) Allene (■) and Propyne (□) (e) C_3H_6 (■) and C_4H_6 (□) (f) C_6H_6 (■)

Figure 2.17: Mole fractions of main species and soot precursors for the rich *n*-heptane premixed flame. Experimental data from Bakali et *al.* [8]

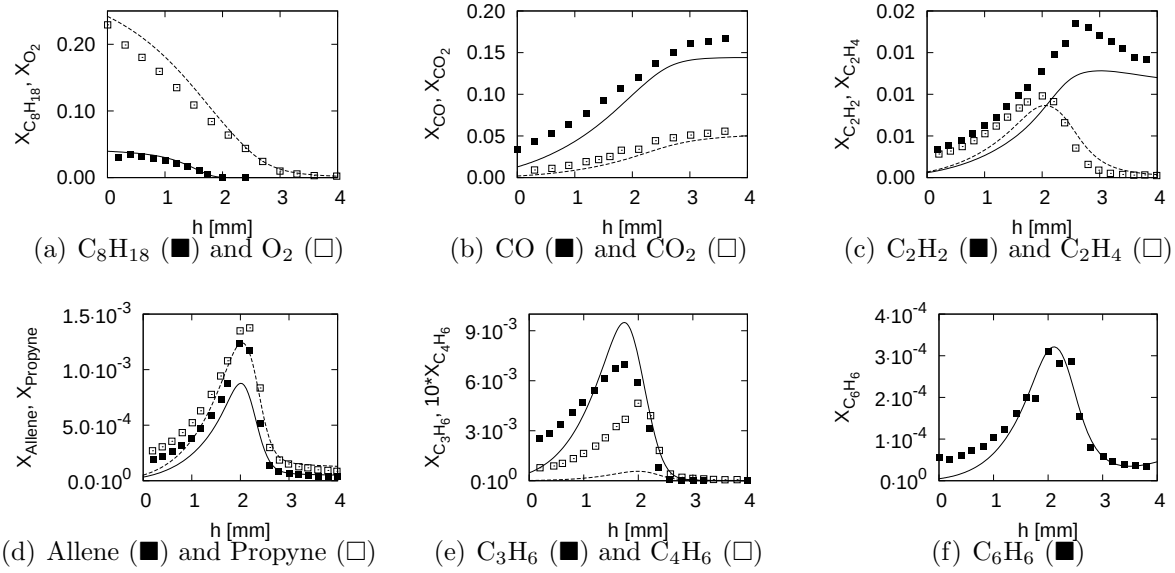

(a) C_8H_{18} (■) and O_2 (□) (b) CO (■) and CO_2 (□) (c) C_2H_2 (■) and C_2H_4 (□)

(d) Allene (■) and Propyne (□) (e) C_3H_6 (■) and C_4H_6 (□) (f) C_6H_6 (■)

Figure 2.18: Mole fractions of main species and soot precursors for the rich *iso*-octane premixed flame. Experimental data from Bakali et *al.* [8]

Then, through H-abstraction reactions, propargyl radicals are rapidly formed. Finally, the first aromatic ring is formed from the recombination of propargyl radicals or the reaction of propargyl and allyl radicals. While present in the mechanism, the reaction of benzene/fulvene formation because of acetylene addition on C_4H_5 radicals was not found to be important.

2.4.2 Counterflow Diffusion Flames

Two counterflow diffusion flames are considered. The first flame is an acetylene/air diffusion flame by Pels-Leusden and Peters [143, 142] with a lean premixed flame ($\phi = 0.63$) on the oxidizer side. The second flame is a *n*-heptane/air diffusion flame by Berta et *al.* [14] with a very rich premixed flame on the fuel side ($\phi = 15$). Contrary to the premixed flames simulated previously, the temperature profiles were not imposed in the current simulations of the diffusion flames. The maximum of the temperature profile occurs away from the two burners, and heat losses to the burners should not be significant.

Figures 2.19 and 2.20 show the mole fraction profiles for the main species and the soot precursors. The decay of the fuels (C_2H_2 and C_7H_{16}) and the oxidizer is correctly represented for both flames, as is the formation of the main products of combustion (CO and CO_2). The predictions for the different soot precursors compare favorably with the experimental data, with the exception of the ethylene profile for the acetylene flame which is underpredicted by a factor of two. In the case of the *n*-heptane diffusion flame, the mole fraction of benzene was measured with two different experimental techniques (filled squares and diamonds). Given the large scatter between these two measurements, the overall agreement with the experimental data for the benzene profile remains reasonable.

For the *n*-heptane diffusion flame, the C_3H_4 isomers are formed from the direct decomposition of the fuel, as was observed in the premixed flame previoulsy presented.

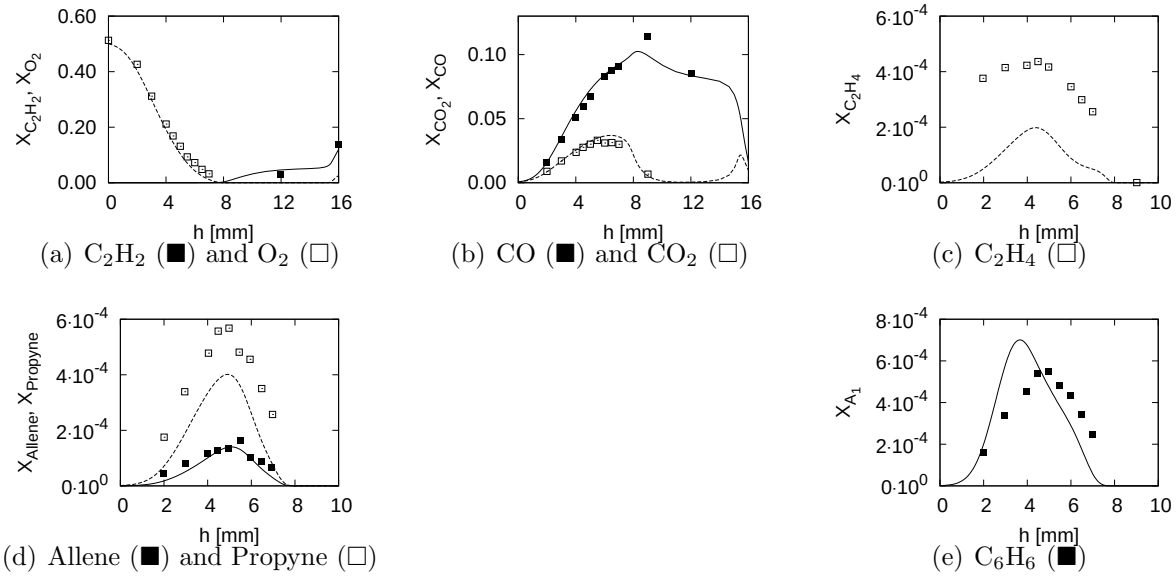

(a) C_2H_2 (■) and O_2 (□) (b) CO (■) and CO_2 (□) (c) C_2H_4 (□)

(d) Allene (■) and Propyne (□) (e) C_6H_6 (■)

Figure 2.19: Mole fractions of main species and soot precursors for the acetylene diffusion flame. Experimental data from Pels Leusden and Peters [143, 142]

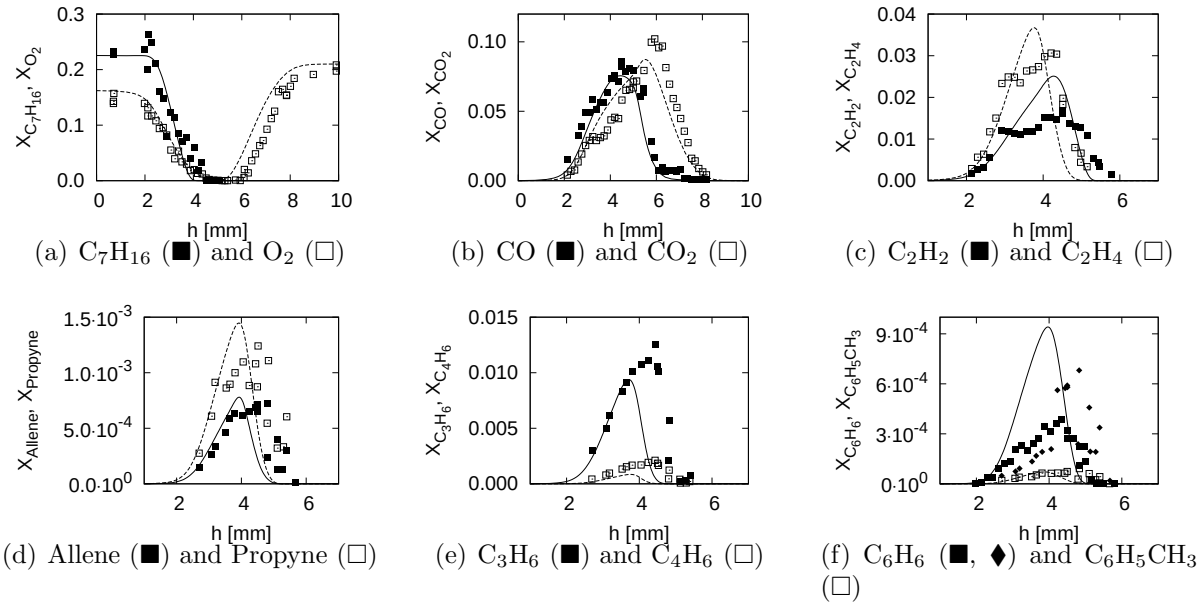

(a) C_7H_{16} (■) and O_2 (□) (b) CO (■) and CO_2 (□) (c) C_2H_2 (■) and C_2H_4 (□)

(d) Allene (■) and Propyne (□) (e) C_3H_6 (■) and C_4H_6 (□) (f) C_6H_6 (■, ♦) and $C_6H_5CH_3$ (□)

Figure 2.20: Mole fractions of main species and soot precursors for the *n*-heptane diffusion flame. Experimental data from Berta et *al.* [14]

On the other hand, for the acetylene diffusion flame, the C_3H_4 isomers are formed from the reaction of methyl radicals with acetylene present in large quantity. In both cases, the propargyl and allyl radicals react with one another to form benzene. Then, toluene molecules are formed by addition of methyl radicals on benzene or phenyl rings.

2.5 Summary

In this chapter, a chemical mechanism has been developed to describe the formation of soot precursors and large Polycyclic Aromatic Hydrocarbons from the combustion of engine relevant fuels. This chemical mechanism is composed of only 151 species and 1658 reactions. However, it remains very detailed and represents the combustion of a large range of fuels from methane to iso-octane with very good accuracy. Furthermore, the formation of soot precursors in laminar premixed and diffusion flames is correctly predicted.

Chapter 3

VSH Multi-Variate Soot Model

In the previous chapter, a chemical model has been derived to describe the combustion of the different fuel components and the formation of larger hydrocarbon molecules. When two large Polycyclic Aromatic Hydrocarbons (PAH) collide with one another, it is assumed that the first soot particle is being born. The mass is transferred from the gas phase into the soot particle. Then, the newly formed soot particle can further grow by collision with other particles or by addition of carbon atoms on its surface through chemical reactions. This chapter details the mechanism for the formation and growth of these soot particles.

In the following section, a multi-variate soot model is formulated. In this model, a soot particle is represented by three variables: its volume, its surface area, and the number of hydrogenated carbon sites on its surface. In order to correctly represent statistically the entire population of soot particles, the Direct Quadrature Method of Moments (DQMOM) is used. In this method, moments of the Number Density Function (NDF) are solved. The source terms for these moments are formulated for each physical and chemical processes affecting soot particles. Finally, comparisons with experimental measurements for a series of laminar premixed and diffusion flames are provided.

3.1 Soot Representation

3.1.1 Multi-Variate Formulation

In the present formulation, soot particles are represented as aggregates of small spherical particles called primary particles [140]. In a flame, it is likely that the primary particles within a given aggregate have been formed at the same time, and hence that they have similar diameter. All primary particles within an aggregate particle are then assumed to be of identical diameter d_p. However, different aggregates can be composed of primary particle with different diameters. A soot aggregate is composed of a certain number of these primary particles n_p. Given the number of primary particles per aggregate (n_p), the total volume (V) and total surface (S) of a soot aggregate can be expressed as

$$V = \frac{\pi}{6} n_p d_p^3, \tag{3.1}$$

$$S = \pi n_p d_p^2. \tag{3.2}$$

Inversely, given the total volume and total surface area of one soot aggregate, one can reconstruct the primary particle diameter and the number of primary particles per aggregate as

$$d_p = 6\frac{V}{S}, \tag{3.3}$$

$$n_p = \frac{1}{36\pi} S^3 V^{-2}. \tag{3.4}$$

The density of soot particles is considered to be constant ($\rho_s = 1800\,\mathrm{kg/m^3}$) and independent of the size and shape of the aggregate. Finally, it is assumed that only carbon atoms contribute to the mass of soot particles, as experimental measurements have reported that the C/H molar ratio is much greater than unity [69, 82]. The following development can be equivantly written in terms of the mass of the soot particle. However, the volume was preferred as experimental measurements usually

report the soot volume fraction.

To better predict the soot volume fraction over a wide range of temperatures and pressures, a third parameter is introduced. This third quantity is the number of hydrogenated carbon sites or active sites on the surface of the soot aggregate, denoted in the following as H. The surface reactivity of a soot particle, defined as the density of active sites per unit surface area, is then written as

$$\chi = \frac{H}{S}. \tag{3.5}$$

In summary, in the present model, a soot particle is here described by three parameters: the total volume (V), the total surface area (S), and the total hydrogen content on the surface (H). This model will be referred to subsequently as Volume-Surface-Hydrogen VSH-model. When a soot model depends upon the volume and surface only, it will be referred to as VS-model, and it is called V-model, when it depends only upon the volume.

3.1.2 Direct Quadrature Method of Moments

To accurately describe the Number Density Function (NDF) of soot, the Direct Quadrature Method of Moments (DQMOM) is used [108]. The method has already been described for a bivariate VS-soot formulation [210, 56], and is here extended to a trivariate formulation. Full details of the method can be found in [108, 210]. Therefore, only a brief description of the method will be presented. Let us consider the Population Balance Equation (PBE):

$$\frac{\partial n}{\partial t} + \frac{\partial \left(u_j n\right)}{\partial x_j} - \frac{\partial}{\partial x_j}\left(\rho D \frac{\partial (n/\rho)}{\partial x_j}\right) + \frac{\partial}{\partial x_j}\left(0.55 \frac{\nu}{T}\frac{\partial T}{\partial x_j} n\right) = \dot{S}\,, \tag{3.6}$$

where $n = n(V, S, H; \mathbf{x}, t)$ is the number density of soot particles that have a given volume V, a given surface S, and a given number of hydrogenated sites H. ρ, T, and ν are the density, temperature, and kinematic viscosity of the surrounding gas, and D is the diffusivity of soot particles. In the free molecular regime, the diffusion coefficient of soot particles is known to depend on the particle diameter as $D \propto d^{-2}$ [60, 164]. This implies that the effective particle Lewis numbers are large, even for very small particles [148]. Therefore, the diffusion term in Eq. 3.6 is neglected. To simplify the notation, the thermophoretic term is combined with the convective term and will not appear later. Details about the numerical methods used to solve these equations are provided below.

The number density varies in space ($\mathbf{x}$) and in time (t). The source term $\dot{S}$ that appears in the PBE is a function of this number density function. One is generally not interested in the full form of the number density function, but only in some of its moments defined as

$$M_{k_1,k_2,k_3}(\mathbf{x}, t) = \iiint V^{k_1} S^{k_2} H^{k_3} n(V, S, H; \mathbf{x}, t) dH dS dV. \tag{3.7}$$

For instance, predicting accurately the total volume ($M_{1,0,0}$), the total surface area ($M_{0,1,0}$), and the total number density ($M_{0,0,0}$) is of primary importance. The DQ-MOM approach can be used to compute a pre-determined set of these moments. DQMOM is a derivative of the QMOM approach (Quadrature Method of Moments). In QMOM, evolution equations for the moments of interest are derived (Eqs. 3.7 and 3.8). The source terms in these equations appear in the form

$$\dot{S}_{k_1,k_2,k_3}(\mathbf{x}, t) = \iiint V^{k_1} S^{k_2} H^{k_3} \dot{S}(V, S, H; \mathbf{x}, t) dH dS dV, \tag{3.8}$$

and are unclosed, since the NDF is unknown. Closure of the source terms is accomplished by a higher order quadrature approximation, which is equivalent to approximating the NDF by a set of delta functions as

$$n(V,S,H;\mathbf{x},t) \approx \sum_{\alpha=1}^{n_d} w_\alpha(\mathbf{x},t)\delta\left(V - V_\alpha(\mathbf{x},t)\right) \times \delta\left(S - S_\alpha(\mathbf{x},t)\right)\delta\left(H - H_\alpha(\mathbf{x},t)\right), \tag{3.9}$$

where n_d is the number of delta functions used for the quadrature. The weights $w_\alpha(\mathbf{x},t)$ and the locations of the delta-functions in the VSH-space $V_\alpha(\mathbf{x},t)$, $S_\alpha(\mathbf{x},t)$, and $H_\alpha(\mathbf{x},t)$, called abscissas, of the delta functions also vary with space and time. Using this expression, the source terms for the moments are approximated by

$$\dot{S}_{k_1,k_2,k_3} \approx \sum_{\alpha=1}^{n_d} V_\alpha^{k_1} S_\alpha^{k_2} H_\alpha^{k_3} \dot{S}(V_\alpha, S_\alpha, H_\alpha) w_\alpha \,. \tag{3.10}$$

With the quadrature approximation, the evolution equations for the moments are closed, leading to the so called Quadrature Method of Moments (QMOM). However, the weights and abscissas appearing in Eq. 3.10 have to be expressed in terms of the moments from Eqs. 3.7 and 3.9 to reconstruct the NDF. This requires $4n_d$ moments and the inversion can be quite complex. The product-difference algorithm [65] can be used for this in the case of a monovariate number density function. Unfortunetaly, in the case of a multivariate number density function, no such algorithm exists, rendering it unusable for the present task.

To avoid this problem, the Direct Quadrature Method of Moments (DQMOM) solves for the weights and abscissas directly rather than for the moments. By replacing the number density appearing in the PBE (Eq. 3.6) with its approximated form given by Eq. 3.9, transport equations for the weights and abscissas are obtained:

$$\frac{\partial w_\alpha}{\partial t} + \frac{\partial}{\partial x_j}\left(u_j w_\alpha\right) = \dot{a}_\alpha \,, \tag{3.11}$$

$$\frac{\partial w_\alpha \xi_\alpha}{\partial t} + \frac{\partial}{\partial x_j}\left(u_j w_\alpha \xi_\alpha\right) = \dot{b}_\alpha \,, \tag{3.12}$$

where ξ_α can be any one of the three abscissas V_α, S_α, or H_α. It can be shown that the source terms $\dot{a}_\alpha$ and $\dot{b}_\alpha$ are solutions of a linear system, whose right-hand side is exactly given by the source terms for the set of $4n_d$ moments [108]. The matrix involved in the linear system only depends upon the abscissas of the n_d delta functions.

In summary, the source terms are first computed for a given set of moments of the number density function ($\dot{S}_{k_1,k_2,k_3}$). Then, a linear system is solved to obtain the source terms for the weights and abscissas ($\dot{a}_\alpha$ and $\dot{b}_\alpha$). The transport equations 3.11 and 3.12 for the weights and abscissas can then be solved. Finally, the moments of the PSDF are reconstructed using Eqs. 3.7 and 3.9.

The matrix involved in the evaluation of the source terms ($\dot{a}_\alpha$ and $\dot{b}_\alpha$) is badly conditioned. As a result, the transport equations for the weights and abscissas are very stiff. To allow an adequate integration of the equations, the partial differential equations (Eq. 3.11 and Eq. 3.12) are replaced by ordinary differential equations were the spatial coordinate is converted into a pseudo time as most of the simulations to be presented are performed for stationary flows ($\frac{\partial}{\partial t} = 0$) in one dimension

$$u\frac{\partial}{\partial x} \rightarrow \frac{\partial}{\partial \tau} \,. \tag{3.13}$$

Finally, the source termns are integrated using a numerical integrator for stiff ODEs (DASSL [146]).

3.1.3 Carbon-to-hydrogen ratio

The C/H ratio is computed from the ratio of the total number of carbon atoms to the total number of hydrogen atoms in the particle. While the first number can

be inferred from the total volume and the soot density, the second number requires additional modeling. This volumetric quantity (denoted H_v) is different from the number of active sites on the surface (denoted H). The effect of the different physical and chemical processes should be considered.

A newly nucleated soot particle has all its hydrogen atoms on the surface ($H_v = H$). Condensation of PAH dimers will increase the total number of hydrogen atoms in the particle as it does on the surface ($dH_v = dH$). Coagulation and surface reactions do not change the total number of hydrogen atoms found in the particle ($dH_v = 0$). Finally, oxidation removes hydrogen atoms from the surface and therefore from the particle ($dH_v = dH$).

3.2 Soot Formation

The source terms which appear in Eqs. 3.10, 3.11, and 3.12 account for different physical and chemical processes: particle inception by PAH dimerization, particle coagulation, growth through surface reaction, and loss of mass by surface oxidation.

3.2.1 Nucleation & Condensation

In the current formulation, a newly formed soot particle is assumed to be a dimer of PAH molecules. Given the large concentration of these dimers, it can be assumed that they either collide with one another or with larger soot particles. The first case will be referred to as nucleation, while the second case will be referred to as condensation (Fig. 3.1). The distinction between PAH dimers and other soot particles is introduced because of the weak binding energy and the small life time of the dimers. Here, we will first describe the formation of the dimers.

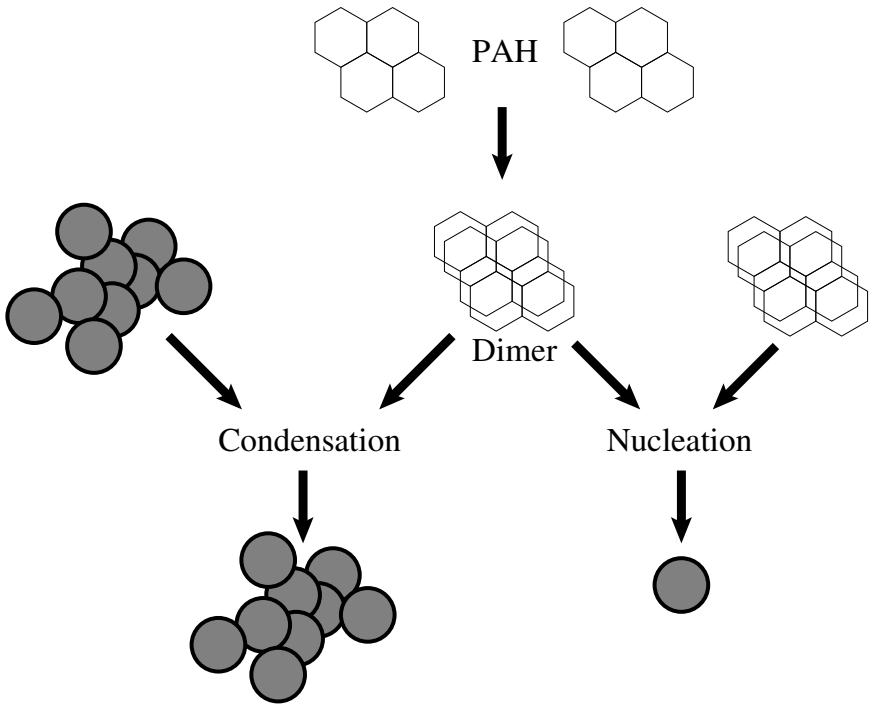

Figure 3.1: Nucleation & condensation of dimers.

Dimerization of PAH molecules

Nucleation of soot particles is usually modeled as the collision and subsequent coalescence of two heavy PAH molecules [161, 201]. For a given type of PAH molecule, the rate of self collisions is given by the kinetic gas theory as

$$\dot{\omega} = \sqrt{\frac{4\pi kT}{m}} d^2 \left[\mathrm{PAH}\right]^2 , \tag{3.14}$$

where d and m are the molecule diameter and mass, and k is the Boltzmann constant. However, the binding energy of dimers formed from the collision of two PAH molecules is very small. For a pyrene dimer, for instance, it is 19.6 kJ/mol [161]. Also, because of the shallow potential well, the dimer lifetime is very small, from about 2 ps for naphthalene dimers to 20 ps for coronene dimers [201]. As a consequence, the effective rate of dimer formation is much smaller than that predicted by kinetic gas theory,

Species name	Formula	m_i	γ_i
naphthalene	$C_{10}H_8$	128	0.0010
acenaphthylene	$C_{12}H_8$	152	0.0030
biphenyl	$C_{12}H_{10}$	154	0.0085
phenathrene	$C_{14}H_{10}$	178	0.0150
acephenanthrylene	$C_{16}H_{10}$	202	0.0250
pyrene	$C_{16}H_{10}$	202	0.0250
fluoranthene	$C_{16}H_{10}$	202	0.0250
cyclo[cd]pyrene	$C_{18}H_{10}$	226	0.0390

Table 3.1: List of species used for dimerization with their mass (in amu) and sticking coefficient.

and a sticking coefficient γ has to be introduced. Both experimental measurements and numerical modeling [40] have shown that the sticking efficiency increases with the size of the collider, and can be very small for nanometer sized spheres ($\gamma \approx 0.001$).

Nucleation is expressed as the self collision of a series of PAH molecules. The species used for nucleation are listed in Table 3.1 together with their mass and sticking coefficient. The diameters of the PAHs were estimated by assuming that PAH molecules are spheres with the density of soot. This assumption is rather crude, as most PAH molecules are planar. However, corrections such as steric factors are reflected in the sticking coefficient. D'Alessio *et al.* [40] showed that for small particles, the sticking coefficient scales with the square of the binding energy, which is estimated to depend upon the square of the mass. As a consequence, the sticking coefficients were assumed to scale with the mass of the PAH molecules to the fourth power

$$\gamma_i = C_N \cdot m_i^4 \,, \tag{3.15}$$

where C_N is a constant that is adjusted to better match experimental concentrations of PAH molecules (cf. Section 4.2). The sticking coefficients for napthalene (A_2) and acenaphthylene (A_2R5) were found too large and were further reduced by a factor of

three. The effective rate of dimerization of PAH molecules is then given by

$$\dot{\omega}_{\text{dimer}} = \sum_i \gamma_i \left(\frac{4\pi kT}{m_i}\right)^{1/2} \left(\frac{6m_i}{\pi\rho_s}\right)^{2/3} [\text{PAH}_i]^2 \tag{3.16}$$

Rather than computing all possible PAH dimers, only the total rate of formation of dimers ($\dot{\omega}_{\text{dimer}}$) and the average carbon (C_{dimer}) and hydrogen (H_{dimer}) content per dimer are evaluated.

Removal of dimers is by nucleation and condensation, which will be discussed next. Both, the source terms for nucleation and condensation depend on the concentration of PAH dimers. Because of the high collision frequency with other dimers or larger soot particles, the dimers are assumed to be in quasi steady state. The dimer concentration can then be calculated as the solution of a quadratic equation given by

$$\dot{\omega}_{\text{dimer}} = \beta_N [\text{DIMER}]^2 + \left(\sum_{i=1}^{n_d} \beta_{C_i} w_i\right) [\text{DIMER}] . \tag{3.17}$$

Nucleation

Although in the model, the nucleation step involves two dimers composed of planar PAH molecules, this can be seen as a crude model for the actual nucleation step, which might involve both planar PAH and more complex aliphatically linked aromatic components [192, 191]. Because of the small size of the PAH molecules and the aliphatic bonds, newly formed particles can undergo internal rearrangements, which leads to the experimentally observed liquid-like character and spherical shape of small particles. For instance, the binding energy of the pyrene-dimer, as the largest species participating in the nucleation process, is only 19.6 kJ/mol. At a temperature of $T = 1600\,\text{K}$, this is comparable to its kinetic energy of $3/2RT = 20.0\,\text{kJ/mol}$, where R is the universal gas constant, which again suggests that internal rearrangements might take place. Therefore it is assumed that particle nucleation always leads to a

spherical particle.

Furthermore, because of the small size of the particle, it is assumed that all hydrogen atoms are located on the surface, and are therefore available for surface reactions. The source term for the moments of the NDF is then given by

$$\dot{S}^{nucl}_{k_1,k_2,k_3} = \frac{1}{2}\beta_N \left[\text{DIMER}\right]^2 V^{k_1} S^{k_2} H^{k_3}\,, \tag{3.18}$$

where β_N is the collision rate between two dimers, and [DIMER] represents their concentration. The volume (V), surface (S), and hydrogen (H) variables of the newly formed soot particle are given by

$$\begin{aligned} V &= 2\, W_C\, C_{\text{dimer}} \rho_s^{-1}, \\ S &= \pi^{1/3} \left(6V\right)^{2/3}, \\ H &= 2\, H_{\text{dimer}}, \end{aligned} \tag{3.19}$$

where W_C is the weight of a carbon atom.

Condensation

When a PAH dimer collides with a large soot particle, the colliding dimer will most likely break appart and the two PAH molecules will deposit on the surface. The volume of the large soot particle participating in the collision will increase, and this aggregate will be rendered more spherical by the condensation of mass onto its surface. The hydrogen atoms from the two PAH molecules will be added to the number of active sites found on the surface of the large soot particle. During the surface absorption, some of the previously active sites might be rendered inactive as they are hidden by the two absorbed PAH molecules. However, this effect was not included in

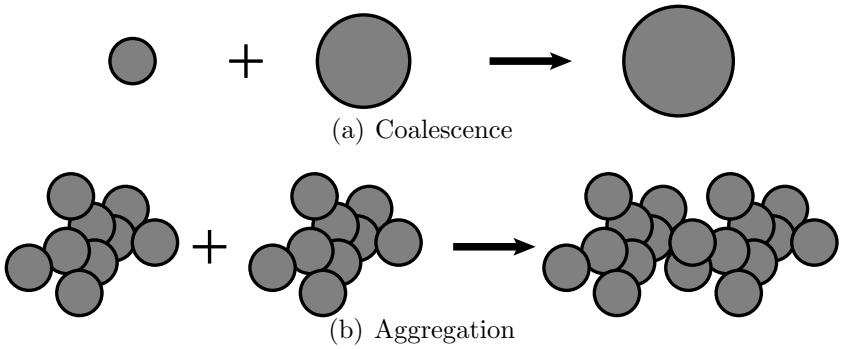

(a) Coalescence

(b) Aggregation

Figure 3.2: Results of two extreme coagulation cases

the model. The source term for the moments of the NDF is then given by

$$\dot{S}^{cond}_{k_1,k_2,k_3} = [\text{DIMER}] \times \sum_{i=1}^{n_d} \beta_{C_i} \left(k_1 \frac{\delta V_i}{V_i} + k_2 \frac{\delta S_i}{S_i} + k_3 \frac{\delta H_i}{H_i} \right) V_i^{k_1} S_i^{k_2} H_i^{k_3} w_i. \tag{3.20}$$

This expression corresponds to a linear (first order) growth as the mass of the PAH molecules is much smaller than that of a soot particle. The small changes in volume and hydrogen of the large soot particle are given by

$$\begin{aligned} \delta V_i &= 2\, W_C\, C_{\text{dimer}} \rho_s^{-1}, \\ \delta H_i &= 2\, H_{\text{dimer}}. \end{aligned} \tag{3.21}$$

The expression for the change in surface area will be given later in Section 3.2.4.

3.2.2 Coagulation

The coagulation process represents the collision of two soot particles. When the particle resulting from the collision of two smaller particles is a sphere, coagulation is here referred to as coalescence (Fig. 3.2(a)). When the resulting particle retains the essential structure of the colliding particles, an aggregate is formed, and coagulation is referred to as aggregation (Fig. 3.2(b)).

The rate of coagulation is a function of the size and shape of the colliding particles. Small primary particles are characterized by a large Knudsen number (Kn $\gg$ 1) defined as the ratio of the collision dimater to the mean free path ($\mathrm{Kn}_i = \lambda/d_{c_i}$). These particles evolve in the free molecular regime. On the other hand, large aggregates, characterized by a small Knudsen number, evolve in the continuum regime (Kn $<$ 1). Kazakov & Frenklach [88] developed expressions for the collision rates for the free molecular ($\beta_{i,j}^{f.m.}$) and for the continuum regimes ($\beta_{i,j}^{cont.}$)

$$\beta_{i,j}^{f.m.} = 2.2\sqrt{\frac{\pi kT}{2m_{ij}}}\left(d_{c_i} + d_{c_j}\right)^2 \ , \tag{3.22}$$

$$\beta_{i,j}^{cont.} = \frac{2kT}{3\mu}\left(\frac{C_i}{d_{m_i}} + \frac{C_j}{d_{m_j}}\right)\left(d_{c_i} + d_{c_j}\right) \ , \tag{3.23}$$

where $m_{ij} = \frac{m_i m_j}{m_i + m_j}$ is the reduced mass, μ the dynamic viscosity of the surrounding gas, d_{c_i}, d_{c_j} are the collision diameters, and d_{m_i}, d_{m_j} are the mobility diameters. The Cunningham slip correction factor takes the form $C_i = 1 + 1.257\mathrm{Kn}_i$ with the Knudsen number expressed as $\mathrm{Kn}_i = \lambda/d_{c_i}$. The collision rate in the transition regime is approximated by the harmonic mean of the asymptotic values [151]

$$\beta_{i,j} = \frac{\beta_{i,j}^{f.m.}\beta_{i,j}^{cont.}}{\beta_{i,j}^{f.m.} + \beta_{i,j}^{cont.}} \ . \tag{3.24}$$

Following the work of Kruis *et al.* [100], the collision and mobility diameters are assumed to be proportional to the radius of gyration, which is defined as

$$R_g = k_f d_p n_p^{1/D_f} \ , \tag{3.25}$$

where k_f is a fractal constant. Here, to evaluate the rate of coagulation, the limit of a single sphere is considered. In this limit, both the collision and the mobility

diameters are equal to the diameter of the sphere

$$d_c \equiv d_m \equiv d_p n_p^{1/D_f}, \tag{3.26}$$

where D_f is the fractal dimension of the soot aggregates, taken to be $D_f = 1.8$. This value corresponds to typical soot aggregates formed in premixed and diffusion flames [98, 82]. The collision and mobility diameters can then be determined from the surface and volume of the particle using Eqs. 3.3, 3.4 and 3.26.

The source terms for the moments of the NDF are given by

$$\dot{S}^{coag}_{k_1,k_2,k_3} = \frac{1}{2}\sum_{i,j=1}^{n_d} \beta_{i,j} w_i w_j \times \left(V_{i+_j}^{k_1} S_{i+j}^{k_2} H_{i+j}^{k_3} - V_i^{k_1} S_i^{k_2} H_i^{k_3} - V_j^{k_1} S_j^{k_2} H_j^{k_3} \right), \tag{3.27}$$

where the volume (V_{i+j}) of the newly formed soot particle is given by

$$V_{i+j} = V_i + V_j \,. \tag{3.28}$$

The reactivity of the newly formed soot particle (H_{i+j}) is assumed to be the same as the averaged reactivity of the two colliding particles [176]

$$H_{i+j} = \frac{H_i + H_j}{S_i + S_j} \times S_{i+j} \,. \tag{3.29}$$

The surface area of the new particle (S_{i+j}) will be expressed later in Section 3.2.4.

3.2.3 Growth by surface reactions

Several chemical reactions could take place on the surface of a soot particle. In the model, the H-abstraction C_2H_2-addition (HACA) mechanism [59] is used. In this mechanism, the addition of mass on the surface of a soot particle proceeds in several steps. Each of these steps is assigned a rate constant in the Arrhenius form

Reactions				A	n	E	ref.
1:	Soot−H + H	↔	Soot* + H_2	1.00×10^8	1.80	68.42	[115]
				8.68×10^4	2.36	25.46	
2:	Soot−H + OH	↔	Soot* + H_2O	6.72×10^1	3.33	6.09	[182]
				6.44×10^{-1}	3.79	27.96	
3:	Soot−H	↔	Soot* + H	1.13×10^{16}	−0.06	476.05	[67]
				4.17×10^{13}	0.15	0.00	
4:	Soot* + C_2H_2	→	Soot−H	2.52×10^9	1.77	13.54	2×[183]

Table 3.2: Rate coefficients for the surface reactions in Arrhenius form ($k = AT^n \exp(-E/RT)$). Units are cm^3, K, mol, s, and kJ.

as shown in Table 3.2. The rate constants hence were taken from similar reactions on benzene and phenyl molecules, which were then rescaled to account for the number of active sites [115, 182, 67, 183]. When available, the high pressure limit of the rate constant was considered. The addition of acetylene on a radical site is assumed to be irreversible, and the rate has been multiplied by two to better match experimental measurements.

After the acetylene addition, several stabilization reactions can occur (Fig. 3.3). These reactions can lead to cyclopentafused aromatics (path 1), ethynyl substituted aromatics (path 2), or ring closure (path 3 and 4). Furthermore, previously stable portions of the surface can be subject to rearrangements to form new 5-membered or 6-membered rings (path 5 and 6) [58].

In the present model, there is no direct distinction between these reaction pathways, since it is impractical to keep track of all possible outcomes. Tracking the different types of active sites requires information about their relative locations to one another and would lead to an excessive model. Instead, only the resulting increase or decrease in the number of hydrogenated sites or active sites on the soot surface is considered.

Because of the possible rearrangements between types of active sites (path 5 and 6), all hydrogenated sites on the surface of a soot particle are considered to be active.

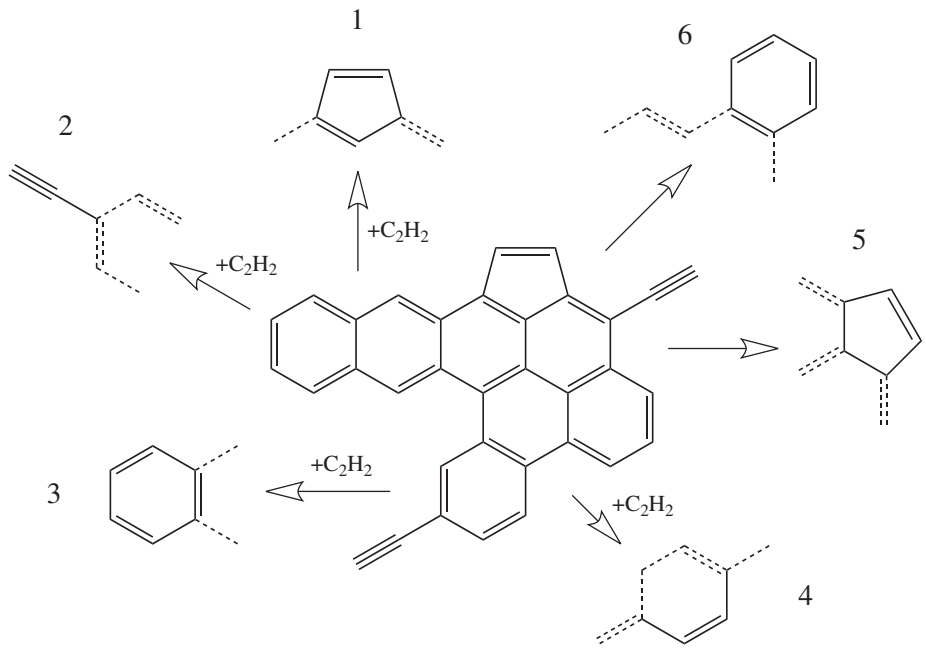

Figure 3.3: Possible stabilization processes resulting from the addition of acetylene C_2H_2 on a radical site.

Most of the possible stabilization reactions will keep the number of hydrogenated sites constant ($\delta H = 0$ for path 1, 2, and 4). Only the ring closure with an ethynyl substituted aromatic site could lead to an increase in the hydrogen content ($\delta H = 2$). Therefore, it is a reasonable assumption to consider that surface reactions do not change the number of active sites on the particle surface, i.e.

$$\delta H_i = 0\,. \tag{3.30}$$

The change in the volume corresponds to the addition of two carbon atoms, hence

$$\delta V_i = 2W_c\rho_s^{-1}. \tag{3.31}$$

To reduce the cost of the simulation, the radical sites on the soot surface are

assumed to be in quasi steady-state

$$[\text{Soot}-\text{C}^*] = \frac{r}{1+r} M_{0,0,1}\,, \tag{3.32}$$

with

$$r = \frac{k_{1f}\,[\text{H}] + k_{2f}\,[\text{OH}] + k_{3f}}{k_{1b}\,[\text{H}_2] + k_{2b}\,[\text{H}_2\text{O}] + k_{3b}\,[\text{H}] + k_4\,[\text{C}_2\text{H}_2]}\,, \tag{3.33}$$

where $M_{0,0,1}$ corresponds to the total concentration of hydrogenated cabon sites per unit volume. The source term for the moments of the NDF is given by

$$\dot{S}^{surf}_{k_1,k_2,k_3} = k_4\,[C_2H_2]\,\frac{r}{1+r} \times \sum_{i=1}^{n_d} \left(k_1 \frac{\delta V_i}{V_i} + k_2 \frac{\delta S_i}{S_i} \right) V_i^{k_1} S_i^{k_2} H_i^{k_3+1} w_i. \tag{3.34}$$

Only the first order terms (linear gowth) is included in the above relation as the mass of an acetylene molecule is small compared to that of a soot particle.

The expression for the change in total surface area (δS_i) requires further analysis and will be discussed in the following section.

3.2.4 Surface area change by addition of mass

Several processes will contribute to an increase in the mass of a soot particle. The addition of mass can be very small, as in the case of dimer absorption onto the surface (a few carbon atoms) and surface reactions (two carbon atoms), or it can vary significantly as in the case of coagulation.

Small mass addition

A small addition of mass on the surface of an aggregate will slowly transform this aggregate into a more spherical particle. The number of primary particles per aggregate will decrease ($\delta\,(n_p) < 0$), while their diameter will increase ($\delta\,(d_p) > 0$). The

rates of change of those two quantitites are linked. The collision diameter is given by the smallest sphere that encloses the aggregate particle. Mass addition will take place on the entire surface of the aggregate and will increase the collision diameter by the same amount that the diameter of the primary particles touching the enclosing sphere is increased. From this follows that

$$\delta\left(d_p\right) = \delta\left(d_c\right). \tag{3.35}$$

Then, from Eq. 3.26 follows

$$\delta\left(d_p\right) = d_c \times \left(\frac{\delta\left(d_p\right)}{d_p} + \frac{1}{D_f}\frac{d\left(n_p\right)}{n_p}\right). \tag{3.36}$$

As a result, the change in the total surface area can be expressed as a function of the volume increase, and is given by

$$\frac{\delta S}{S} = \frac{\delta V}{V}\left[\frac{1 - n_p^{-1/D_f} - \frac{2}{D_f}}{1 - n_p^{-1/D_f} - \frac{3}{D_f}}\right], \tag{3.37}$$

where V, S, and n_p are the volume, surface area, and number of primary particles in the soot aggregate before the addition of mass. The surface area of the new particle is simply $S + \delta S$. In the limit of a pure spherical particle ($n_p = 1$), the expression for a sphere is recovered

$$\frac{\delta S}{S} = \frac{2}{3}\frac{\delta V}{V}. \tag{3.38}$$

Larger mass addition

The mass to be added on an aggregate can be of the same order as the mass of the aggregate itself, as it is the case for the collision between two large aggregates. In this limiting case, the two particles are assumed to be linked by point contact. For

two particles i and j, the surface area of the new aggregate is

$$S_{i+j} = S_i + S_j. \tag{3.39}$$

For an addition of mass of intermediate size, a geometrically weighted average of the two limiting cases is used. This blending function is based on the ratio of the volume of the smaller particle (V_j) to the volume of the larger particle (V_i)

$$\alpha = V_j/V_i < 1, \tag{3.40}$$

and reads

$$S_{i+j} = (S_i + S_j)^{\alpha} \times \left(S_i + \int_0^{V_j} \delta S_i \left(\delta V \right) \right)^{(1-\alpha)}, \tag{3.41}$$

where the expression for δS_i is given by Eq. 3.37. The integration is introduced to account for cases where the volume increase is not infinitesimal ($V_j \approx V_i$). In these cases, the integral is evaluated by performing successive addition of small elementary volumes.

3.2.5 Oxidation

In addition to the reactions previously mentioned in the context of the surface growth mechanism, other heterogeneous reactions can occur on the particle surface. Reactions describing the oxidation of soot by O_2 or OH are very important, since they account for most of the mass loss of soot in flames. The main product formed by oxidation of soot is carbon monoxide CO. The rate of oxidation by O_2 is taken from Kazakov *et al.* [89], where it is proportional to the number of radical sites on the soot surface. The rate of oxidation by OH, which is proportional to the soot surface, is taken from Neoh *et al.* [132]. Those reactions are summarized in Table 3.3. This simple oxidation mechanism was used for the simulations, as the oxidation process was

Reactions				A	n	E	ref.
1:	$Soot^* + O_2$	$\rightarrow$	$Soot-H + 2\ CO$	2.20×10^{12}	0.0	31.38	[89]
2:	$Soot-H + OH$	$\rightarrow$	$Soot-H + CO$	Reaction probability		0.13	[132]

Table 3.3: Rate coefficients for the surface oxidation in Arrhenius form ($k = AT^n \exp(-E/RT)$). Units are cm^3, K, mol, s and kJ.

found to show small impact on the soot predictions for the current set of premixed and diffusion flames.

When these reactions occur, the volume of a soot particle decreases by loss of one (oxidation by OH) or two (oxidation by O_2) carbon atoms. As in the case of surface growth by acetylene addition, the total surface area is changed. In the case of oxidation, it is assumed that the number of primary particles per aggregate remains constant throughout the oxidation process

$$d\left(n_p\right) = 0. \tag{3.42}$$

Following this assumption, the rate of change of the total surface can be expressed with the rate of change of the total volume. Furthermore, the number of active sites on the surface decreases similarly to the decrease of the total surface area. It is simply assumed that the number of hydrogenated sites per unit surface is kept constant, in other words

$$d\left(\chi\right) = 0\,. \tag{3.43}$$

As a consequence, the rate of change of the surface area and number of hydrogenated sites take the form

$$\frac{\delta H}{H} = \frac{\delta S}{S} = \frac{2}{3}\frac{\delta V}{V}. \tag{3.44}$$

The source term for the moments of the NDF is given by

$$\dot{S}^{ox}_{k_1,k_2,k_3} = \frac{1}{3}\delta V\,(3k_1 + 2k_2 + 2k_3) \times \left(2\,\dot{\omega}_{O_2}\frac{M_{k_1-1,k_2,k_3+1}}{M_{0,0,1}} + \dot{\omega}_{OH}\frac{M_{k_1-1,k_2+1,k_3}}{M_{0,1,0}}\right), \tag{3.45}$$

where

$$\delta V = -W_c\rho_s^{-1}. \tag{3.46}$$

Chapter 4

Validation Results

4.1 Flame Configurations

The present soot model is applied to four atmospheric rich premixed flames [185, 202], and one diffusion flame [143]. The parameters for the premixed flames are given in Table 4.1, while Table 4.2 lists the parameters for the diffusion flame. The gas phase chemistry is solved using the FlameMaster code [147]. Details about the FlameMaster code and the different physical configurations can be found in Appendix C.

Large uncertainties in the temperature measurements are reported for the premized flames (about 100 K for the benzene flame [185]). Because of these uncertainties and unknown heat losses at the wall due to conduction, the experimental temperature

Fuel	ϕ	C/O	v_0	T_0	T_{10}	$T_{\max}$	$\Delta T_{\max}$	Ref.
C_2H_4	2.93	0.98	6.93	400	1746	1878	-30	[202]
C_2H_4	2.64	0.88	6.93	400	1832	1929	0	[202]
C_2H_4	2.33	0.78	6.93	400	1871	1986	-120	[202]
C_6H_6	1.80	0.72	4.0	333	1614	1850	0	[185]

Table 4.1: Parameters for the considered premixed flames. T_0 is the temperature at the burner surface, T_{10} the temperature at 10 mm above the burner, and $T_{\max}$ the maximum temperature (in K). v_0 is the cold gas velocity (in cm/s).

Stream	T	v_0	Y_{N_2}	Y_{O_2}	$Y_{C_2H_2}$
Fuel	400	4.176	0.5096	0	0.4904
Oxidizer	400	8.403	0.7794	0.1836	0.0370

Table 4.2: Mass fractions, temperatures (in K), and cold gas velocities (in cm/s) for the diffusion flame [143].

profiles were imposed after some corrections. Two of the ethylene flames ($C/O = 0.98$ and $C/O = 0.78$) exhibit atypical temperature profiles with a large maximum in the temperature, followed by a sudden drop and then a linear decay. This linear decay is mainly due to radiation heat losses by the gas phase. However, the large measured maximum temperature results from catalytic effect of non-ceramic-coated thermocouples [172]. As a consequence, the maximum temperatures of these two ethylene flames were reduced, and the new values are listed in Table 4.1 together with the corresponding temperature reduction ($\Delta T_{\max}$). The downstrem decay of the temperature was not affected and a piecewise cubic Hermite interpolation was used between the experimental points. The experimental temperature of the benzene flame was imposed without any changes.

For the diffusion flame, the temperature profile was not imposed, and an enthalpy equation was solved. However, due to uncertainties in the exact composition of the oxidizer stream, the dilution by nitrogen was reduced to better match the experimental profiles of CO and CO_2. The mass fractions of oxygen and ethylene were increased by about 20%, while keeping the same equivalence ratio of $\phi = 0.62$. The composition of the two streams used in the simulations are listed in Table 4.2.

DQMOM is implemented as part of the FlameMaster code and is fully coupled with the gas phase chemistry. More details about the FlameMaster code can be found in Appendix C. During these simulations, the total mass of carbon atoms is conserved, since the mass transferred to the soot particles due to PAH dimerization

or surface growth is removed from the gas phase. The simulations have been performed with a quadrature approximation of order three by representing the number density function with two delta functions ($n_d = 2$). Using two delta functions was found to yield very good results when compared to Monte-Carlo simulations while being of comparable cost to other methods typically used in modeling soot formation [127]. Therefore, eight moments of the number density function are required (c.f. Section 3.1.2). This set of moments should include the quantities of primary importance such as $M_{0,0,0}$ (number density), $M_{1,0,0}$ (total volume), $M_{0,1,0}$ (total surface), and $M_{0,0,1}$ (total hydrogen content on the surface). The four other moments were chosen based on dimensional analysis, and are $M_{1/3,0,0}$, $M_{2/3,0,0}$, $M_{0,1/2,0}$, and $M_{0,0,1/2}$. In the pure coalescence limit, $M_{1/3,0,0}$ and $M_{0,1/2,0}$ represent the diameter, while $M_{2/3,0,0}$ is equivalent to $M_{0,1,0}$. In the case of a constant surface reactivity ($\chi = \text{const}$), the last moment $M_{0,0,1/2}$ is proportional to $M_{0,1/2,0}$. This set of eight moments was found to produce accurate results [127] with a good matrix condition number [56] for the inversion of the source terms (Eqs. 3.11 and 3.12).

4.2 Premixed benzene flame

Figure 4.1 gives a comparison of the predicted mole fractions of the main species as well as some of the PAH molecules for the premized benzene flame. The agreement for CO, CO_2, CH_4, and C_2H_2 is very good given the level of uncertainty of the temperature profile (about 100 K [185]).

This flame was used as a target for obtaining the sticking coefficient for the PAH dimerization model. The constant in the sticking coefficient model was chosen to reproduce correctly the concentration of the $C_{16}H_{10}$ species like pyrene (A_4), acenaphthylene (A_3R5) and fluoranthene (FLTN). However, by following this procedure, the sticking coefficients for napthalene (A_2) and acenaphthylene (A_2R5) were found too

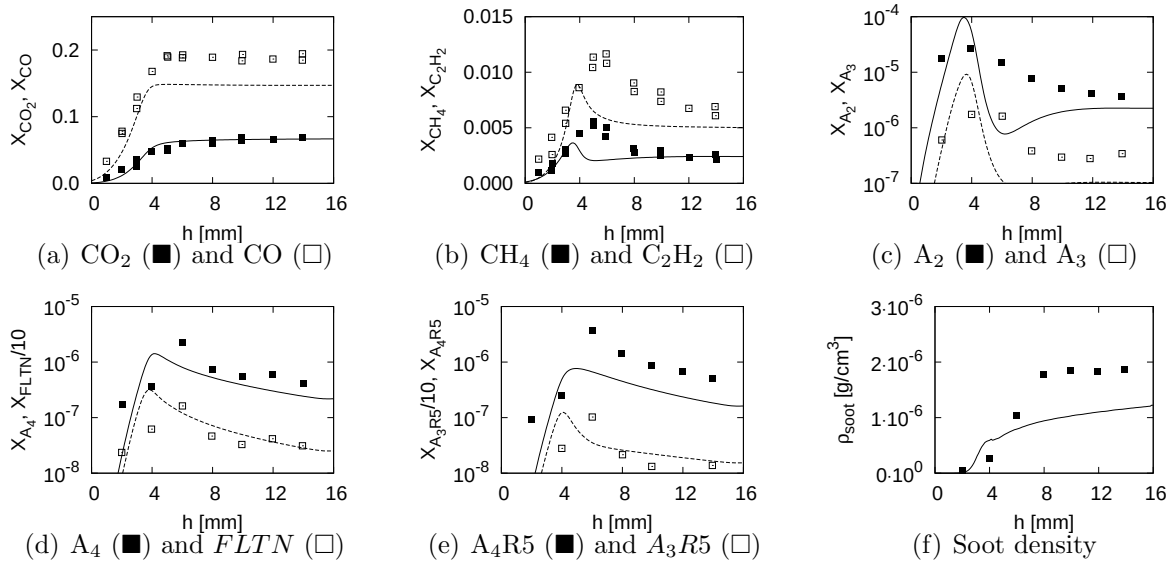

(a) CO_2 (■) and CO (□) (b) CH_4 (■) and C_2H_2 (□) (c) A_2 (■) and A_3 (□)

(d) A_4 (■) and $FLTN$ (□) (e) A_4R5 (■) and A_3R5 (□) (f) Soot density

Figure 4.1: Mole fractions of some species and soot density (in soot mass per unit volume of gas phase) for the benzene flame [185]. First line refers to the first shown species, dashed line to the second.

large and were further reduced by a factor of three. As expected, the mole fractions of the target PAH molecules (Fig. 4.1(d)) are reproduced very accurately, while the mole fractions of the other PAH molecules are predicted with reasonable accuracy (Fig. 4.1(c) and 4.1(e)).

Finally, the soot density profile is compared with the experimental measurements in Fig. 4.1(f). Both the shape and the maximum of the profile are predicted with reasonable accuracy.

4.3 Acetylene diffusion flame

4.3.1 Base case

Figure 4.2 presents the comparison of the simulation of the diffusion flame of acetylene with experimental results. As was already mentioned, the temperature profile was not

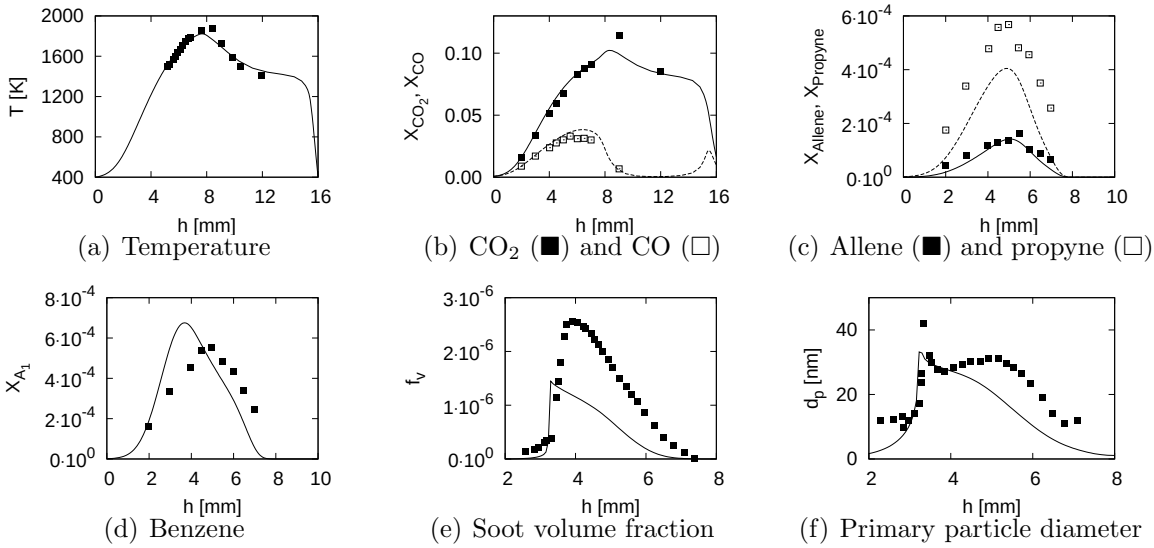

(a) Temperature (b) CO_2 (■) and CO (□) (c) Allene (■) and propyne (□)

(d) Benzene (e) Soot volume fraction (f) Primary particle diameter

Figure 4.2: Mole fractions of some species, soot volume fraction, and primary particle diameter (d_{63} from Eq. 4.1) for the acetylene flame [143, 142].

imposed in this simulation. As a result, a small deviation of approximately 0.5 mm in the location of the maximum occurs, mainly due to buoyancy effects, which were neglected [165]. The profiles of CO and CO_2 (Fig. 4.2(b)) are also correctly predicted, since the composition of the lean premixed flame at $h = 16$ mm has been adjusted. Soot precursors like allene (CH_2CCH_2), propyne (CH_3CCH), and benzene (A_1) are also well predicted by the current chemical mechanism (Fig. 4.2(c) and 4.2(d)).

The soot volume fraction predicted by the current model compares favorably with the experimental measurements (Fig. 4.2(e)). Soot starts to form at a height above the lower burner of $h = 7$ mm, and increases monotonically past the stagnation plane at $h = 3.7$ mm because of thermophoretic effects. The entire profile appears to be shifted towards the fuel nozzle, similarly to the temperature profile because of buoyancy effects.

Finally, Fig. 4.2(f) shows a comparison of the diameter of the primary particles. This diameter has been evaluated experimentally by comparing the average scattering

coefficient (proportional to $n_p d_p^6$ or $M_{4,-3,0}$) to the average extinction coefficient (proportional to $n_p d_p^3$ or $M_{1,0,0}$) [88]. With the current representation of a soot particle (Eqs. 3.1, 3.2, 3.3, and 3.4), the experimental value corresponds to

$$d_{63} = 6 \left(\frac{M_{4,-3,0}}{M_{1,0,0}} \right)^{1/3}. \tag{4.1}$$

Figure 4.2(f) shows the evaluation of the primary particle diameter from Eq. 4.1. Both the scattering and the extinction coefficients depend strongly on the particle diameter. As a consequence, for a bimodal distribution, the d_{63} diameter mainly represents the diameter of the spherical particles composing the large aggregates. In the numerical simulations, two delta functions were used to represent the soot NDF. Throughout this flame, the first delta function remains mostly at the inception zone with a diameter of about $d_{p_1} \approx 1\,\text{nm}$. On the other hand, the second mode ($d_{p_2} \approx d_{63}$) slowly increases and then reaches a plateau, as measured experimentally. Furthermore, close to the stagnation plane, because of the long residence time, the soot particles suddenly grow by addition of mass on the surface through coalescence of smaller particles and absorption of PAH dimers.

This flame has been used as a test case for the coagulation model. Because of the low temperature in the sooting region (below 1600 K), the pool of gas phase radicals is not sufficient to enhance the soot growth by surface reaction through the HACA mechanism. As a consequence, most of the mass in soot comes from the nucleation and adsorption of PAH dimers.

The two modes used to describe the soot PSDF in this flame are significantly different. The first mode corresponds to small spherical particles and the second mode to large aggregates. These bimodal PSDFs have also been found in the experimental work of Wang *et al.* [206] in low temperature flames. To validate the formulation of the coagulation model presented in Sections 3.2.2 and 3.2.4, two additional simulations

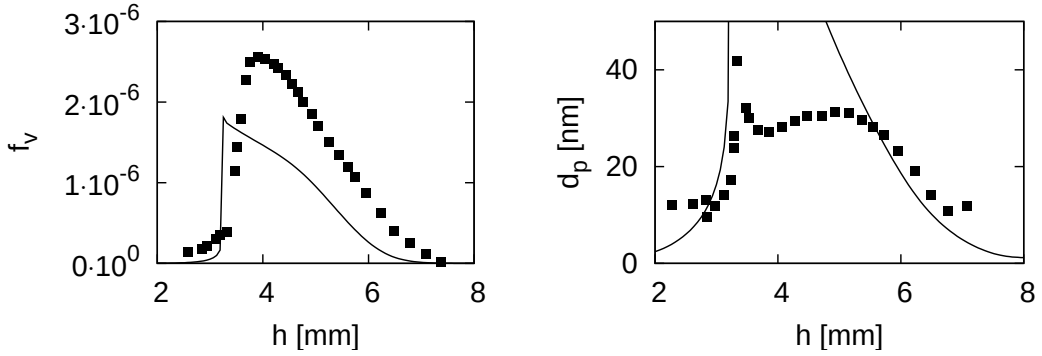

(a) Soot volume fraction (b) Primary particle diameter

Figure 4.3: Soot volume fraction and primary particle diameter (d_{63} from Eq. 4.1) for the acetylene flame [143, 142] in the pure coalescence case.

have been carried out for the case of pure coalescence (all particles are spheres) and pure aggregation (no merging after collision). As for the VSH model, these simulations were performed with two delta functions, thus ensuring that a bimodal distribution can be represented.

4.3.2 Coalescence limit

The first simulation corresponds to the case when coagulation of two soot particles always leads to coalescence (Eq. 3.41 with $\alpha = 0$). This simulation is equivalent to the commonly used model where soot particles are treated as spheres. In this model, soot particles can be described simply by their volume (V-model). Figures 4.3(a) and 4.3(b) show the soot volume fraction and particle diameter for this simulation. As expected, the volume fraction does not differ significantly from the case with the full VSH model, as surface reactions play only a minor role. On the other hand, the particle diameter is largely overpredicted. In the V-model, the diameter of soot particles will keep increasing because of coalescence resulting from particle collisions. If an aggregation model is used, these collisions will form aggregates for collisions of larger particles. The resulting diameters from the V-model will therefore be much

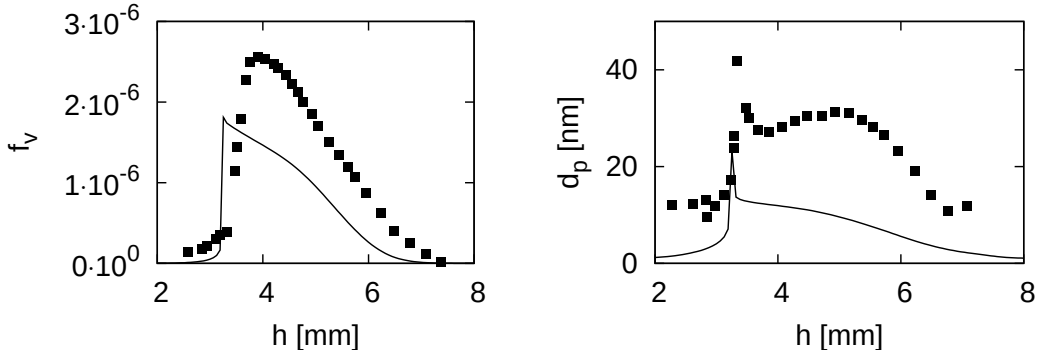

(a) Soot volume fraction (b) Primary particle diameter

Figure 4.4: Soot volume fraction and primary particle diameter (d_{63} from Eq. 4.1) for the acetylene flame [143, 142] in the pure aggregation case.

larger than the primary particle diameter predicted with any aggregation model. In other words, for this particular case, a soot particle cannot be adequately represented by only its volume. The structure of the soot particles has to be considered.

4.3.3 Aggregation limit

The second simulation corresponds to the case when coagulation of soot particles always leads to aggregation (Eq. 3.41 with $\alpha = 1$). This model corresponds to the Monte-Carlo simulations performed by Mitchell & Frenklach [123] or the DQMOM simulations of Fox [56] in the absence of sintering. The predicted volume fraction is slightly greater than for the full coagulation model (Fig. 4.4(a)). However, the particle diameter is underestimated by about a factor of two (Fig. 4.4(b)). In the case of pure aggregation, the diameter of primary soot particles can only increase through surface reactions or adsorption of PAH dimers on the surface. For this flame, the increase of the diameter is mainly due to surface adsorption, as growth by surface reaction is limited. The simulation shows that a large number of the soot particles are very small (around $d_p = 1\,\mathrm{nm}$). One would expect that their collision with larger particles would lead to mostly spherical particles and not aggregates. Thus proving the necessity of

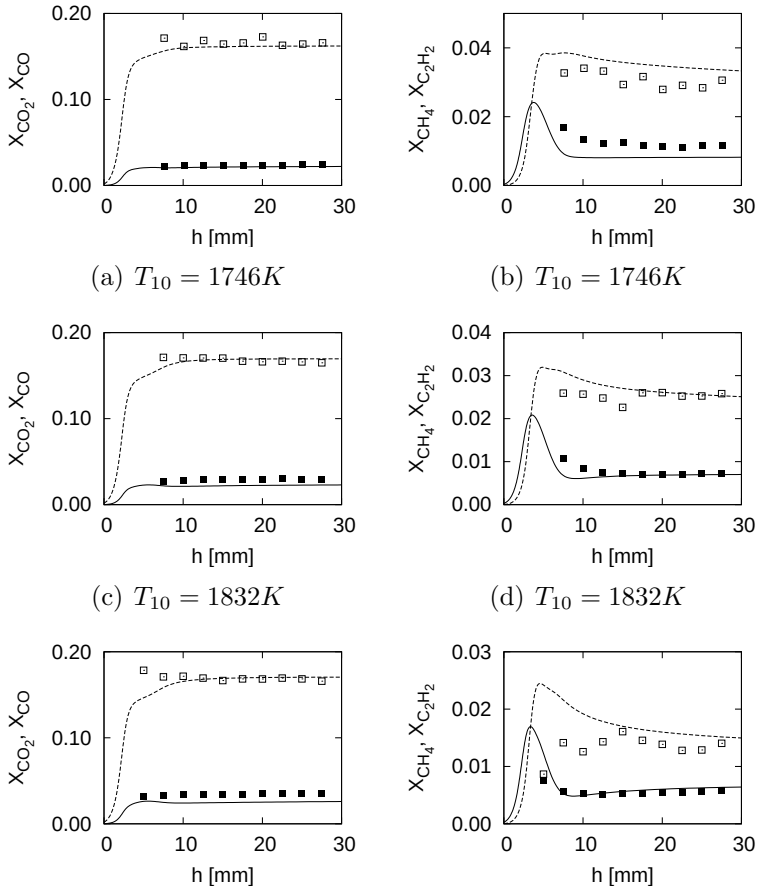

(a) $T_{10} = 1746K$ (b) $T_{10} = 1746K$

(c) $T_{10} = 1832K$ (d) $T_{10} = 1832K$

(e) $T_{10} = 1871K$ (f) $T_{10} = 1871K$

Figure 4.5: Mole fractions of CO_2 (■) and CO (□) (left graphs), and CH_4 (■) and C_2H_2 (□) (right graphs).

considering both limits, coalescence and aggregation, as given by Eq. 3.41.

4.4 Premixed ethylene flames

Figure 4.5 gives a comparison of the predicted mole fractions of the main gas phase species with the experimental measurements. As for the other flames, the main combustion products (CO and CO_2), as well as intermediate species relevant for soot formation (CH_4 and C_2H_2), are correctly predicted by the chemical mechanism.

4.4.1 Soot volume fraction

Figure 4.6 provides a comparison between predicted and measured soot volume fraction. The soot model is able to predict the soot volume fraction for the three flames with good accuracy. Interestingly, the soot volume fraction decreases with increasing temperature. This is an experimentally well known and well characterized phenomenon [17]. At low temperatures, the soot volume fraction increases with increasing temperature. Then, beyond a threshold temperature, the soot volume fraction decreases if the temperature is further increased. This bell-shaped curve has been measured experimentally for several premixed flames by Böhm *et al.* [17]. The value of the threshold temperature was found to be a function of the fuel and other flame parameters. The flames considered here and measured by Xu *et al.* [202] are all in the high temperature region.

4.4.2 Aggregate properties

Figure 4.7 shows a comparison of the predicted diameter of the primary particles with experimental values [202]. The primary particle diameters were measured experimentally through the use of Transmission Electron Microscopy (TEM) pictures. This technique has been shown to disagree with Scanning Mobility Particle Sizer (SMPS) [204]. The soot particles are liquid-like and will spread upon collision on a TEM grid, thus losing their sphericity. Furthermore, only the diameter of the large primary particles found in the larger aggregates can be measured. It might be difficult to gather any information on the diameter of the smallest spherical particles. Therefore, the experimental values should be compared to the diameter of the particles from the second mode of the PSDF.

For most of the time, the first delta function remains at a small diameter around $d_p \approx 1\,\text{nm}$ corresponding to the size of the first soot particles formed by nucleation.

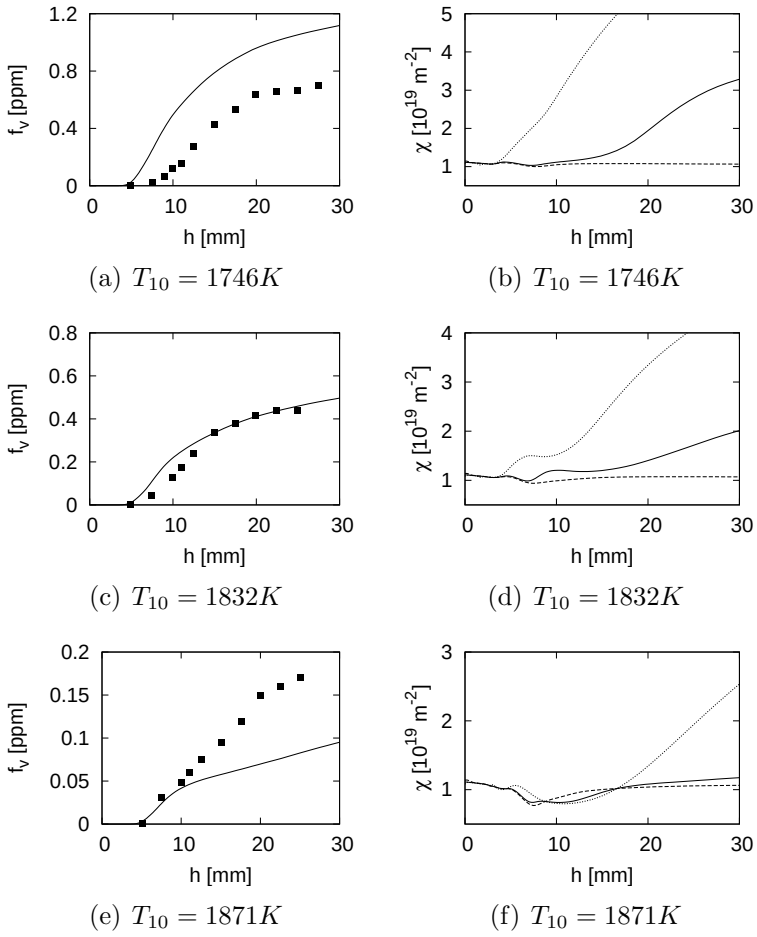

(a) $T_{10} = 1746K$ (b) $T_{10} = 1746K$

(c) $T_{10} = 1832K$ (d) $T_{10} = 1832K$

(e) $T_{10} = 1871K$ (f) $T_{10} = 1871K$

Figure 4.6: Soot volume fraction (left graphs) and surface reactivity (right graphs). Solid line: mean, dashed line: first mode, dotted line: second mode.

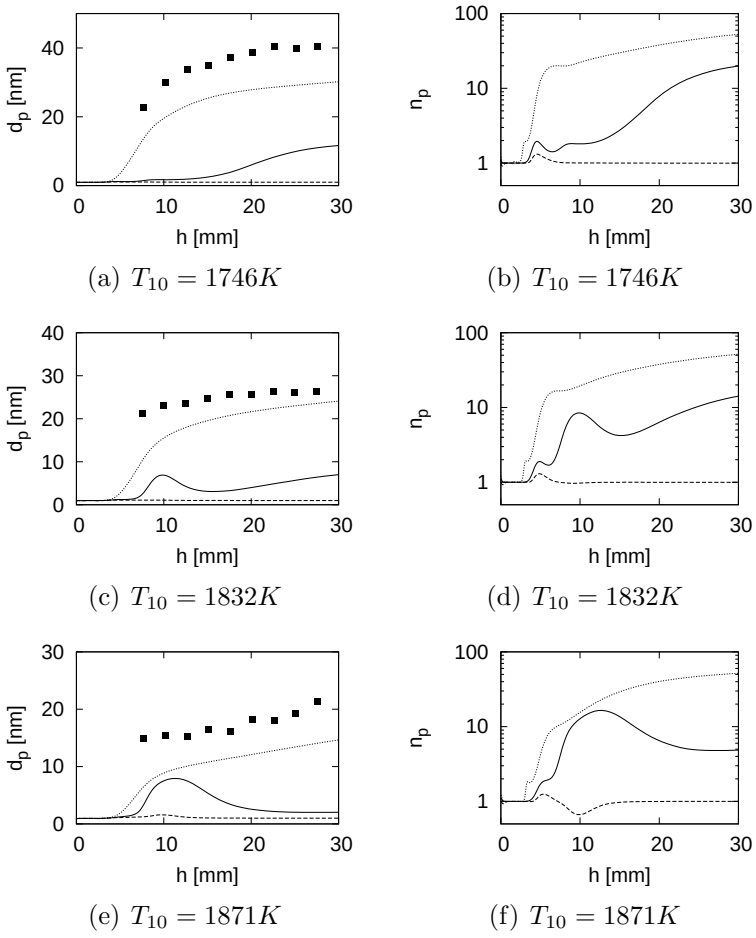

(a) $T_{10} = 1746K$ (b) $T_{10} = 1746K$

(c) $T_{10} = 1832K$ (d) $T_{10} = 1832K$

(e) $T_{10} = 1871K$ (f) $T_{10} = 1871K$

Figure 4.7: Primary particle diameter (left graphs) and number of primary particles per aggregate (right graphs). Solid line: mean, dashed line: first mode, dotted line: second mode.

The second mode reaches rapidly a steady state value around 20 nm. This second mode compares qualitatively well with the experimental values for the three flames studied. Only the flame with the lowest temperature shows some deviation between the computed and measured values. The mean diameter lies between the values of the two modes, but usually closer to the second mode. The reason is that nucleation stops very rapidly in these flames. As a consequence, the magnitude of the first delta function tends to decrease and its weight is transferred to the second delta function.

Finally, Fig. 4.7 also shows the number of primary particles per aggregate (n_p). While there are no experimental values for this quantity, one can estimate from the TEM pictures provided in [202] that this number lies somewhere between 10 to 100. In the current simulations, the number of primary particles per aggregate starts at one, since the first soot particles are assumed to be spherical. Later during the simulation, larger aggregates will form from the collision with smaller soot particles. The computed number of primary particles is for all flames in the expected range.

4.4.3 Discussion

As shown in Fig. 4.6, the decay of the soot volume fraction with increasing temperature is well predicted by the model. The analysis of the results shows that this is because of the decrease in PAH concentration for higher temperatures. This causes, first of all, a lower rate of nucleation and condensation, which decreases the soot volume fraction. Because of this, the surface reactivity, shown in Fig. 4.6, also goes down, which leads to a further decrease in the soot volume fraction.

Figures 4.6(b), 4.6(d), and 4.6(f) show the density of active sites per unit soot surface area for the three flames. The mean value (solid line) varies from about $\chi \approx 1 \times 10^{19}\,\mathrm{m}^{-2}$ to around $\chi \approx 4 \times 10^{19}\,\mathrm{m}^{-2}$. As initially assumed by Kazakov and Frenklach [89], the surface reactivity appears to depend on the temperature. Both the averaged surface reactivity and the surface reactivity corresponding to the second

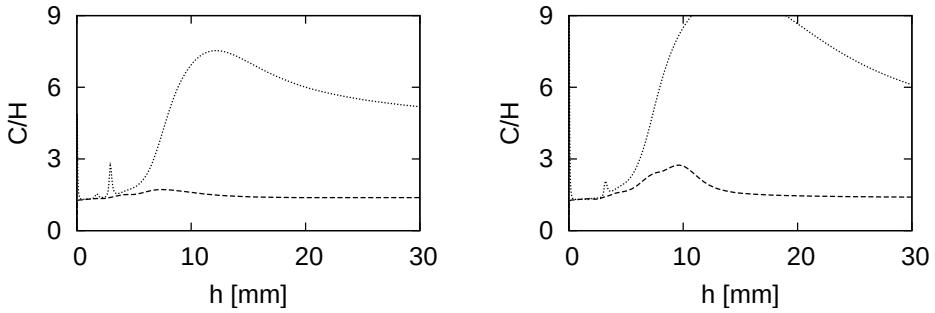

(a) $T_{10} = 1832K$ (b) $T_{10} = 1871K$

Figure 4.8: Carbon to hydrogen (C/H) ratio. Dashed line: first mode, dotted line: second mode.

mode are smaller at higher temperature.

For the flames considered here, the small particles are less reactive than the large particles. However, it is important to note that this is not an assumption in the model. In the present formulation, it is not the size that determines the reactivity, but the history of the soot particles, and the growth mechanisms that have contributed to the particle mass. It is also interesting to note that although the surface reactivity increases, the C/H ratio also increases (Fig. 4.8), as was found in experiments [69]. An increased C/H ratio indicates that the particle is more carbonized.

4.5 Accuracy of Statistical Representation

All the previous simulations were carried out using the Direct Quadrature Method of Moments (DQMOM) with a quadrature approximation of order three (two delta functions). While the different cases studied showed good comparison with experimental measurements, it is interesting to examine the effect the statistical representation might have on the numerical results. Towards this goal, additional simulations are performed for one of the ethylene premixed flames (C/O = 0.88, T_{10} = 1832 K). To fully quantify the accuracy of the statistical representation, simulations with

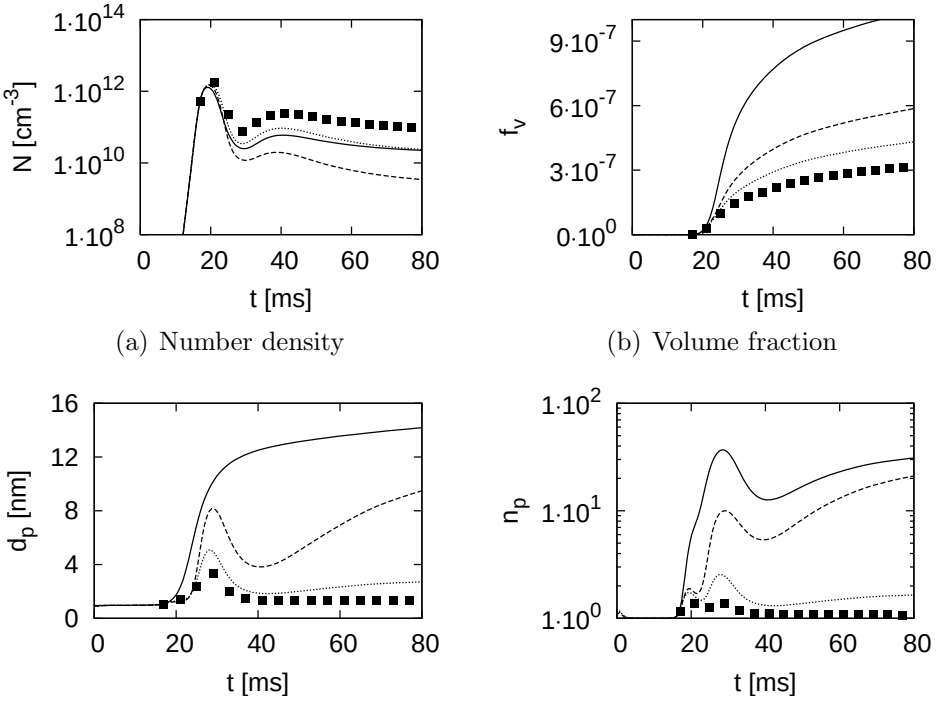

(a) Number density

(b) Volume fraction

(c) Primary particle diameter

(d) Number of primary particles

Figure 4.9: Comparison of predicted mean quantities between DQMOM (one peak (solid), two peaks (dashed), and three peaks (dotted)) and Monte-Carlo simulations (symbols).

DQMOM with different numbers of delta functions (one, two, or three peaks) are compared with Monte-Carlo simulations. More details of the numerical implementation of this method can be found in Ref. [64]. The Monte-Carlo simulation has been performed with 10^5 notional particles using the the same soot model as for DQMOM. However, to allow comparison between the two methods, thermophoretic effects and oxidation reactions were not considered in this section.

Figure 4.9 shows a comparison of predicted mean quantities between DQMOM and Monte-Carlo simulations. For most of the mean quantities, there is a constant improvement going from one peak to two peaks, and from two peaks to three peaks. However, for this particular flame, the results for the number density using just one

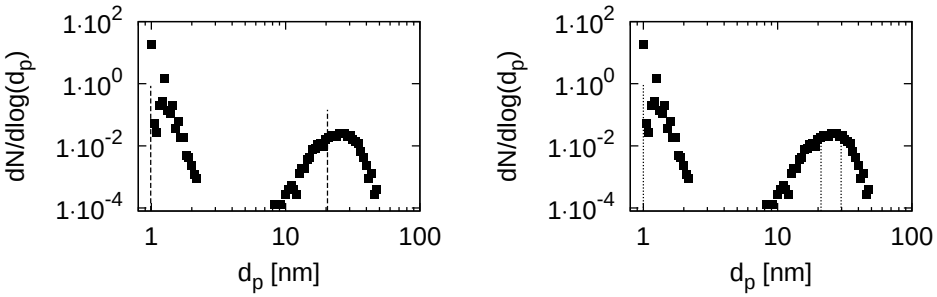

(a) Two peaks (b) Three peaks

Figure 4.10: Location and magnitude of the delta functions in the DQMOM formulation. Symbols are the PSDF evaluated from the Monte-Carlo simulation.

peak are closer to the experiments than those with two peaks.

Figure 4.10 shows the full distribution function of the primary particle diameter predicted with the Monte-Carlo simulation. Apparently, this flame exhibits a significantly bimodal distribution. The first mode corresponds to small spherical particles while the second mode corresponds to large aggregates. In the same figure, the delta functions in the DQMOM formulation are represented. When two peaks are used, the first peak is associated with small particles and the second peak with large particles. The introduction of a third peak does not change the bimodal representation of the PSDF as this third peak is associated also with the second mode. The improvement seen on the volume fraction from the introduction of the third delta function comes from a better description of the variance of the second mode.

In summary, as expected, these simulations show that using more delta functions leads to a better representation of the PSDF. However, this improvement comes at a high cost as the system of transport equations becomes stiffer. Furthermore, the location of the second mode is already well predicted with two delta functions. The improvement between two and three delta functions might not always justify the increased cost. As a consequence, here, the numerical simulations are performed with only two delta funcstions.

Chapter 5

Further Model Analysis

In the previous chapters a chemical model and a soot model have been presented. They describe all combustion processes from the decomposition of the different fuel components to the formation of the first soot particle and its subsequent growth. In this chapter, both models are used to analyze the formation of soot particles in different configurations. In the first case, the effects of temperature on soot formation are studied in a series of homogeneous reactors and laminar premixed flames. Then, the capabilities of the models to predict soot from the combustion of typical fuel components is assessed in laminar premixed flames.

5.1 Analysis of Temperature Effects on Soot

The effects of temperature on soot formation is analyzed in order to explain some of the experimental findings both at low and high temperatures. Towards this goal, the VSH model is applied first in the simulation of a series of high pressure shock tube experiments. Then, numerical simulations of the so-called "bell-shaped" curve are presented for laminar atmospheric premixed flames of ethylene. Finally, soot properties such as the reactivity of the surface and the C/H ratio are evaluated.

5.1.1 Pyrolysis in Shock Tubes

Methodology

In this section, the experimental setup of Hong *et al.* [77] is computed. The shock tube experiments were conducted with a mixture of n-heptane/air/argon under very rich conditions ($\phi = 5.0$) and high pressures ($P_5 \approx 20\,\text{bar}$). During the experiment, the pressure trace was recorded with high accuracy. After the reflected shock, the temperature profile can be evaluated, assuming an isentropically compressed ideal gas. Figures 5.1(a) and 5.1(b) show the time evolution of the temperature and pressure traces for a high temperature run ($T_5 = 1812\,\text{K}$). Both profiles remain constant for about 2 ms until the rarefaction wave arrives. To accurately account for the temperature and pressure effects throughout the simulation, both profiles were prescribed in our shock tube simulations. These simulations have been performed with the FlameMaster code [147] using the detailed chemical mechanism presented in the previous chapters.

Results

A single shock tube simulation ($T_5 = 1812\,\text{K}$) is studied in more detail in order to analyze the effects of temperature and pressure. Figure 5.1(c) shows a comparison of the soot yield predicted by the VSH model and the soot yield obtained from laser extinction measurements [77]. The soot yield is defined as the percentage of initial carbon atoms converted into soot and can be evaluated from the volume fraction using

$$Y = \frac{f_v\,\rho_s\,R\,T}{7\,P\,X_{C_7H_{16}}W_c}\,, \tag{5.1}$$

where R is the gas constant, W_c is the molecular weight of carbon, and $X_{C_7H_{16}}$ is the initial mole fraction of heptane. In these shock tube experiments, the soot yield is preferred over the volume fraction for the dilution effects from changes in temperature

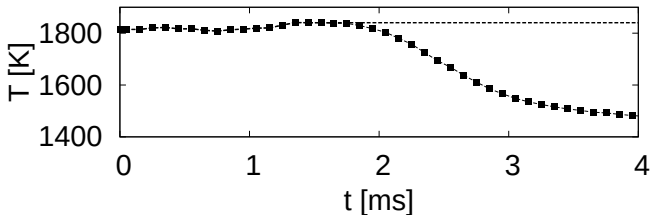

(a) Temperature trace

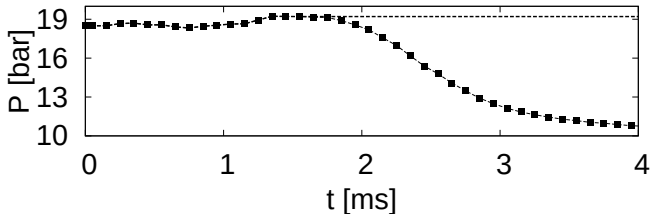

(b) Pressure trace

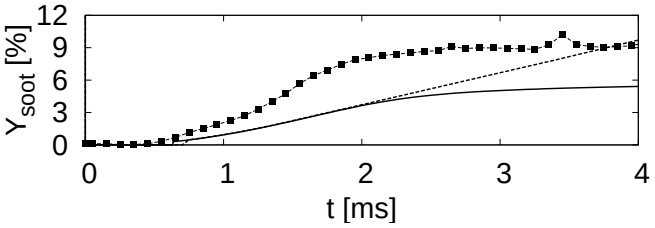

(c) Soot yield

Figure 5.1: Single shock tube experiment perfomed at $P_5 = 20\,\text{bar}$ and $T_5 = 1812\,\text{K}$. Symbols are filtered experiments, solid lines are simulations with full temperature and pressure traces, and dashed lines are simulations with constant temperature and pressure profiles.

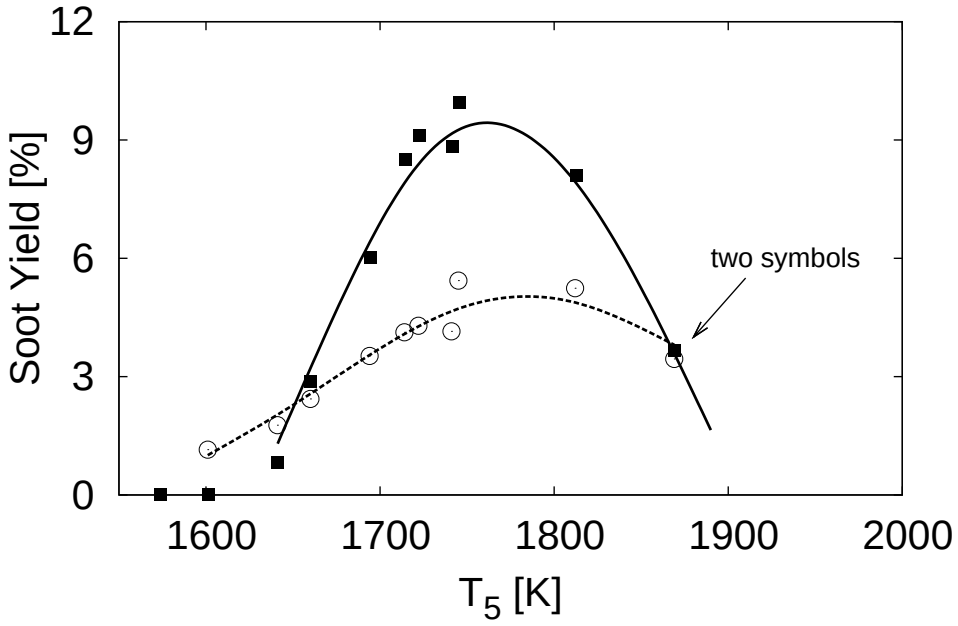

Figure 5.2: Evolution of the soot yield (predicted at $t = 4\,\mathrm{ms}$) with temperature (T_5). Closed symbols: experiments, open symbols: simulations (one simulation per experimentla data point), and lines: fit to the data.

and pressure are removed.

As observed experimentally, the predicted soot yield increases during the first phase of the simulation where both temperature and pressure traces are stable. Then, the temperature gradually drops to 1400 K, and the soot yield remains almost constant. The arrival of the rarefaction wave has severe consequences on the different source terms for the volume fraction. First, the drop in pressure results in a reduction by almost a factor of four in the nucleation and coagulation rates. Second, the drop in temperature virtually eliminates growth by surface reaction by removing the pool of available radicals. To further substantiate these conclusions, an additional numerical simulation has been performed without the effect of the expansion wave. In this simulation, the temperature and pressure profiles were artificially taken to be constant after $t \approx 2\,\text{ms}$. The result of this simulation is compared to the simulation with the full temperature and pressure traces in Fig. 5.1. As expected, the soot yield is not affected until $t \approx 2\,\text{ms}$. Beyond this point, the soot yield from the constant temperature profile keeps increasing while the original soot yield remains nearly constant. This simulation emphasizes the important effects of both temperature and pressure on soot formation.

The soot yield has been measured experimentally for a series of shock tube experiments with different temperatures [77]. Figure 5.2 shows a comparison of the predicted soot yield with the soot yield from the experiments. Each numerical simulation has been performed by using the presure and temperature traces from the experiments. The overall "bell-shaped" curve, and particularly the threshold temperature, is reproduced with reasonably good accuracy. The overprediction of soot yield at low temperature could be explained by an incomplete PAH chemical mechanism. At these temperatures, additional intermediate species and reactions pathways should be considered.

5.1.2 Laminar Premixed Flames

Methodology

Böhm *et al.* [17] studied soot formation in a series of rich atmospheric laminar premixed flames of ethylene ($\phi = 2.16$, C/O = 0.72). In such burner stabilized flames, the maximum temperature is a function only of the heat release from combustion and the heat losses by conduction to the burner and by radiation. In the experimental setup, different flame temperatures were achieved by increasing the mass flow rate of the ethylene/air mixture, thus reducing the heat losses to the burner. The same approach has been used to simulate these flames numerically using the FlameMaster code [147]. However, because of unknown heat losses to the burner, the maximum flame temperature predicted was lower (by more than 100 K) than the experimental values for a given nozzle exit velocity. As a consequence, the temperature profiles were prescribed in the simulations using the following methodology. For a given nozzle exit velocity (v_0), two flames were computed. The first flame was simulated with an increased nozzle exit velocity ($v_0 + 2.0\,\mathrm{cm/s}$) to counter the heat losses to the burner. Then, the temperature profile predicted was extracted and imposed in the simulation of the second flame with the correct nozzle exit velocity (v_0).

Results

First, to validate the methodoly presented previously, the case of one premixed ethylene flame is analyzed in more detail. Figure 5.3 presents the predicted soot volume fraction (f_v) and number density (N) for the case of a flame at an intermediate temperature ($T_{10} = 1627\,\mathrm{K}$). The evolution of the soot volume fraction is reasonably well predicted. However, the predicted volume fraction at long residence times ($f_{v\infty}$) is larger than the experimental value. The number density and particle volume were

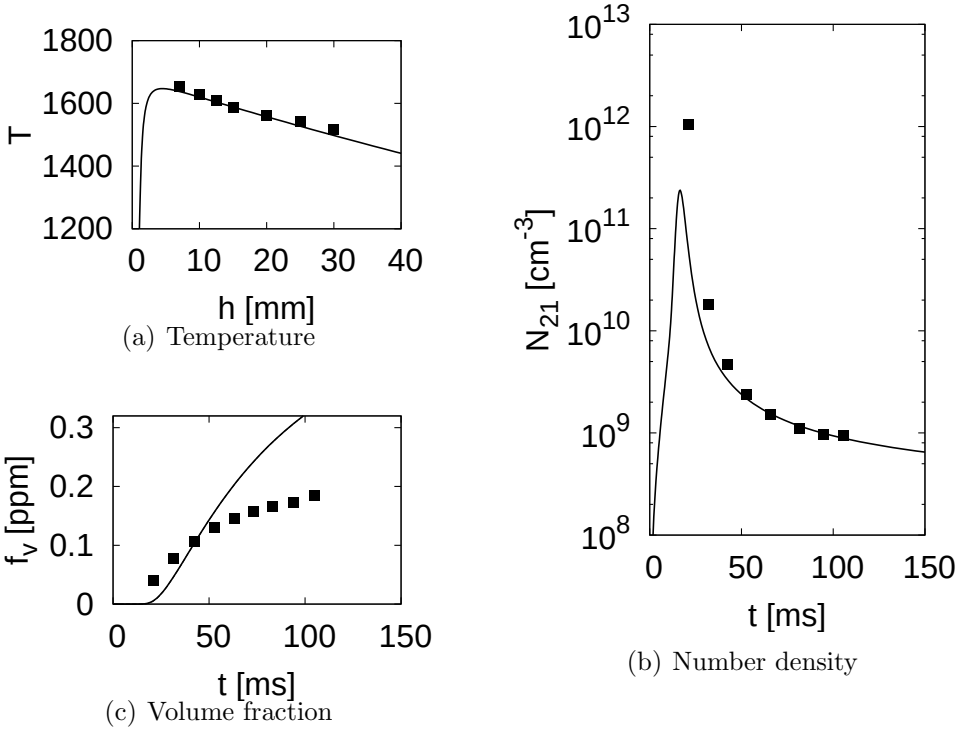

(a) Temperature

(c) Volume fraction

(b) Number density

Figure 5.3: Example of a single premixed ethylene flame ($v_0 = 4.54\,cm/s$, $T_{10} = 1627\,\mathrm{K}$). Symbols are experiments [17, 16], solid lines are predictions.

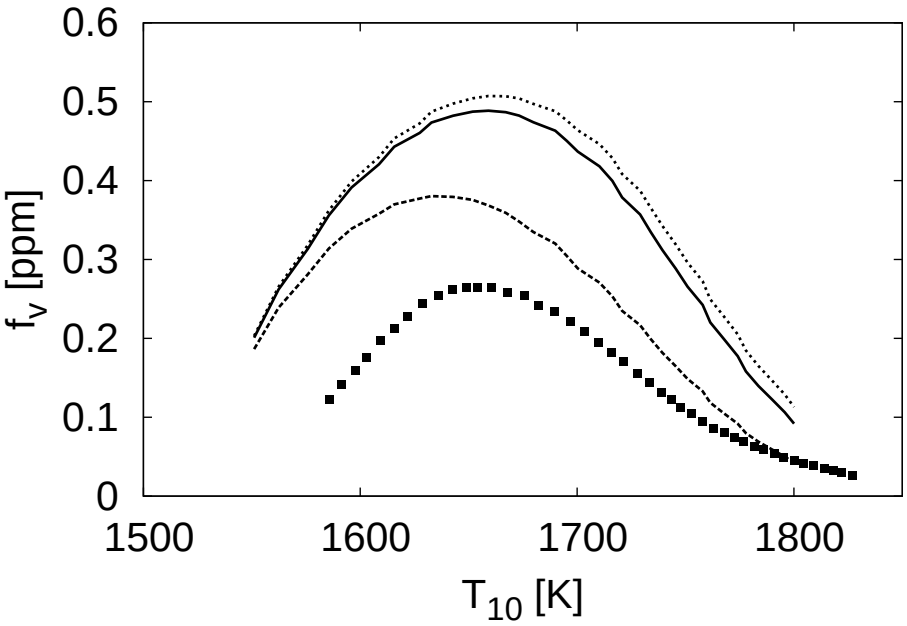

Figure 5.4: Evolution of the soot volume fraction (predicted at $h = 50\,\text{mm}$) with temperature (T_{10}). Symbols: experiments, solid line: full model, dotted line: without oxidation, dashed line: nucleation only

evaluated experimentally from the average scattering coefficients (assumed to be proportional to the square of the particle volume or $M_{2,0,0}$) and the average absorption coefficients (assumed to be proportional to the particle volume or $M_{1,0,0}$) [17]. To accurately compare to the experiment, the number density was evaluated from the numerical simulation as follows

$$N_{21} = \frac{M_{1,0,0}^2}{M_{2,0,0}}. \tag{5.2}$$

While the maximum of the number density is slightly underpredicted, the decay with time is accurately reproduced.

Figure 5.4 shows a comparison of the predicted soot volume fraction at $h = 50\,\text{mm}$ above the burner surface as a function of the flame temperature at $h = 10\,\text{mm}$ (T_{10})

with experimental data [17]. The model predicts reasonably well the so-called "bell-shaped" curve. The location of the peak temperature is correctly estimated, but the overall magnitude of soot volume fraction is too large.

An analysis of the contribution of the different source terms for the first volume moment of the NDF is also provided in Fig. 5.4. Two additional series of simulations have been performed. In the first series, only nucleation source terms were included (dashed line). In the second, all source terms but that for surface oxidation were included (dotted line). In the current model, three processes can affect the soot volume fraction: nucleation/condensation, growth by surface reactions, and loss of mass by oxidation. Nucleation of soot particles occurs mainly at low temperature and reaches a maximum around $T = 1630\,\mathrm{K}$. For low temperature flames (below $T = 1670\,\mathrm{K}$), the mass of a soot particle mainly comes from PAH molecules either through nucleation or condensation. At higher temperatures, surface reactions by way of the HACA mechanism contribute more than 50% of the total mass of a particle. In these rich ethylene flames, oxidation does not play a major role and is active only at high temperatures.

5.1.3 Soot Properties

With the soot volume fraction dependance on temperature predicted with reasonable accuracy, it is interesting to analyze other quantities. The surface reactivity and the carbon-to-hydrogen ratio are of particular interest since they provide insight into the chemical structure of the soot particle.

Surface Reactivity

The soot model used for the present analysis does not assume a given value for the surface reactivity χ. In fact, it directly solves for the surface area and the number of

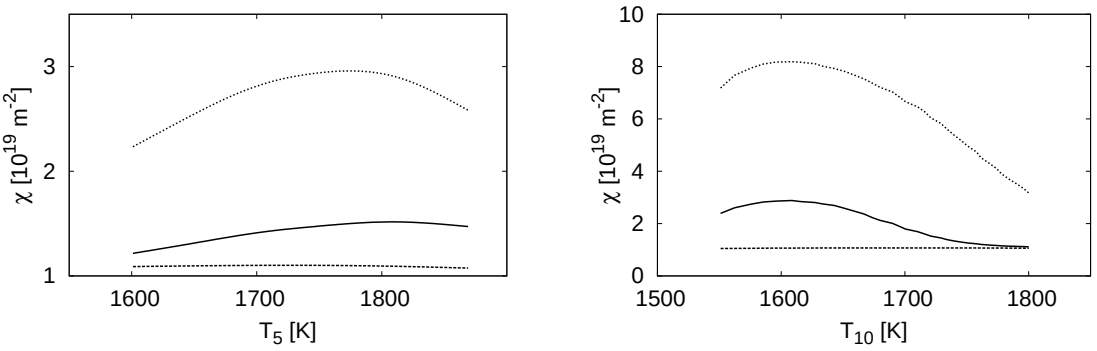

(a) Homogeneous reactors (b) Premixed flames

Figure 5.5: Evolution of the surface reactivity with temperature. Solid: mean value, dashed: first mode corresponding to small particles, dotted: second mode mainly representing large particles.

active sites on the surface. From these two quantities, the surface reactivity can be computed (Eq. 3.5) and plotted as a function of temperature. Figure 5.5 shows the surface reactivity for the two modes (or delta functions) in the DQMOM formulation as well as the mean quantity. The first mode corresponds to small spherical particles, while the second mode corresponds to large soot aggregates.

For both the homogeneous reactors and the premixed flames, the surface reactivity of small spherical particles always remains small around $\chi \approx 1 \cdot 10^{19}\,\mathrm{m}^{-2}$. A newly formed soot particle from the collision of PAH molecules has a small diameter (about $d_p \approx 1\,\mathrm{nm}$) and has only a few hydrogen atoms. As a result, the reactivity of these small particles is very small.

On the other hand, large aggregates are much more reactive. The surface reactivity reaches values around $\chi = 3 \cdot 10^{19}\,\mathrm{m}^{-2}$ at $T = 1800\,\mathrm{K}$ for the homogeneous reactors, and $\chi = 8 \cdot 10^{19}\,\mathrm{m}^{-2}$ at $T = 1600\,\mathrm{K}$ for the premixed flames. Due to their size, large aggregates are more prone to PAH adsorption than small spherical particles. Thus, the surface reactivity is increased by deposition of new active sites on the surface. The values predicted for the surface reactivity of these large aggregates with the current

model are much larger than values typically used in other models [5, 111]. However, it has to be noted that the surface area S corresponds to a macroscopic description of the surface, which would not consider any roughness of the particles and potential aromatic or aliphatic groups sticking out of the surface. This has to be considered in the interpretation of the absolute values of the surface reactivity. It also has to be mentioned that the magnitude of the average surface reactivity is consistent with the values typically specified in other models.

The current model predicts that the surface reactivity increases slightly between 1600 K and 1800 K for the homogeneous reactor. However, over the same temperature range, the surface reactivity decreases significantly more for the premixed flames. While this last result is consistent with the modeling assumption used by Kazakov and Frenklach [89] and later by Appel *et al.* [5], the present work shows that a simple empirical fit for the surface reactivity as a function of temperature may not be adequate for different fuels, and different configurations. Furthermore, the magnitude of the surface reactivity for large particles is significantly different in both cases. Appel *et al.* [5] further assumed that the reactivity of the particles decreases as the particle diameter increases. The current analysis tends to suggest the opposite. In the current model, two processes affect the reactivity of the surface. Through condensation of PAH molecules onto the surface, the particles become larger and more reactive. Surface reactions also lead to an increase in the size of the particle, but reduce the reactivity of the surface per unit surface area. As can be observed in Fig. 5.5, depending on the flame conditions, the balance between these two processes might be different.

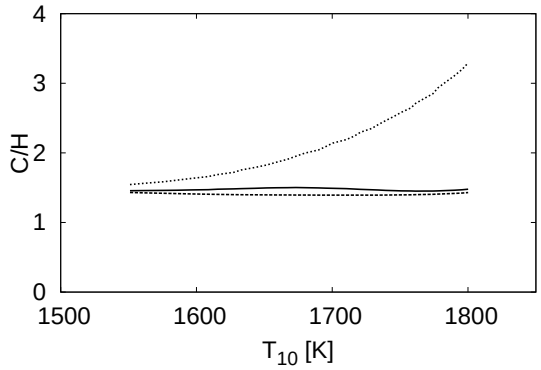

Figure 5.6: Evolution of the C/H ratio with temperature. Solid: mean value; dashed: first mode; dotted: second mode.

Carbon-to-Hydrogen Ratio

As an addition to the VSH model developed previously, the total number of hydrogen atoms in a soot particle (H_v) is also computed. With this quantity, the carbon-to-hydrogen (C/H) ratio can be evaluated and plotted as a function of temperature. Figure 5.6 shows the C/H ratio for the two modes of the DQMOM formulation as well as the mean value. The relative hydrogen content in the small spherical soot particles given by the first mode remains close to that of typical PAH molecules (C/H ≈ 1.5). On the other hand, the large soot aggregates become more carbonized at higher temperatures where the carbon-to-hydrogen ratio can reach values above three. The mean carbon-to-hydrogen ratio remains mostly constant slightly above the value of the first mode.

These results are consistent with experimental measurements for other ethylene premixed flames [69, 204]. Zhao *et al.* [204] measured the intensity of the different carbon based groups in soot particles formed in a low temperature flame (around $T = 1500\,\mathrm{K}$). They found that the C/H ratio was small, ranging from 1.0 to 1.6. While those measurements are confirmed by the simulations, Zhao *et al.* [204] also found aliphatic components in the soot particles which are not considered in the

present model. These aliphatic components would drive the C/H ratio to even lower values. Harris and Weiner [69] measured the carbon-to-hydrogen ratio in flames with higher temperatures (above $T = 1650\,\mathrm{K}$). They found that the particles became more carbonized (larger C/H ratio) with higher residence time in the flame. At higher temperatures, growth by surface reactions is more active. While this process increases the total mass of the particle by adding more carbon atoms, the total hydrogen content remains constant. As a result, the C/H ratio is decreased. Until now, other attempts made at modeling the carbon-to-hydrogen ratio were done in plug flow reactors [200, 27]. In their later models, Celnik *et al.* [27] modeled the detailed chemical structure of the soot surface. Similar to the present results, they found that the C/H ratio increases with time from 1.6 to about 2.0.

5.2 Modeling Soot using Fuel Surrogates of Realistic Fuels

A fuel surrogate is composed of several chemical components. In order to derive a surrogate with the same sooting tendency than that of real fuels, it is important to assess the formation of soot particle from the combustion of the different fuel components separately.

The ability of the chemical mechanism and the soot model to predict the formation of soot particles from the combustion of single component fuels is assessed through the simulation of a series of rich laminar premixed flames. For each component, at least two premixed flames have been considered with different equivalence ratios to evaluate the effect of equivalence ratio on soot yield. The numerical simulations have been performed with the FlameMaster code [147]. When available, the experimental data points are plotted with their respective uncertainties.

Fuel	Pressure	ϕ	v_0 [cm/s]	T_0 [K]	$T_{\max}$ [K]
benzene	1.0	1.80	4.0	333	1821
benzene	1.0	1.80	4.0	333	1821
toluene	1.0	1.88	2.15	370	1497
toluene	1.5	1.91	1.98	390	1550
toluene	3.0	1.75	1.18	370	1659
n-heptane	1.0	2.08	4.76	450	1800
n-heptane	1.0	2.18	4.77	450	1800
iso-octane	1.0	2.08	3.94	450	1850
iso-octane	1.0	2.18	3.95	450	1850

Table 5.1: Parameters used in the simulations of the laminar premixed flames of single component fuels.

5.2.1 Benzene

The formation of PAH species and soot particles in rich premixed flames of benzene has been investigated experimentally by Tregrossi et *al.* [185]. They studied two flames at atmospheric pressure with different equivalence ratios $\phi = 1.8$ and $\phi = 1.93$, corresponding to a carbon-to-oxygen ratio of C/O = 0.72 and C/O = 0.77. These rich premixed flames are stabilized above the burner surface because of heat losses to the burner due to conduction. Because of unknown heat losses to the burner, the temperature profiles were imposed in the current numerical simulations. The temperature profiles measured with thermocouples and reported by Tregrossi et *al.* [185] have been used. The parameters relevant for the benzene flames are listed in Table 5.1.

Both flames have been simulated numerically with the current soot model. Figures 5.7 and 5.8 show the mole fraction of certain soot precursors like acetylene (C_2H_2), propyne (CH_3CCH), and naphthalene ($C_{10}H_8$), and the soot density. The concentration of most of the soot precursors compare resonably well with the experimental data. A small shift could be observed between the predicted and the measured concentration of acetylene and propyne. To account for probe insertion effects, the temperature profiles were shifted by 2 mm [185]. This arbitrary shift together with

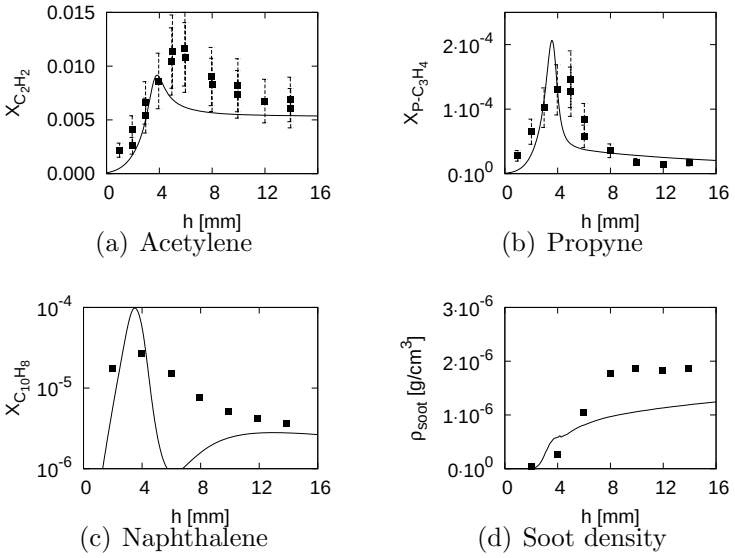

(a) Acetylene (b) Propyne

(c) Naphthalene (d) Soot density

Figure 5.7: Mole fractions of soot precursors and soot volume fraction for the benzene premixed flame ($\phi = 1.80$).

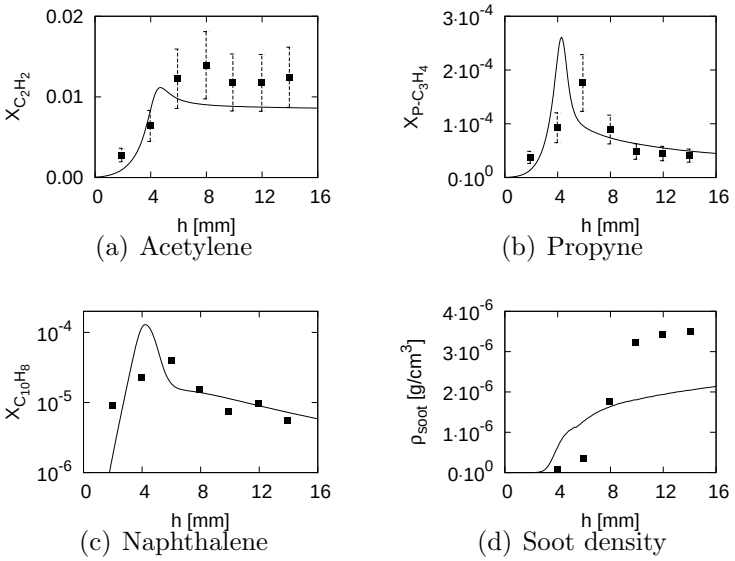

(a) Acetylene (b) Propyne

(c) Naphthalene (d) Soot density

Figure 5.8: Mole fractions of soot precursors and soot volume fraction for the benzene premixed flame ($\phi = 1.93$).

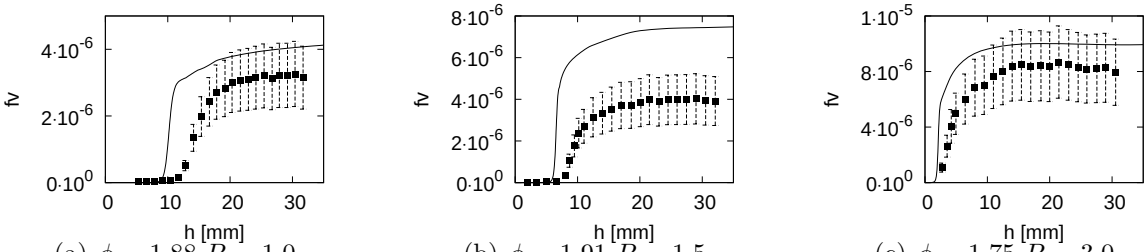

(a) $\phi = 1.88$ $P = 1.0$ (b) $\phi = 1.91$ $P = 1.5$ (c) $\phi = 1.75$ $P = 3.0$

Figure 5.9: Soot volume fraction for the toluene premixed flames.

the large uncertainty on the temperature measurements (up to 100 K) are most likely the source of these errors. For the leaner flame ($\phi = 1.8$), the naphthalene profile shows some discrepancies. These errors could be linked to an incomplete oxidation mechanism for bicyclic aromatics like naphthalene and indene. Further improvement of the aromatic chemistry is required.

The overall evolution of the soot density, defined as the total mass of soot particles per unit volume, is correctly captured with the current model. A small increase in the equivalence ratio leads to a significant increase in the soot yield.

5.2.2 Toluene

Tsurikov et *al.* [186, 63] have studied the formation of soot from the combustion of toluene under atmospheric and elevated pressures (1 bar $< P <$ 5 bar). They considered three flames whose conditions are listed in Table 5.1. The temperature profiles were measured with high accuracy using shifted vibrational coherent anti-Stokes Raman scattering (SV-CARS) technique. Soot volume fraction was measured with Laser induced incandescence (LII). The uncertainties on the temperature measurements were reported to be only ±3% while there were estimated around ±30% for soot volume fraction. As in the case of the benzene flames, the temperature profiles measured experimentally were imposed during the simulation of the three flames.

Figure 5.9 shows a comparison of the predicted soot volume fractions from the current model with the experimental measurements. In should be noted that the predictions are consistently larger than the measurements. Furthermore, the onset of soot formation occurs earlier in the three flames under considerations. However, given the level of uncertainty on the soot measurements the soot volume fractions given by the current model agree favourably with the experimental values. In addition, the effects of pressure and equivalence ratio on the yield of soot is accurately reproduced. When either the equivalence ratio or the pressure is increased, the soot volume fraction is increased.

The results were found to be very sensitive to the rate constant of the propargyl addition on benzyl radical described by the global equation

$$C_7H_7 + C_3H_3 \rightarrow C_{10}H_8 + H_2 \tag{5.3}$$

The rate constant was taken to be the same as that of propargyl recombination [117]. However, at low temperature the yield of dihydro-naphthalene ($C_{10}H_{10}$) is expected to be significant. Thus, the rate constant for the formation of naphthalene should be reduced. A better evaluation of the rate constant is necessary.

5.2.3 n-Heptane

El Bakali et *al.* [7, 193] analyzed the formation of soot particles in premixed *n*-heptane and *iso*-octane flames. They considered a series of rich atmospheric flames with different equivalence ratios from $\phi = 1.90$ to $\phi = 2.24$. The concentration of the main soot precursors like acetylene, allene (CH_2CCH_2), and benzene were measured by gas chromatography. Laser extinction measurements were used to measure the soot volume fractions. In the current work, only two flames were simulated numerically, a moderate rich flame ($\phi = 2.08$) and a very rich flame ($\phi = 2.18$). No temperature

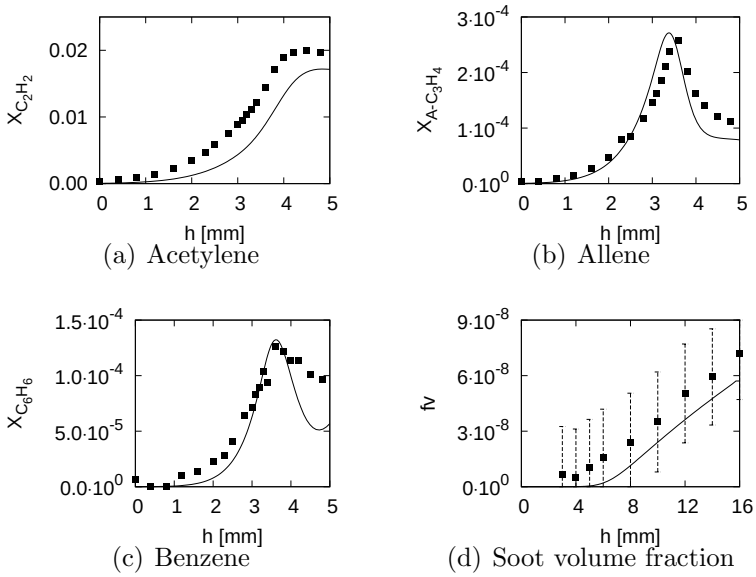

(a) Acetylene (b) Allene

(c) Benzene (d) Soot volume fraction

Figure 5.10: Mole fractions of soot precursors and soot volume fraction for the *n*-heptane premixed flame ($\phi = 2.08$).

measurements have been reported for these flames. As a consequence, the temperature profiles were adjusted to match the location and magnitude of the peaks of allene and benzene. The parameters used for these two flames are summarized in Table 5.1.

Figure 5.10 and 5.11 show a comparison of the concentration of the soot precursors and soot volume fraction with experimental measurements. Most of the soot precursors are accurately predicted over the entire flame. The concentration of benzene molecules is slightly overestimated in the post flame region. However, the comparison remains very good. The evolution of the soot volume fraction profile compares also favourably with experiments. The numerical simulations reproduce an increase in the soot yield similar to that observed experimentally as the equivalence ratio is increased from $\phi = 2.08$ to $\phi = 2.18$.

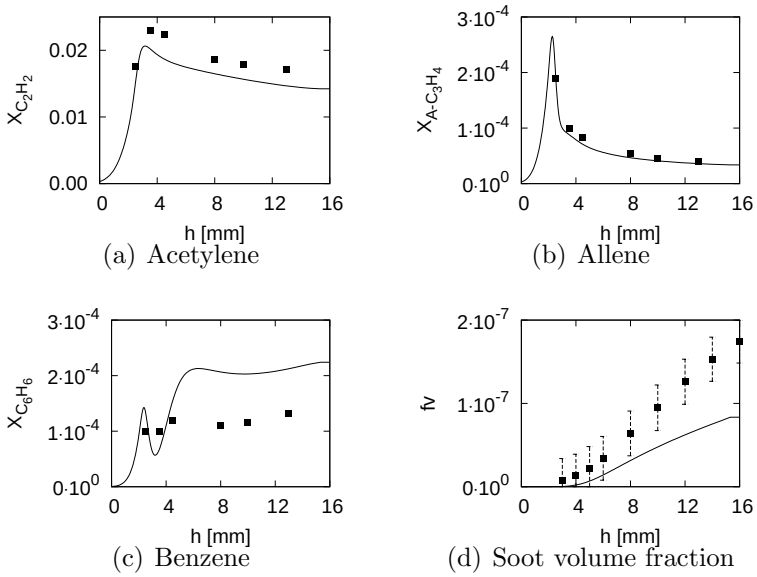

(a) Acetylene (b) Allene

(c) Benzene (d) Soot volume fraction

Figure 5.11: Mole fractions of soot precursors and soot volume fraction for the *n*-heptane premixed flame ($\phi = 2.18$).

5.2.4 iso-Octane

Two *iso*-octane flames were considered for the current work. The experimental data were taken from the same compilation previously used for *n*-heptane flames [7, 193]. As for the *n*-heptane flames, the temperature profiles were adjusted to match the location and magnitude of the peaks of allene and benzene. The parameters used for the numerical simulations are listed in Table 5.1.

The concentration of the soot precursors and the soot volume fraction are compared with experimental measurements in Fig. 5.12 and 5.13. Once again, the concentrations of the soot precursors are correctly estimated. A small underprediction of the maximum of allene in the $\phi = 2.08$ flame is to be noted. The soot volume fraction computed with the current model agrees very well with the experimental data, and the effect of the equivalence ratio on soot yield is correctly captured.

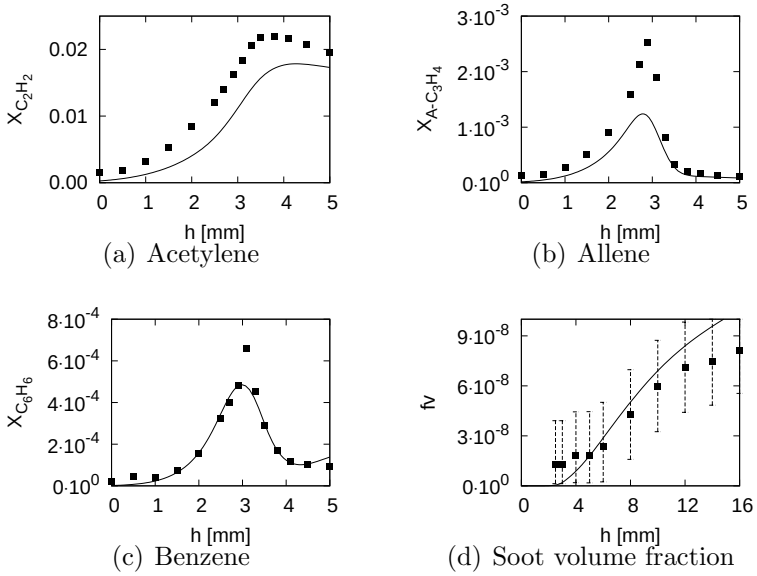

(a) Acetylene (b) Allene

(c) Benzene (d) Soot volume fraction

Figure 5.12: Mole fractions of soot precursors and soot volume fraction for the *iso*-octane premixed flame ($\phi = 2.08$).

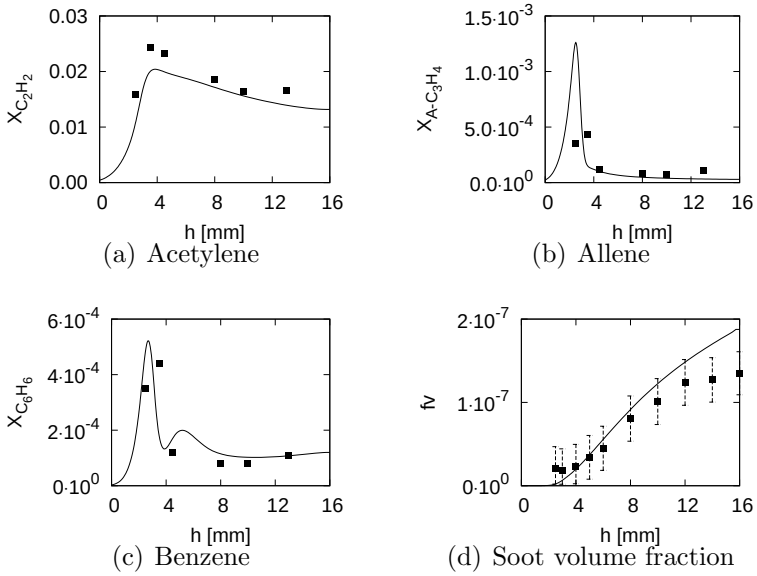

(a) Acetylene (b) Allene

(c) Benzene (d) Soot volume fraction

Figure 5.13: Mole fractions of soot precursors and soot volume fraction for the *iso*-octane premixed flame ($\phi = 2.18$).

5.2.5 Summary

The VSH soot model associated with the chemical mechanism developed previously is found to reproduce soot formation quite accurately from the combustion of several surrogate components. A surrogate for the combustion of gasoline, diesel, or kerosene can be formulated based on these four components (benzene, toluene, *n*-heptane, and iso-octane). This surrogate formulation should be compared to experimental measurements when available.

Chapter 6

Conclusions and Directions for Future Work

The formation of soot particles from the combustion of petroleum based fuels (kerosene, gasoline, and diesel) remains a major problem as the consequences on human health are severe. Over the past decades, strict limitations of particulate matter emissions have been enforced on car engines as well as aircraft engines. Designing such engines and other industrial devices in a way to reduce soot formation is still difficult, for the predictive capabilities of available soot models are limited. First, the formation of soot precursors from the combustion of the different constitutive components of a real fuels is not fully understood. Second, the range of applicability of available soot models remains limited. For instance, the description of soot formation in low and high temperature flames is not completely explained.

This work presents a tentative improvement of some of the above-metioned shortcomings. Towards this goal, the formation of soot particles has been addressed from a chemical, statistical, and physical modeling point of view.

As a first step towards building up a chemical model for simulating the formation

of soot particles from the combustion of fuel surrogates, a new database of thermodynamic properties of large aromatic hydrocarbons has been created. The geometric structures of the different species were optimized at different levels of theory using different basis sets. Results indicate that most of these species are planar under normal conditions. However, certain molecules exhibit an internal degree of rotation. A thorough analysis of the torsional potentials of those molecules has been performed. It was shown that treating those degrees of freedom as hindered rotor is necessary and that a sufficiently accurate level of theory is required to capture the energy barrier to rotation. Finally, the recent and expensive G3MP2//B3 method has been used to compute the enthalpies of formation of these species. Group corrections to these enthalpies have been derived from a set of PAH molecules ranging from benzene up to coronene. The final corrected enthalpies show very good agreement with experimental data, whenever data are available.

Equipped with accurate thermodynamic properties for all species involved in the formation of soot precursors, a chemical mechanism has been developed for the high temperature combustion of engine relevant fuels. In this development, a particular emphasis has been placed on the chemistry of soot precursors like acetylene, the C_3H_4 isomers (allene and propyne), propene, butadiene, and benzene. This mechanism has been extended to include the chemistry relevant to aromatic combustion (benzene and toluene) and the combustion of larger alkanes like *n*-heptane and iso-octane. The full mechanism has been validated extensively against ignition delay times and laminar burning velocities over a large range of equivalence ratios and pressures. The comparison with experimental measurements is very good in almost all cases. Then, the mechanism has been used in the simulation of a series of laminar rich premixed and diffusion flames where the profiles of the main species as well as the soot precursors was shown to compare favorably with experimental data. The chemical steps responsible for the formation of benzene and other soot precursors were analyzed

in these flames. It was shown that the reaction pathways leading to the formation of C_3 and C_4 species (and then benzene) can be significantly different in different flames with different fuels.

Then, a new model describing soot particle dynamics has been formulated. In this model, a soot particle is represented as a fractal-shaped aggregate composed of many spherical primary particles. Three coordinates are used to characterize a soot aggregate: the total volume (V), the total surface area (S), and the total number of hydrogenated (or actives) sites on the surface (H). This multivariate model (VSH) is formulated in the framework of Direct Quadrature Method of Moments (DQMOM) with two delta functions. This allows for an adequate description of a bimodal number density function of soot particles. The VSH model has been applied to a series of laminar premixed and diffusion flames. For all flames, the soot volume fraction was predicted with good accuracy. Aggregate properties, such as primary particle diameter and size of the aggregates, were also analyzed. The results were in reasonable agreement with experiments, where measured data were available. It was shown that the VSH-model has an inherent description of aggregation, because of the consideration of surface and volume as independent parameters. The reactivity of the surface, expressed by the density of active sites per unit surface area, is also computed as part of the model, because of the joint description of particle surface and active surface sites. For high flame temperatures, the reactivity is shown to decrease when the temperature of the flame increases. The combined effect of depletion of PAH molecules in the gas phase and stronger rates of surface reactions could partially explain the reduced soot surface reactivity at high temperature. Furthermore, the current model predicts an increasing surface reactivity with particle size and residence time for the three ethylene flames.

Finally, the joint Volume-Surface-Hydrogen (VSH) model for soot formation has been applied in simulations of high pressure homogeneous reactors and atmospheric

laminar premixed flames of ethylene. The effects of temperature on the prediction of soot volume fraction were analyzed in more details. The soot model was found to predict the so-called "bell-shaped" curve qualitatively well. The soot volume fraction increases until a threshold temperature and then decreases as the temperature is further increased. It was found that nucleation and condensation dominate at low temperatures while growth by surface reaction is more active at intermediate to high temperatures. The chemical composition of soot particles has been investigated by considering the surface reactivity and the volumetric carbon-to-hydrogen ratio. As postulated in many soot models, the surface reactivity was shown to decrease with increasing temperature. However, the reactivity of large aggregates was found to be much larger than that of small spherical particles. On the other hand, large aggregates exhibit a larger C/H ratio characteristic of a more carbonized particle resulting from strong surface reactions.

The current chemical and statistical representation of soot particles allows for a better description of soot formation. This model was shown to predict soot yield for a large set of fuel components and over a wide range of flame conditions, including low and high temperature flames. Furthermore, aggregate properties like the primary particle diameter or the size of the aggregate were predicted accurately in these different flames. However, a series of key points need to be improved for the model to be applied in the simulation of a real engine:

- **Method of Moments** The current statistical formulation based on the Direct Quadrature Method of Moments (DQMOM) provides very accurate predictions of the main moments of the number density function like total number density, soot volume fraction or total surface area of the aggregates. However, the method remains costly and numerical difficulties are often encountered in the integration of the sources terms. Because of the large condition number of the matrix involved in the evaluation of the source terms, an integrator for stiff

ODE had to be used (DASSL). This renders the method impractical for the integration of the soot model in Large Eddy Simulations or Direct Numerical Simulations. A new formulation based on the Method of Moments should be derived. This formulation should remain an accurate statictial representation of the PSDF and should be of reasonable cost.

- **Transition to Aggregation** The collision of two soot particles can lead to the formation of a spherical particle or an aggregate. The transition from coalescence to aggregation has been model empirically. While the results reported in this work compare favourably with experimental measurements of the aggregate properties, a more physical approach to this phenomenon should be included.

- **Surrogate Formulation** This work presents one of the first models to be applied in the simulation of soot formation in flames involving four different fuel components typically found in surrogates: *n*-heptane, iso-octane, benzne, and toluene. However, some properties of real fuels like kerosene cannot be represented accurately only with these four components. For instance, the average carbon number is too small. Longer alkane chains like *n*-decane or *n*-dodecane as well as heavier substituted aromatic hydrocarbons like xylene, trimethybenzene, or *n*-propylbenzene should be considered. In the derivation of a chemical model for the combustion of these chemical species, great emphasis should be placed on the formation of soot precursors.

Appendix A

Geometric Structures of PAH

The following figures provide the detailed geometric structures of the Polycyclic Aromatic Hydrocarbons recomputed in Section 2.

species		symmetry group	geometrical representation
name	formula		
Benzene	A_1	D_{6h}	
Phenyl radical	A_1-	C_{2v}	
ethynylbenzene	A_1C_2H	C_{2v}	
2-ethynylphenyl	A_1C_2H-2	C_s	
3-ethynylphenyl	A_1C_2H-3	C_s	
4-ethynylphenyl	A_1C_2H-4	C_{2v}	
Styrene	$A_1C_2H_3$	C_s	
1-phenylvinyl	$i-A_1C_2H_2$	C_{2v}	
2-phenylvinyl	$n-A_1C_2H_2$	C_s	
1-vinyl-2-phenyl	$A_1C_2H_3*$	C_s	
1,2-diethynylbenzene	$A_1(C_2H)_2$	C_{2v}	
naphthalene	A_2	D_{2h}	
1-napthhyl	A_2-1	C_s	
2-napthhyl	A_2-2	C_s	
2-ethynylnaphthalene	A_2C_2HB	C_s	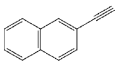
2-ethynyl-1-naphthyl	A_2C_2HB*	C_s	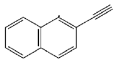
1-ethynylnaphthalene	A_2C_2HA	C_s	

species		symmetry group	geometrical representation
name	formula		
1-ethynyl-2-naphthyl	A_2C_2HA*	C_s	
vinylnaphthalene	$A_2C_2H_3$	C_1	
2-naphthylvinyl	$A_2C_2H_2$	C_1	
1,2-diethynylnaphthalene	$A_2(C_2H)_2$	C_s	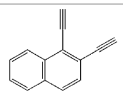
acenaphthylene	A_2R5	C_{2v}	
acenaphthyl	A_2R5-	C_s	
1-ethynylacenaphthylene	A_2R5C_2H	C_s	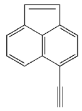
2-ethynyl-1-acenaphthyl	A_2R5C_2H*	C_s	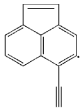
1,2-diethynylacenaphthylene	$A_2R5(C_2H)_2$	C_s	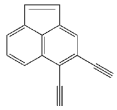
2-acenaphthylvinyl	$A_2R5C_2H_2$	C_1	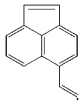
vinylacenaphthylene	$A_2R5C_2H_3$	C_1	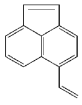
anthracene	A_3	D_{2h}	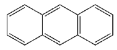
phenanphthrene	A_3	C_{2v}	
phenanphthryl	A_3-	C_s	
1-ethynylphenanphthrene	A_3C_2H	C_s	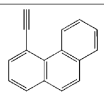

species		symmetry group	geometrical representation
name	formula		
2-phenanphthrylvinyl	$A_3C_2H_2$	C_1	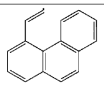
pyrene	$A_4(C_{16}H_{10})$	D_{2h}	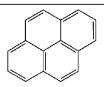
tetracene	$A_4(C_{18}H_{12})$	D_{2h}	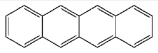
chrysene	$A_4(C_{18}H_{12})$	C_{2h}	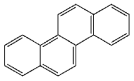
pyrenyl radical	A_4-	C_s	
acephenanphthrylene	A_3R5	C_s	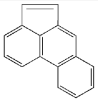
acephenanphthryl	A_3R5-	C_s	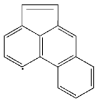

species		symmetry group	geometrical representation
name	formula		
1-ethynylacephenanphthrene	A_3R5C_2H	C_s	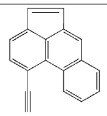
2-acephenanphthrylvinyl	$A_3R5C_2H_2$	C_1	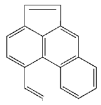
cyclopenta[cd]pyrene	A_4R5	C_s	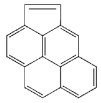
biphenyl	P_2	D_2	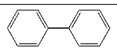
biphenyl radical	P_2-	C_1	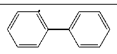
perylene	A_5	D_{2h}	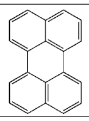
Coronene	A_7	D_{6h}	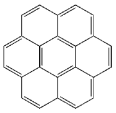

Appendix B

Thermodynamic properties of PAH

The following table provides the detailed thermodynamic properties of the Polycyclic Aromatic Hydrocarbons recomputed in Section 2. These data are expressed in the Chemkin format.

```
A1                G3B3  H   6C   6O   0N   0G   300.000  3000.000  1000.000    1
-2.06240612E-01 4.64122440E-02-2.77653536E-05 7.88910537E-09-8.60365259E-13    2
 8.09883905E+03 2.06566629E+01-5.51558393E+00 6.45453225E-02-4.41402928E-05    3
 7.47712161E-09 3.10282254E-12 9.11031457E+03 4.65332293E+01 1.43778102E+04    4
A1-               G3B3  H   5C   6O   0N   0G   300.000  3000.000  1000.000    1
 1.38016336E+00 4.04032009E-02-2.42250885E-05 6.88723321E-09-7.50960802E-13    2
 3.86973520E+04 1.55220921E+01-4.87654845E+00 6.26805782E-02-4.87402286E-05    3
 1.41122287E-08 5.18518312E-13 3.99269438E+04 4.59964173E+01 1.43462431E+04    4
A1C2H             G3B3  H   6C   8O   0N   0G   300.000  3000.000  1000.000    1
 5.81520488E+00 4.40872933E-02-2.52053858E-05 6.90275228E-09-7.31378908E-13    2
 3.30271906E+04-6.49320690E+00-5.21036925E+00 8.65551944E-02-8.45007483E-05    3
 4.21920706E-08-8.16766167E-12 3.52488620E+04 4.69445057E+01 1.98675349E+04    4
A1C2H-2           G3B3  H   5C   8O   0N   0G   300.000  3000.000  1000.000    1
 7.23812069E+00 3.83812109E-02-2.18850731E-05 5.97161247E-09-6.30351467E-13    2
 6.49528135E+04-1.17512654E+01-4.42757639E+00 8.36668645E-02-8.70106362E-05    3
 4.70285661E-08-1.01816985E-11 6.73302359E+04 4.48118287E+01 1.98764605E+04    4
```

```
A1C2H-3           G3B3  H   5C   8O   0N   0G   300.000  3000.000  1000.000    1
 7.31641956E+00 3.82473550E-02-2.17938546E-05 5.94358208E-09-6.27137621E-13    2
 6.54731852E+04-1.22582068E+01-4.56828912E+00 8.44648171E-02-8.84690497E-05    3
 4.81804208E-08-1.05215346E-11 6.78938976E+04 4.53532408E+01 1.98240414E+04    4
A1C2H-4           G3B3  H   5C   8O   0N   0G   300.000  3000.000  1000.000    1
 7.24042883E+00 3.83970829E-02-2.19039080E-05 5.97895043E-09-6.31309644E-13    2
 6.54533824E+04-1.25806584E+01-4.49496527E+00 8.39558238E-02-8.74231539E-05    3
 4.72827961E-08-1.02392561E-11 6.78447826E+04 4.43194923E+01 1.97905322E+04    4
A1C2H3            G3B3  H   8C   8O   0N   0G   300.000  3000.000  1000.000    1
 5.40554217E-01 6.17302362E-02-3.73947305E-05 1.07046587E-08-1.17304984E-12    2
 1.50413170E+04 2.14502681E+01-5.38499941E+00 8.20365155E-02-5.34461878E-05    3
 5.59095007E-09 5.61139050E-12 1.60857559E+04 5.01104513E+01 2.03770231E+04    4
i-A1C2H2          G3B3  H   7C   8O   0N   0G   300.000  3000.000  1000.000    1
 4.68084467E+00 5.04138194E-02-2.93058792E-05 8.13188132E-09-8.70428833E-13    2
 4.01230053E+04 8.98426155E-01-4.58086421E+00 8.50863874E-02-7.39245609E-05    3
 3.03983761E-08-3.92910114E-12 4.19664348E+04 4.58553205E+01 2.15359911E+04    4
n-A1C2H2          G3B3  H   7C   8O   0N   0G   300.000  3000.000  1000.000    1
 5.85935080E+00 4.72571459E-02-2.69864733E-05 7.35311775E-09-7.74900830E-13    2
 4.33198974E+04-5.22359403E+00-6.31199276E+00 9.51097942E-02-9.56352102E-05    3
 4.97780207E-08-1.02323717E-11 4.57330975E+04 5.35475222E+01 2.09496589E+04    4
A1C2H3*           G3B3  H   7C   8O   0N   0G   300.000  3000.000  1000.000    1
 3.90114779E+00 5.15894020E-02-3.05080522E-05 8.55910896E-09-9.23046757E-13    2
 4.59935428E+04 5.96930655E+00-5.36214520E+00 8.67033297E-02-7.54297960E-05    3
 3.01139854E-08-3.40681418E-12 4.77818209E+04 5.07407949E+01 2.08934947E+04    4
A1C2HX2           G3B3  H   6C  10O   0N   0G   300.000  3000.000  1000.000    1
 1.37021422E+01 3.75307154E-02-1.92386067E-05 4.75485847E-09-4.59816124E-13    2
 5.77849575E+04-4.54354786E+01-5.36135437E+00 1.12368754E-01-1.35377090E-04    3
 8.87716961E-08-2.41127122E-11 6.18686324E+04 4.73893049E+01 2.55807663E+04    4
A2                G3B3  H   8C  10O   0N   0G   300.000  3000.000  1000.000    1
 1.76826275E+00 6.89143506E-02-4.14322176E-05 1.17914309E-08-1.28597061E-12    2
 1.26883657E+04 1.06256608E+01-8.72434585E+00 1.05376008E-01-8.01710690E-05    3
 2.18545974E-08 1.42066606E-12 1.48059774E+04 6.19827540E+01 2.10522087E+04    4
```

```
A2-1              G3B3  H   7C  10O   0N   0G   300.000  3000.000  1000.000    1
 3.22892303E+00 6.31264486E-02-3.80582381E-05 1.08454069E-08-1.18342512E-12    2
 4.78400840E+04 5.82016697E+00-8.02718034E+00 1.02924518E-01-8.34272010E-05    3
 2.72135383E-08-7.24559554E-13 5.01363344E+04 6.08902264E+01 2.10209869E+04    4
A2-2              G3B3  H   7C  10O   0N   0G   300.000  3000.000  1000.000    1
 3.29950506E+00 6.30133365E-02-3.79760083E-05 1.08180756E-08-1.18007697E-12    2
 4.76658373E+04 5.41215697E+00-8.00768796E+00 1.03041289E-01-8.38190998E-05    3
 2.76491726E-08-8.88842208E-13 4.99740633E+04 6.07298980E+01 2.10265738E+04    4
A2C2HB            G3B3  H   8C  12O   0N   0G   300.000  3000.000  1000.000    1
 7.63899557E+00 6.69335855E-02-3.91500110E-05 1.08999883E-08-1.16865999E-12    2
 3.92947046E+04-1.61008215E+01-8.22579974E+00 1.26247551E-01-1.18140742E-04    3
 5.43987363E-08-9.12584671E-12 4.25495114E+04 6.11604165E+01 2.68441432E+04    4
A2C2HB*           G3B3  H   7C  12O   0N   0G   300.000  3000.000  1000.000    1
 8.88789581E+00 6.15504161E-02-3.60748511E-05 1.00510071E-08-1.07767823E-12    2
 7.39803629E+04-2.10417142E+01-7.35510706E+00 1.22525336E-01-1.18741281E-04    3
 5.74311178E-08-1.05232765E-11 7.73354743E+04 5.80872988E+01 2.68630047E+04    4
A2C2HA            G3B3  H   8C  12O   0N   0G   300.000  3000.000  1000.000    1
 7.55690939E+00 6.71073273E-02-3.92895768E-05 1.09479979E-08-1.17460930E-12    2
 3.91372224E+04-1.57914447E+01-8.23047877E+00 1.26053176E-01-1.17499124E-04    3
 5.36790980E-08-8.85462308E-12 4.23747629E+04 6.10991972E+01 2.67855027E+04    4
A2C2HA*           G3B3  H   7C  12O   0N   0G   300.000  3000.000  1000.000    1
 8.88459555E+00 6.15767170E-02-3.60988783E-05 1.00592710E-08-1.07867529E-12    2
 7.36259656E+04-2.12171362E+01-7.36585075E+00 1.22557991E-01-1.18737276E-04    3
 5.73940282E-08-1.05058631E-11 7.69836555E+04 5.79534391E+01 2.67813639E+04    4
A2C2H3            G3B3  H  10C  12O   0N   0G   300.000  3000.000  1000.000    1
 1.32975653E+01 5.93510763E-02-3.09957694E-05 7.76036896E-09-7.57379989E-13    2
 1.86786693E+04-4.64217734E+01-1.18619338E+01 1.53032993E-01-1.70232379E-04    3
 1.05825836E-07-2.81086546E-11 2.43633017E+04 7.74596078E+01 2.82106281E+04    4
A2C2H2            G3B3  H   9C  12O   0N   0G   300.000  3000.000  1000.000    1
 8.53385239E+00 6.87542797E-02-4.01750101E-05 1.11481146E-08-1.19062243E-12    2
 5.27583345E+04-1.97684170E+01-9.26784872E+00 1.35043130E-01-1.29791842E-04    3
 6.27220331E-08-1.16348577E-11 5.64832554E+04 6.71406964E+01 2.80382524E+04    4
```

```
A2C2HX2           G3B3  H   8C  14O   0N   0G   300.000  3000.000  1000.000    1
 1.81257820E+01 5.43540831E-02-2.82848502E-05 7.07124239E-09-6.89826849E-13    2
 6.28804722E+04-6.91206854E+01-8.96307203E+00 1.56379973E-01-1.80578142E-04    3
 1.13935574E-07-3.01979021E-11 6.89063443E+04 6.38788206E+01 3.26546072E+04    4
A2R5              G3B3  H   8C  12O   0N   0G   300.000  3000.000  1000.000    1
 3.65432884E+00 7.52647236E-02-4.54864951E-05 1.29795341E-08-1.41730827E-12    2
 2.65223472E+04 7.23303392E-01-1.05497902E+01 1.25536790E-01-1.03646045E-04    3
 3.52989130E-08-1.64508384E-12 2.94426605E+04 7.02667419E+01 2.34879850E+04    4
A2R5-             G3B3  H   7C  12O   0N   0G   300.000  3000.000  1000.000    1
 4.90108932E+00 6.98931618E-02-4.24225860E-05 1.21346296E-08-1.32683710E-12    2
 5.94391140E+04-3.69961369E+00-9.79699017E+00 1.22277213E-01-1.04932509E-04    3
 3.87946409E-08-3.16289661E-12 6.24840181E+04 6.82743775E+01 2.33744860E+04    4
A2R5C2H           G3B3  H   8C  14O   0N   0G   300.000  3000.000  1000.000    1
 9.29417050E+00 7.37696223E-02-4.35832594E-05 1.22153595E-08-1.31549318E-12    2
 5.14110057E+04-2.55650843E+01-9.95199604E+00 1.45413562E-01-1.39200806E-04    3
 6.55032994E-08-1.13836596E-11 5.53993662E+04 6.83019526E+01 2.93116490E+04    4
A2R5C2H*          G3B3  H   7C  14O   0N   0G   300.000  3000.000  1000.000    1
 1.06117453E+01 6.82675505E-02-4.04202391E-05 1.13372400E-08-1.22096366E-12    2
 8.51154522E+04-3.08958560E+01-9.09090029E+00 1.41918164E-01-1.40371367E-04    3
 6.90982381E-08-1.29788015E-11 8.92211518E+04 6.52159423E+01 2.93326739E+04    4
A2R5C2HX2         G3B3  H   8C  16O   0N   0G   300.000  3000.000  1000.000    1
 2.06921158E+01 5.91433246E-02-3.10721904E-05 7.82499471E-09-7.67637291E-13    2
 7.49180169E+04-8.33041119E+01-1.08000987E+01 1.76997102E-01-2.05947270E-04    3
 1.29982680E-07-3.44118058E-11 8.19644483E+04 7.15119755E+01 3.52772657E+04    4
A2R5C2H2          G3B3  H   9C  14O   0N   0G   300.000  3000.000  1000.000    1
 7.80126948E+00 8.14615345E-02-4.87650376E-05 1.38133442E-08-1.50000241E-12    2
 6.50870635E+04-1.66224782E+01-9.79888742E+00 1.45400515E-01-1.28359949E-04    3
 5.15868534E-08-6.01742362E-12 6.87094743E+04 6.93517594E+01 3.05830258E+04    4
A2R5C2H3          G3B3  H  10C  14O   0N   0G   300.000  3000.000  1000.000    1
 5.52003394E+00 8.91008738E-02-5.35154567E-05 1.52092570E-08-1.65642383E-12    2
 3.36285582E+04-5.99395171E+00-9.71641225E+00 1.42587793E-01-1.13607750E-04    3
 3.58788724E-08-4.84218311E-13 3.67504645E+04 6.86319946E+01 3.07499411E+04    4
```

```
A3                G3B3  H  10C  14O   0N   0G   300.000  3000.000  1000.000    1
 3.62268555E+00 9.17532610E-02-5.53932771E-05 1.57984276E-08-1.72476358E-12    2
 2.25116223E+04 1.58651567E-01-1.16564026E+01 1.44874841E-01-1.13500194E-04    3
 3.37638751E-08 5.74214422E-13 2.56477354E+04 7.50715049E+01 2.82496236E+04    4
A3                G3B3  H  10C  14O   0N   0G   300.000  3000.000  1000.000    1
 3.38725839E+00 9.21885604E-02-5.57286994E-05 1.59123919E-08-1.73884258E-12    2
 1.91061794E+04 2.24294382E+00-1.15461369E+01 1.43758163E-01-1.10869124E-04    3
 3.12180141E-08 1.45975232E-12 2.21687904E+04 7.54982708E+01 2.82874719E+04    4
A3-               G3B3  H   9C  14O   0N   0G   300.000  3000.000  1000.000    1
 4.71264594E+00 8.67230002E-02-5.26011632E-05 1.50459549E-08-1.64563976E-12    2
 5.37939644E+04-2.69867594E+00-1.08881743E+01 1.41187077E-01-1.13531428E-04    3
 3.59175357E-08-4.50212032E-13 5.70158539E+04 7.38129777E+01 2.81655136E+04    4
A3C2H             G3B3  H  10C  16O   0N   0G   300.000  3000.000  1000.000    1
 9.22849694E+00 9.03138321E-02-5.35519070E-05 1.50612110E-08-1.62682557E-12    2
 4.60974425E+04-2.44714627E+01-1.11174384E+01 1.64862353E-01-1.48933465E-04    3
 6.35625044E-08-8.94914690E-12 5.03021108E+04 7.48790195E+01 3.41764376E+04    4
A3C2H2            G3B3  H  11C  16O   0N   0G   300.000  3000.000  1000.000    1
 7.22603489E+00 9.83998189E-02-5.90146454E-05 1.67470805E-08-1.82147310E-12    2
 6.22651455E+04-1.48176474E+01-1.16614100E+01 1.65960836E-01-1.39356763E-04    3
 5.02980423E-08-3.70389013E-12 6.61415304E+04 7.75491911E+01 3.44423049E+04    4
A4                G3B3  H  10C  16O   0N   0G   300.000  3000.000  1000.000    1
 4.54060055E+00 9.98115207E-02-6.06376301E-05 1.73575019E-08-1.89902318E-12    2
 2.12755890E+04-6.19295231E+00-1.31524443E+01 1.60878843E-01-1.27719717E-04    3
 3.90918898E-08 7.43991125E-14 2.49673872E+04 8.07618418E+01 3.00634243E+04    4
A4                G3B3  H  12C  18O   0N   0G   300.000  3000.000  1000.000    1
 5.56187101E+00 1.14459178E-01-6.92665744E-05 1.97788045E-08-2.16052176E-12    2
 3.13580577E+04-1.07435666E+01-1.46027261E+01 1.84682793E-01-1.47520503E-04    3
 4.62742042E-08-4.61011132E-13 3.55317380E+04 8.81952068E+01 3.56333707E+04    4
A4                G3B3  H  12C  18O   0N   0G   300.000  3000.000  1000.000    1
 5.08081742E+00 1.15309317E-01-6.99119694E-05 1.99971593E-08-2.18747457E-12    2
 2.45866645E+04-7.15205827E+00-1.43182817E+01 1.82115126E-01-1.41735636E-04    3
 4.08234628E-08 1.40317913E-12 2.85993748E+04 8.81184309E+01 3.57239746E+04    4
```

```
A4-               G3B3  H   9C  16O   0N   0G   300.000  3000.000  1000.000    1
 5.85098138E+00 9.43231105E-02-5.74898152E-05 1.64858853E-08-1.80541509E-12    2
 5.89572568E+04-1.02177357E+01-1.23671835E+01 1.57657515E-01-1.29243633E-04    3
 4.28629673E-08-1.54491879E-12 6.27797890E+04 7.93139090E+01 2.99983238E+04    4
A3R5              G3B3  H  10C  16O   0N   0G   300.000  3000.000  1000.000    1
 5.07024731E+00 9.89917305E-02-6.01400259E-05 1.72204585E-08-1.88476151E-12    2
 3.06528296E+04-6.72179815E+00-1.32241574E+01 1.62862647E-01-1.31967056E-04    3
 4.24393865E-08-8.53171724E-13 3.44430693E+04 8.30298639E+01 3.08028224E+04    4
A3R5-             G3B3  H   9C  16O   0N   0G   300.000  3000.000  1000.000    1
 6.47777347E+00 9.33337716E-02-5.68626896E-05 1.63046727E-08-1.78566643E-12    2
 6.47489852E+04-1.26768700E+01-1.25419370E+01 1.60371016E-01-1.35029003E-04    3
 4.76044093E-08-2.93662303E-12 6.87107686E+04 8.06070415E+01 3.07355313E+04    4
A3R5C2H           G3B3  H   0C   0O   0N   0G   300.000  3000.000  1000.000    1
 1.09363963E+01 9.70461008E-02-5.79061978E-05 1.63504098E-08-1.77049851E-12    2
 5.69856157E+04-3.48364372E+01-1.28179751E+01 1.84105804E-01-1.70347251E-04    3
 7.50708926E-08-1.13552597E-11 6.19273182E+04 8.12364671E+01 3.66201278E+04    4
A4R5              G3B3  H  10C  18O   0N   0G   300.000  3000.000  1000.000    1
 6.20190827E+00 1.06656275E-01-6.50829301E-05 1.86776130E-08-2.04647350E-12    2
 3.34439422E+04-1.42387586E+01-1.47695663E+01 1.79658022E-01-1.48189900E-04    3
 4.97722102E-08-2.06437335E-12 3.78467972E+04 8.88184030E+01 3.26588481E+04    4
P2                G3B3  H  10C  12O   0N   0G   300.000  3000.000  1000.000    1
 5.73686527E+00 7.54659445E-02-4.38684869E-05 1.21616109E-08-1.30012291E-12    2
 1.66022411E+04-7.75535705E+00-1.19438051E+01 1.42163159E-01-1.33497449E-04    3
 6.20505718E-08-1.05766664E-11 2.01936932E+04 7.81851355E+01 2.68791478E+04    4
P2-               G3B3  H   9C  12O   0N   0G   300.000  3000.000  1000.000    1
 3.97670430E+00 7.79432070E-02-4.74482168E-05 1.36376082E-08-1.49857832E-12    2
 5.02964162E+04 3.31269296E+00-9.50091731E+00 1.25210503E-01-9.83718223E-05    3
 2.75934175E-08 1.67954345E-12 5.29903482E+04 6.91608446E+01 2.67481900E+04    4
A5                G3B3  H  12C  20O   0N   0G   300.000  3000.000  1000.000    1
 6.03814479E+00 1.23420577E-01-7.52509905E-05 2.15982407E-08-2.36762799E-12    2
 2.94432380E+04-1.35373546E+01-1.56026351E+01 1.97485831E-01-1.54773542E-04    3
 4.50107010E-08 1.31798892E-12 3.39686695E+04 9.29223208E+01 3.79790075E+04    4
```

```
A7               G3B3  H  12C  24O   0N   0G   300.000  3000.000  1000.000    1
 8.19741179E+00 1.39201992E-01-8.55704378E-05 2.46727618E-08-2.71164580E-12    2
 2.90655397E+08-3.02293408E+01-1.69421713E+01 2.23766155E-01-1.74659551E-04    3
 4.97168313E-08 1.90881808E-12 2.90660766E+08 9.39060014E+01 4.11748232E+04    4
```

Appendix C

The FlameMaster Code

The FlameMaster code is a program designed to solve numerically typical problems found in combustion processes. Several different configurations are supported such as computations of homogeneous ignition delay times, laminar burning velocities, premixed flames, or counterflow diffusion flames. The following description provides an overview of the configurations and the equations solved.

C.1 General Description

The FlameMaster code relies on detailed chemical mechanisms to solve the different combustion problems. These chemical mechanisms are composed of thermodynamic and transport properties for each species in the system and a list of reactions among these species.

C.1.1 Thermodynamic Properties

The thermodynamic properties for agiven species at a given temperature T, such as heat capacity ($C_p(T)$), enthalpy content ($H(T)$), and entropy ($S(T)$), are evaluated

by polynomial interpolation as follows

$$\frac{C_p(T)}{R} = a_1 + a_2 T + a_3 T^2 + a_4 T^3 + a_5 T^4 \tag{C.1}$$

$$\frac{H(T)}{R} = a_1 + \frac{a_2}{2} T + \frac{a_3}{3} T^2 + \frac{a_4}{4} T^3 + \frac{a_5}{5} T^4 + \frac{a_6}{T} \tag{C.2}$$

$$\frac{S(T)}{R} = a_1 \ln T + a_2 T + \frac{a_3}{2} T^2 + \frac{a_4}{3} T^3 + \frac{a_5}{4} T^4 + a_7 \tag{C.3}$$

where R is the universal gas constant. The seven parameters (a_1 to a_7) are constant and are different for different species. To improve the quality of the polynomial fit, two sets of parameters are used. The first set is used for low temperatures ($1000\,\mathrm{K} > T$) and the second set for high temperatures ($T > 1000\,\mathrm{K}$).

C.1.2 Reaction Rates

Suppose the following reaction

$$\sum_{j=1}^{n} \nu_{ij}\, \mathrm{S_j} \leftrightarrows \sum_{j=1}^{n} \nu'_{ij}\, \mathrm{S_j}\,, \tag{C.4}$$

where $\mathrm{S_j}$ is the j-th species in the system and ν_{ij} is the stoichiometric coefficient for species j in reaction i. For a given reaction, the rate constant of the reaction is expressed in the modified Arrhenius form which describes its temperature dependence

$$k_i(T) = A_i T^{n_i} \exp\left(-\frac{E_i}{RT}\right)\,. \tag{C.5}$$

The reaction rate is simply evaluated from the forward (k_{if}) and backward (k_{ib}) rate constants as

$$\omega_i = k_{if} \prod_{j=1}^{n} \left(\frac{\rho Y_j}{W_j}\right)^{\nu_{ij}} - k_{ib} \prod_{j=1}^{n} \left(\frac{\rho Y_j}{W_j}\right)^{\nu'_{ij}}\,, \tag{C.6}$$

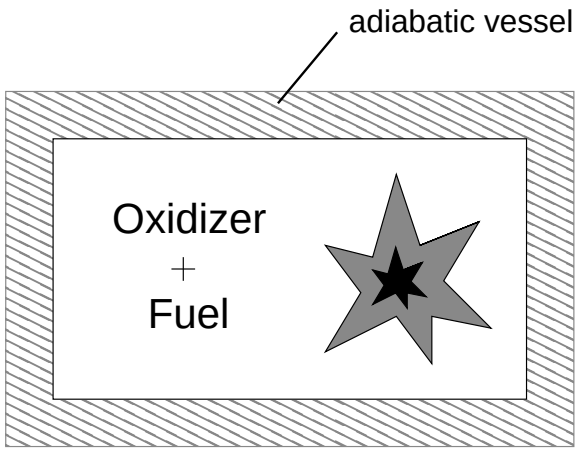

Figure C.1: Sketch of a constant volume vessel used to measure ignition delay times

where ρ is the density and Y_j and W_j are the mass fraction and the molecular weight of species j, respectively.

C.2 Homogeneous 0D Reactors

Figure C.1 shows a sketch of a constant volume vessel used to compute ignition delay times. During the ignition, the pressure and temperature will increase due to heat release. The configuration is assumed to be perfectly homogeneous. The 0D equations describing the temporal evolution of the system are expressed as follows

$$\rho \frac{dY_j}{dt} = W_j \omega_j \,, \tag{C.7}$$

$$\rho \left(c_p - \frac{R}{W} \right) \frac{dT}{dt} + \sum_{j=1}^{n} \left(h_j - \frac{R}{W_j} \right) W_j \omega_j = 0 \,, \tag{C.8}$$

where c_p and W are the mixture averaged specific heat and molecular weight defined as

$$c_p = \sum_{j=1}^{n} Y_j c_{p_j} \tag{C.9}$$

and

$$W = \left(\sum_{j=1}^{n} \frac{Y_j}{W_j} \right)^{-1} . \tag{C.10}$$

For the considered system, the density is constant, and the pressure P is computed from the equation of state

$$P = \frac{\rho R T}{W} . \tag{C.11}$$

C.3 1D Laminar Flames

C.3.1 Transport Properties

The diffusion velocity is decomposed into three parts

$$v_j = v_j^D + v_j^T + v_c \tag{C.12}$$

where v_j^D is the molecular diffusion, v_j^T is the thermal diffusion (Soret effect), and v_c is the velocity correction (the same value for each species). The molecular diffusion takes the following form

$$v_j^D = -\frac{D_j}{X_j} \nabla X_j \tag{C.13}$$

where X_j is the mole fraction of species j and D_j is the average diffusion coefficient of species j in the mixture. This coefficient is evaluated from the binary diffusion coefficient as

$$D_j = \frac{1 - \sum_{k=1}^{n} Y_k}{\sum_{k \neq j} \frac{X_k}{D_{jk}}} \tag{C.14}$$

In order to conserve mass, the total mass flux due to diffusion should be exactly zero

$$\sum_{j=1}^{n} Y_j v_j = 0 . \tag{C.15}$$

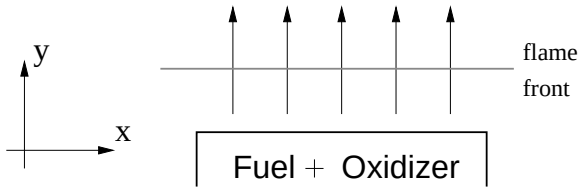

Figure C.2: Sketch of a burner stabilized premixed flame

This condition is ensured by defining the velocity correction as

$$v_c = -\sum_{j=1}^{n} Y_j \cdot (v_j^D + v_j^T)\,. \tag{C.16}$$

C.3.2 Mixture-averaged properties

Dynamic viscosity and thermal conductivity of the mixture are calculated with semi-empirical formulae

$$\mu = \sum_{j=1}^{n} \frac{Y_j \mu_j}{\Delta_j} \tag{C.17}$$

with

$$\Delta_j = \sum_{k=1}^{n} G_{jk} \frac{M_j}{M_k} Y_k \tag{C.18}$$

where

$$G_{jk} = \frac{1}{\sqrt{8}} \left(1 + \frac{W_j}{W_k}\right)^{-1/2} \left[1 + \left(\frac{\mu_j}{\mu_k}\right)^{1/2} \left(\frac{W_k}{W_j}\right)^{1/4}\right]^2 . \tag{C.19}$$

The mixture-averaged thermal conductivity is evaluated as

$$\lambda = \frac{1}{2} \left[\sum_{j=1}^{n} X_j \lambda_j + \left(\sum_{j=1}^{n} \frac{X_j}{\lambda_j}\right)^{-1}\right] . \tag{C.20}$$

C.3.3 Premixed Flames

Figure C.2 shows a sketch of a typical laminar premixed flame. In this configuration, both the fuel and the oxidizer are premixed before being injected through the nozzle.

The flow field is assumed to be homogeneous in the spanwise direction, and thus the configuration is assumed to be one-dimensional. The equations for $1D$ laminar premixed flames are as follows

$$\rho V = \text{const}\,, \tag{C.21}$$

$$\rho V \frac{dY_j}{dy} + \frac{d}{dy}\left(\rho Y_j v_j\right) = W_j \omega_j\,, \tag{C.22}$$

$$\rho V C_p \frac{dT}{dy} - \frac{d}{dy}\left(\lambda \frac{dT}{dy}\right) + \frac{d}{dy}\left(\rho Y_j v_j C_{p_j} \frac{dT}{dy}\right) + \sum_{j=1}^{n} h_j W_j \omega_j = 0\,, \tag{C.23}$$

where V is the vertical velocity. These equations can represent two different premixed configurations:

- For burner stabilized flames, the mass flow rate (ρV) is prescribed and the flame is stabilized over the burner surface.
- To compute laminar burning velocities, the temperature of one point inside the domain is prescribed. Then, the mass flow rate becomes an eigenvalue of the problem.

C.3.4 Counterflow Diffusion Flame

Figure C.3 shows a sketch of a typical laminar counterflow diffusion flame. In this configuration, the fuel is injected though a nozzle and the oxidizer is injected though a different nozzle. In certain cases, a mixture of both oxidizer and fuel could be injected. As the flow coming from both nozzles are diverted away, a stagnation plane is formed. The flame front typically sits on the fuel side of the stagnation plane. Considering the different quantities on the axis of symmetry ($x = 0$), the equations for counterflow diffusion flames are as follows

$$\frac{d(\rho V)}{dy} + 2\rho G = 0\,, \tag{C.24}$$

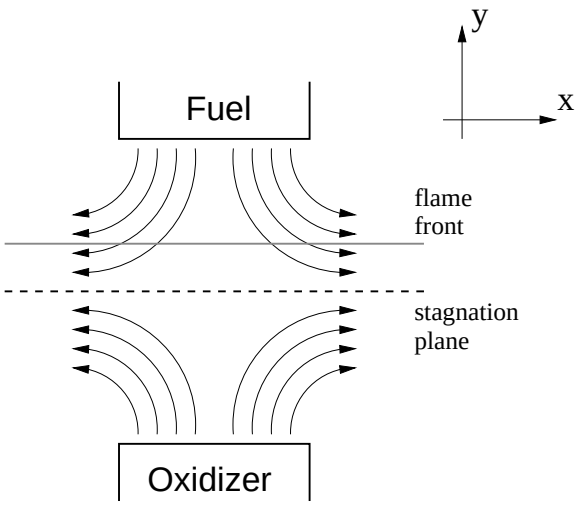

Figure C.3: Sketch of a counterflow diffusion flame

$$\rho V \frac{dG}{dy} = -\rho G^2 + P' + \frac{d}{dy}\left(\mu \frac{dG}{dy}\right) , \tag{C.25}$$

$$\rho V \frac{dY_j}{dy} + \frac{d}{dy}\left(\rho Y_j v_j\right) = W_j \omega_j , \tag{C.26}$$

$$\rho V C_p \frac{dT}{dy} - \frac{d}{dy}\left(\lambda \frac{dT}{dy}\right) + \frac{d}{dy}\left(\rho Y_j v_j C_{p_j} \frac{dT}{dy}\right) + \sum_{j=1}^{n} h_j W_j \omega_j = 0 , \tag{C.27}$$

where G is defined as the derivative of the u velocity component on the axis

$$u(x, y) = G(y) \cdot x , \tag{C.28}$$

and P' is the constant axial pressure gradient and can be expressed as a function of the strain rate as

$$P' = \rho_\infty a^2 . \tag{C.29}$$

Bibliography

[1] G. L. Agafonov, I. Naydenova, P.A. Vlasov, and J. Warnatz. Detailed kinetic modeling of soot formation in shock tube pyrolysis and oxidation of toluene and n-heptane. *Proc. Comb. Inst.*, 31:575–583, 2007.

[2] J. Aguilera-Iparraguirre and W. Klopper. Density functional theory study of the formation of naphthalene and phenanthrene from reactions of phenyl with vinyl- and phenylacetylene. *J. Chem. Theory. Comput.*, 3:139–145, 2007.

[3] M. Alfe, B. Apicella, R. Barbella, A. Tregrossi, and A. Ciajolo. Similarities and dissimilarities in n-hexane and benzene sooting premixed flames. *Proc. Comb. Inst.*, 31:585–591, 2007.

[4] A. Almenningen, O. Bastiansen, L. Frenholt, B. Cyvin, and S. Smdal. *J. Mol. Struct.*, 128:59–76, 1985.

[5] J Appel, H. Bockhorn, and M. Frenklach. Kinetic modeling of soot formation with detailed chemistry and physics: Laminar premixed flames of c_2 hydrocarbons. *Comb. Flame.*, 121:122–136, 2000.

[6] A. G. Baboul, L. A. Curtiss, and P. C. Redfern. *J. Chem. Phys.*, 110:7650–, 1999.

[7] A. E. Bakali, J. L. Delfau, and C. Vovelle. Measurement of soot volume fraction and gaseous species concentrations in premixed n-heptane and iso-octane flames. *J. Chim. Phys.*, 94:1659–1673, 1997.

[8] A. E. Bakali, J. L. Delfau, and C. Vovelle. Experimental study of 1 atmosphere, rich, premixed n-heptane and iso-octane flames. *Comb. Sci. Tech.*, 140:69–91, 1998.

[9] M. Balthasar and M. Frenklach. Detailed kinetic modeling of soot aggregate formation in laminar premixed flames. *Comb. Flame*, 140:130–145, 2005.

[10] O. Bastiansen and S. Samdal. *J. Mol. Struct.*, 128:115–125, 1985.

[11] D.L. Baulch, C.T. Bowman, C.J. Cobos, R.A. Cox, T. Just, J.A. Kerr, M.J. Pilling, D. Stocker, J. Troe, W. Tsang, R. W. Walker, and J. Warnatz. Evaluated kinetic data for combustion modeling: supplement II. *J. Phys. Chem. ref. Data*, 34:757–1397, 2005.

[12] A. D. Becke. *J. Chem. Phys.*, 98:5648–, 1993.

[13] S. W. Benson. *Thermochemical kinetics, 2nd ed.* Willey, New York, 1976.

[14] P. Berta, S. K. Aggarwal, and I. K. Puri. An experimental and numerical investigation of n-heptane/air counterflow partially premixed flames and emission of nox and pah species. *Comb. Flame*, 145:740–764, 2006.

[15] M.A. Blitz, M.S. Beasley, M.J. Pilling, and S.H. Robertson. Formation of the propargyl radical in the reaction of ch_2 and c_2h_2: experiment and modelling. *Phys. Chem. Chem. Phys.*, 2:805–812, 2000.

[16] H. Böhm, D. Hesse, H. Jander, B. Lüers, J. Pietscher, H. GG. Wagner, and M. Weiss. personal communication, 1988.

[17] H. Bohm, D. Hesse, H. Jander, B. Luers, J. Pietscher, H. GG. Wagner, and M. Weiss. The influence of pressure and temperature on soot formation in premixed flames. *Proc. Comb. Inst.*, 22:403–411, 1988.

[18] M. Bönig, C. Feldermann, H. Jander, B. Lüers, G. Rudolph, and H. GG. Wagner. The influence of pressure and temperature on soot formation in premixed flames. *Proc. Comb. Inst.*, 23:1581–1587, 1990.

[19] C. J. Brown and G. O. Thomas. Experimental studies of shock-induced ignition and transition to detonation in ethylene and propane mixtures. *Comb. Flame*, 117:861–870, 1999.

[20] A. Burcat, A. Lifshitz, K. Scheller, and G. B. Skinner. Shock-tube investigation of ignition in propane-oxygen-argon mixtures. *Proc. Comb. Inst.*, 13:745–755, 1970.

[21] A. Burcat and B. Ruscic. Ideal gas thermochemical database with updates from active thermochemical tables. ftp://ftp.technion.ac.il/pub/supported/aetdd/thermodynamics/, 2008.

[22] A. Burcat, C. Snyder, and T. Brabbs. Ignition delay times of benzene and toluene with oxygen in argon mixtures. Technical Report TM-87312, NASA, 1986.

[23] W. Caminati, B. Vogelsanger, and A. Bauder. *J. Mol. Spec.*, 128:384–398, 1988.

[24] L. A. Carreira and T. G. Towns. *J. Mol. Struct.*, 41:1–, 1977.

[25] H.H. Carstensen and A.M. Dean. Rate constants for the abstraction reacstions $ro_2 + c_2h_6$; r = h, ch_3, and c_2h_5. *Proc. Comb. Inst.*, 30:995–1003, 2005.

[26] NIST computational chemistry comparison and benchmark database, NIST standard reference database number 101 release 14, sept 2006, Editor: Russell D. Johnson III, http://srdata.nist.gov/cccbdb/.

[27] M. Celnik, A. Raj, R. West, R. Patterson, and M. Kraft. An aromatic site description of soot particles. *Proc. Int. Workshop on Combustion Generated Fine Carbon Particles*, 2008.

[28] B. Ceursters, H.M.T. Nguyen, J. Peeters, and M.T. Nguyen. Experimental and theoretical study of the reaction of the ethynyl radical with acetylene. *Chem. Phys.*, 262:243–252, 2000.

[29] M. W. Chase. *J. Phys. Chem. Ref. Data*, 9:–, 1998.

[30] R. D. Chirico, S. E. Knipmeyer, S. Nguen, and W. V. Steele. *J. Chem. Thermodyn.*, 21:1307–1331, 1989.

[31] Y. M. Choi, W. S. Xia, J. Park, and M. C. Lin. Kinetics and mechanism for the reaction of phenyl radical with formaldehyde. *J. Phys. Chem. A*, 104:7030–7035, 2006.

[32] H. K. Ciezki and G. Adomeit. Shock-tube investigation of self-ignition of n-heptane-air mixtures under engine relevant conditions. *Comb. Flame*, 93:421–433, 1993.

[33] J. C. Cochran, K. Hagen, G. Paulen, Q. Shen, S. Tom, M. Tracetteberg, and C. Wells. *J. Mol. Struct.*, 413-4:313–326, 1997.

[34] M. Colket, T. Edwards, S. Williams, N.P. Cernansky, D.L. Miller, F. Egolfopoulos, P. Lindstedt, K. Seshadri, F.L. Dryer, C.K. Law, D. Friend, D.B. Lenhert,

H. Pitsch, A.F. Sarofim, M. Smooke, and W. Tsang. Development of an experimental database and kinetic models for surrogate jet fuels. In *45th AIAA Aerospace Sciences Meeting and Exhibit, Reno, Nevada, Jan. 8-11*, 2007.

[35] M. B. Colket and R. J. Hall. Successes and uncertainties in modeling soot formation in laminar, premixed flames. In H. Bockhorn, editor, *Soot Formation in Combustion-Mechanism and Models*, pages 442–470. Springer-Verlag, 1994.

[36] H. Curran, J. M. Simmie, P. Dagaut, D. Voisin, and M. Cathonnet. The ignition and oxidation of allene and propyne: Experiments and kinetic modeling. *Proc. Comb. Inst.*, 26:613–620, 1996.

[37] H. J. Curran. Rate constant estimation for c-1 to c-4 alkyl and alkoxyl radical decomposition. *Int. J. Chem. Kin.*, 38:250–275, 2006.

[38] H. J. Curran, P. Gaffuri, W. J. Pitz, and C. K. Westbrook. A comprehensive modeling study of n-heptane oxidation. *Comb. Flame*, 114:149–177, 1998.

[39] H. J. Curran, P. Gaffuri, W. J. Pitz, and C. K. Westbrook. A comprehensive modeling study of iso-octane oxidation. *Comb. Flame*, 129:253–280, 2002.

[40] A. D'Alessio, A. C. Barone, R. Cau, A. D'Anna, and P. Minutolo. Surface deposition and coagulation efficiency of combustion generated nanoparticles in the size range from 1 to 10nm. *Proc. Comb. Inst.*, 30:2595–2603, 2005.

[41] A. D'Anna, M. Alfe, B. Apicella, A. Tregrossi, and A. Ciajolo. Effect of fuel/air ratio and aromaticity on sooting behavior of premixed heptane flames. *Energy and Fuels*, 21:2655–2662, 2007.

[42] A. D'Anna and J. H. Kent. Aromatic formation pathways in non-premixed methane flames. *Comb. Flame*, 132:715–722, 2003.

[43] D. Darius, N. Chaumeix, and C. Paillard. Pyrolysis and oxidation of n-decane and n-propylbenzene and kerosene surrogate behing reflected shock waves. *International Workshop on Combustion Generated Fine Carbon Particles*, 2008.

[44] D. F. Davidson, B. M. Gauthier, and R. K. Hanson. Shock tube ignition measurements of iso-octane/air and toluene/air at high pressures. *Proc. Comb. Inst.*, 30:1175–1182, 2005.

[45] S. G. Davis and C. K. Law. Determination of and fuel structure effects on laminar flame speeds of c_1 to c_8 hydrocarbons. *Comb. Sci. Tech.*, 140:427–449, 1998.

[46] S.G. Davis, C.K. Law, and . Wanh, H. Propyne pyrolysis in flow reactor: An experimental, rrkm, and detailed kinetic modeling study. *J. Phys. Chem. A*, 103:5889–5899, 1999.

[47] J. de Vries, J. M. Hall, S. L. Simmons, M. J. A. Rickard, D. M. Kalitan, and E. L. Petersen. Ethane ignition and oxidation behind reflected shock waves. *Comb. Flame*, 150:137–150, 2007.

[48] H. P. Diogo, G. Persy, and M. E. Minas da Pedale. *J. Org. Chem.*, 61:6733–6734, 1996.

[49] Z. M. Djurisic. Detailed kinetic modeling of benzene and toluene oxidation at high temperatures. http://diesel.me.berkeley.edu/∼zoran/ publications/2000_MS_Thesis.

[50] Z. M. Djurisic. Detailed kinetic modeling of benzene and toluene oxidation at high temperatures. Master's thesis, University of Delaware, Newark, DE, November 1999.

[51] F. N. Egolfopoulos, D. L. Zhu, and C. K. Law. Experimental and numerical determination of laminar flame speeds. *Proc. Comb. Inst.*, 23:471–478, 1990.

[52] B. Eiteneer and M. Frenklach. Experimental and modeling study of shock-tube oxidation of acetylene. *Int. J. Chem. Kinet.*, 35:391–414, 2003.

[53] A. Fattahi, S. R. Kass, J. F. Liebman, M. A. R. Matos, M. S. Miranda, and V. M. F. Morais. The enthalpies of formation of o-, m-, and p-benzoquinone: Gas-phase ion eneretics, combustion calorimetry, and quantum chemical computations combined. *J. Am. Chem. Soc.*, 127:6116–6122, 2005.

[54] K. Fieweger, R. Blumenthal, and G. Adomeit. Self-ignition of s.i. engine model fuels: A shock tube investigation at high pressure. *Comb. Flame*, 109:599–619, 1997.

[55] R. Fournet, J. C. Bauge, and F. Battin-Leclerc. Experimental and modeling of oxidation of acetylene, propyne, allene and 1,3-butadiene. *Int. J. Chem. Kin.*, 31:361–379, 1999.

[56] R. O. Fox. Bivariate direct quadrature method of moments for coagulation and sintering of particle populations. *J. Aerosol Sci.*, 37:1562–1580, 2006.

[57] M. Frenklach, D. W. Clary, T. Yuan, W. C. Jr. Gardiner, and S. E. Stein. *Combust. Sci. Technol.*, 50:79–, 1986.

[58] M. Frenklach, C. A. Schuetz, and J. Ping. Migration mechanism of aromatic-egde growth. *Proc. Combust. Inst.*, 30:1389–1396, 2005.

[59] M Frenklach and H Wang. Detailed modeling of soot particle nucleation and growth. *Proc. Comb. Inst.*, 23:1559–1566, 1991.

[60] S. K. Friedlander. Wiley & Sons, 1986.

[61] M. J. Frisch, G. W. Trucks, H. B. Schlegel, G. E. Scuseria, M. A. Robb, J. R. Cheeseman, J. A. Montgomery, Jr.., T. Vreven, K. N. Kudin, J. C. Burant, J. M. Millam, S. S. Iyengar, J. Tomasi, V. Barone, B. Mennucci, M. Cossi, G. Scalmani, N. Rega, G. A. Petersson, H. Nakatsuji, M. Hada, M. Ehara, K. Toyota, R. Fukuda, J. Hasegawa, M. Ishida, T. Nakajima, Y. Honda, O. Kitao, H. Nakai, M. Klene, X. Li, J. E. Knox, H. P. Hratchian, J. B. Cross, C. Adamo, J. Jaramillo, R. Gomperts, R. E. Stratmann, O. Yazyev, A. J. Austin, R. Cammi, C. Pomelli, J.W. Ochterski, P. Y. Ayala, K. Morokuma, G. A. Voth, P. Salvador, J. J. Dannenberg, V. G. Zakrzewski, S. Dapprich, A. D. Daniels, M. C. Strain, O. Farkas, D. K. Malick, A. D. Rabuck, K. Raghavachari, J. B. Foresman, J. V. Ortiz, Q. Cui, A. G. Baboul, S. Clifford, J. Cioslowski, B. B. Stefanov, G. Liu, A. Liashenko, P. Piskorz, I. Komaromi, R. L. Martin, D. J. Fox, T. Keith, M. A. Al-Laham, C. Y. Peng, A. Nanayakkara, M. Challacombe, P.M.W. Gill, B. Johnson, W. Chen, M. W. Wong, C. Gonzalez, and J. A. Pople. Gaussian 03, revision c.01, gaussian, inc., wallingford ct, 2004., 2003.

[62] B. M. Gauthier, D. F. Davidson, and R. K. Hanson. Shock tube determination of ignition delay times in full-blend and surrogate fuel mixtures. *Comb. Flame*, 139:300–311, 2004.

[63] K. P. Geigle, Y. Schneider-Kuhnle, M. S. Tsurikov, R. Hadef, R. Luckerath, V. Kruger, W. Stricker, and M. Aigner. Investigation of laminar pressurixed flames for soot model validation using SV-CARS and LII. *Proc. Comb. Inst.*, 30:1645–1653, 2005.

[64] M. Goodson and M. Kraft. An efficient stochastic algorithm for simulating nano-particle dynamics. *J. Comp. Phys.*, 183:210–232, 2002.

[65] R.G. Gordon. Error bounds in equlibrium statistical mechanics. *J. Math. Phys.*, 9:655, 1968.

[66] D.K. Hahn, S.J. Klippenstein, and J.A. Miller. A theoertical analysis of the reaction between propargyl and molecular axygen. *Faraday Discuss.*, 119:79–100, 2001.

[67] L. B. Harding, Y. Georgievskii, and S. J. Klippenstein. Predictive theory for hydrogen atom-hydrocarbon radical association kinetics. *J. Phys. Chem. A*, 109:4646–4656, 2005.

[68] L. B. Harding, S. J. Klippenstein, and Y. Georgievskii. Reactions of oxygen atoms with hydrocarbon radicals: a priori kinetic predictions for the $ch_3 + o$, $c_2h_5 + o$, and $c_2h_3 + o$ reactions. *Proc. Comb. Inst.*, 30:985–993, 2005.

[69] S. J. Harris and A. M. Weiner. Surface growth of soot particles in premixed ethylene/air flames. *Combust. Sci. Technol.*, 31:155–167, 1983.

[70] M. I. Hassan, K. T. Aung, and G. M. Faeth. Measured and predicted properties of laminar premixed methane/air flames at various pressures. *Comb. Flame*, 115:539–550, 1998.

[71] W. J. Hehre, L. R. , J. A. Pople, and P. v. R. Schleyer. *Ab Initio Molecular Orbital Theory*. Willey, New York, 1987.

[72] G. Herzberg. *Electronic spectra and electronic structure of polyatomic molecules*. Van Norstrand, New York, 1966.

[73] Y. Hidaka, K. Hattori, T. Okuno, K. Inami, and T. Koike. Shock-tube and modeling study of acetylene pyrolysis and oxidation. *Comb. Flame*, 107:401–417, 1996.

[74] Y. Hidaka, Y. Henmi, T. Ohonishi, and T. Okuno. Shock-tube and modeling study of diacetylene pyrolysis and oxidation. *Comb. Flame*, 130:62–82, 2002.

[75] Y. Hidaka, T. Nishimori, K. Sato, R. Henmi, Y. Okuda, K. Inami, and T. Higashihara. Shock-tube and modeling study of ethylene pyrolysis and oxidation. *Comb. Flame*, 117:755–776, 1999.

[76] T. Hirasawa, C. J. Sung, A. Joshi, Z. Yang, H. Wang, and C. K. Law. Determination of laminar flame speeds using digital particle image velocimetry: Binary fuel blends of ethylene, n-butane, and toluene. *Proc. Comb. Inst.*, 29:1427–1434, 2002.

[77] Z. Hong, D. F. Davidson, S. S. Vasu, and R. K. Hanson. Shock tube study of soot formation in rich heptane/oxygen mixtures with dme/acetone/butanal/3-pentanone additives. *Proc. Comb. Inst.*, 32:submitted, 2008.

[78] S. Honnet, K. Seshadri, N. Peters, and U. Niemann. Experimental and chemical-kinetic modeling study of combustion of kerosene and its surrogate in laminar nonpremixed flows. *Proc. Comb. Inst.*, 32:submitted, 2008.

[79] D. C. Horning. *A Study of the High Temperature Autoignition and Thermal Decomposition of Hydrocarbons*. PhD thesis, Stanford University, 2001.

[80] Y. Huang, C.J. Sung, and J.A. Eng. Laminar flame speeds of primary reference fuels and reformer gas mixtures. *Comb. Flame*, 139:239–251, 2004.

[81] F. Inal and S. M. Senkan. Effects of equivalence ratio on species and soot concentrations in premixed n-heptane flames. *Comb. Flame*, 131:16–28, 2002.

[82] K. A. Jensen, J. M. Suo-Antilla, and L. G. Blevins. Characterization of soot properties in two-meter JP-8 pool fires. Technical Report SAND2005-0337, Sandia National Laboratories, 2005.

[83] K. A. Jensen, J. M. Suo-Antilla, and L. G. Blevins. Measurement of soot morphology, chemistry, and optical properties in the visible and near-infrared spectrum in the flame zone and overfire region of large JP-8 pool fires. *Combust. Sci. Tech.*, 179:2453–2487, 2007.

[84] S. Jerzembeck, N. Peters, P. Pepiot-Desjardins, and H. Pitsch. Laminar burning velocities at high pressure for primary reference fuels and gasoline: Experimental and numerical investigation. *Comb. Flame*, submitted, 2008.

[85] R. J. Johnston and J. T. Farrell. Laminar burning velocities and markstein lengths of aromatics at elevated temperature and pressure. *Proc. Comb. Inst.*, 30:217–224, 2005.

[86] G. Jomaas, X. L. Zheng, D. L. Zhu, and C. K. Law. Experimental determination of counterflow ignition temperatures and laminar flame speeds of c2c3 hydrocarbons at atmospheric and elevated pressures. *Proc. Comb. Inst.*, 30:193–200, 2005.

[87] J. Jones, G. B. Backsay, and J. C. Mackie. Decomposition of the benzyl radical: quantum chemical and experimental (shock tube) investigations of reaction pathways. *J. Phys. Chem. A*, 101:7105–7113, 1997.

[88] A. Kazakov and M Frenklach. Dynamic modeling of soot particle coagulation and aggregation: Implementation with the method of moments and application to high-pressure laminar premixed flames. *Comb. Flame*, 114:484–501, 1998.

[89] A. Kazakov, H. Wang, and M Frenklach. Detailed modeling of soot formation in laminar premixed ethylene flames at a pressure of 10 bar. *Comb. Flame*, 100:111–120, 1995.

[90] H. Kellerer, A. Muller, H. J. Bauer, and S. Witting. Soot formation in a shock tube under elevated pressure conditions. *Comb. Sci. Tech.*, 113:67–80, 1996.

[91] J. H. Kiefer, S. Santharam, N. K. Srinivasan, R. S. Tranter, S. J. Klippenstein, and M. A. Oehlschlaeger. Dissociation, relaxation, and incubation in the high temperature pyrolysis of ethane, and a successful rrkm modeling. *Proc. Comb. Inst.*, 30:1129–1135, 2005.

[92] V. V. Kislov, N. I. Islamova, A. M. Kolker, S. H. Lin, and A. M. Mebel. Hydrogen abstraction acetylene addition and diels-alder mechanisms of pah formation: A detailed study using first principles calculations. *J. Chem. Theory Comput.*, 1:908–924, 2005.

[93] V. V. Kislov and A. M. Mebel. The formation of naphthalene, azulene, and fulvalene from cyclic c_5 species in combustion: An ab initio/rrkm study of 9-h-fulvalenyl (c_5h_5-c_5h_4) radical rearrangements. *J. Phys. Chem. A*, 111:9532–9543, 2007.

[94] T. H. kLay, L. N. Krasnoperov, C. A. Venanzi, J. W. Bozzelli, and N. V. Shokhirev. *J. Phys. Chem.*, 100:8240–8249, 1996.

[95] S. J. Klippenstein, L. B. Harding, and Y. Georgievskii. On the formation and decomposition of c_7h_8. *Proc. Comb. Inst.*, 31:221–229, 2007.

[96] V. G. Knorre, D. Tanke, TH. Thienel, and H. Gg. Wagner. Soot formation in the pyrolysis of benzene/acetylene and acetylene/hydrogen mixtures at high carbon contentrations. *Proc. Comb. Inst*, 26:2303–2310, 1996.

[97] V. D. Knyazev and I. R. Slagle. Kinetics of the reaction between propargyl radical and acetylene. *J. Phys. Chem. A*, 106:5613–5617, 2002.

[98] U. O. Köylü, G. M. Faeth, T. L. Farias, and M. G. Carvalho. Fractal and projected structure properties of soot aggregates. *Combust. Flame*, 100:621–633, 1995.

[99] L. N. Krasnoperov and J.V. Michael. Shock tube studies using a novel multipass absorption cell: rate constant resilts for $oh + h_2$ and $oh + c_2h_6$. *J. Phys. Chem. A*, 26:5643–5648, 2004.

[100] F. E. Kruis, K. A. Kusters, S. E. Pratsinis, and B. Scarlett. A simple model for the evolution of the characteristics of aggregate particles undergoing coagulation and sintering. *Aerosol Sci. Technol.*, 19:514–526, 1993.

[101] K. Kumar, J. E. Freeh, C. J. Sung, and Y. Huang. Laminar flame speeds of preheated iso-octane/o_2/n_2 and n-heptane/o_2/n_2 mixtures. *J. Prop. Power*, 23:428–436, 2007.

[102] A. Laskin and H Wang. On initiation reactions of acetylene oxidation in shock tubes. a quantum mechanical and kinetic modeling study. *Chem. Phys. Letters*, 303:43–49, 1999.

[103] A. Laskin, H. Wang, and C. K. Law. Detailed kinetic modeling of 1,3-butadiene oxidation at high temperatures. *Int. J. Chem. Kinet.*, 32:589–614, 2000.

[104] M. Lattuada, H. Wu, and M. Morbidelli. A simple model for the structure of fractal aggregates. *J. Colloid Interf. Sci.*, 268:106–120, 2003.

[105] C. Lee, W. Yang, and R. G. Parr. *Phys. Rev. B*, 37:785–, 1988.

[106] C. Libby, D. F. Davidson, and R. K. Hanson. A shock tube study of the oxidation of 1,3-butadiene. In *42nd AIAA Aerospace Sciences Meeting and Exhibit, Reno, Nevada, Jan. 5-8*, 2004.

[107] B. Ludwig, W. Brandt, G. Friedrichs, and F. Temps. Kinetics of the reaction $c_2h_5 + ho_2$ by time-resolved mass spectrometry. *J. Phys. Chem. A*, 110:3330–3337, 2006.

[108] D. L. Marchisio and R. O. Fox. Solution of population balance equations using the direct quadrature method of moments. *J. Aerosol Sci.*, 36:43–73, 2005.

[109] N. M. Marinov, W. J. Pitz, C. K. Westbrook, M. J. Castaldi, and S. M. Senkan. Modeling of aromatic and polycyclic aromatic hydrocarbon formation in premixed methane and ethane flames. *Comb. Sci. Tech.*, 116:211–287, 1996.

[110] N. D. Marsh and M. J. Wornat. *Proc. Comb. Inst.*, 28:2585–2592, 2000.

[111] F. Mauss, B. Trilken, J. Breitbach, and N Peters. Soot formation in partially premixed diffusion flames at atmospheric pressue. In H. Bockhorn, editor, *Soot Formation in Combustion-Mechanism and Models*, pages 325–349. Springer-Verlag, 1994.

[112] C. S. McEnally, L. D. Pefferle, B. Atakan, and K. Kohse-Hinghaus. Studies of aromatic hydrocarbon formation mechanisms in flames: Progress towards closing the fuel gap. *Prog. Energy. Comb. Science*, 32:247–294, 2006.

[113] C. S. McEnally and L. D. Pfefferle. Improved sooting tendency measurements for aromatic hydrocarbons and their implications for naphthalene formation pathways. *Comb. Flame*, 148:210–222, 2007.

[114] P. Meakin. The vold-sutherland and eden models of cluster formation. *J. Colloid Interface Sci.*, 96:415–424, 1983.

[115] A. M. Mebel, M. C. Lin, T. Yu, and K Morokuma. Theoretical study of potential energy surface and thermal rate constants for the c6h5 + h2 and c6h6 + h reactions. *J. Phys. Chem. A*, 101:3189–3196, 1997.

[116] R. M. Metzger, C. S. Kuo, and E. S. Arafat. *J. Chem. Therm.*, 15:841–, 1983.

[117] J. A. Miller and S. J. Klippenstein. The recombination of propargyl radicals and other reactions on a c6h6 potential. *J. Phys. Chem. A*, 107:7783–7799, 2003.

[118] J. A. Miller and S. J. Klippenstein. The $h + c_2h_2(+m) \leftrightarrows c_2h_3(+m)$ and $h + c_2h_4(+m) \leftrightarrows c_2h_5(+m)$ reactions: electronic struture, variational transition-state theory, and solutions to a two-dimensional master equation. *Phys. Chem. Chem. Phys.*, 6:1192–1202, 2004.

[119] J. A. Miller, S. J. Klippenstein, and S. H. Robertson. A theoretical analysis of the reaction between ethyl and molecular oxygen. *Proc. Comb. Inst.*, 28:1479–1486, 2000.

[120] S. J. Miller, J. A.and Klippenstein. From the multiple-well master equation to phenomenological rate coefficients: reactions on a c_3h_4 potential energy surface. *J. Phys. Chem. A*, 107:2680–26920, 2003.

[121] S. J. Miller, J. A.and Klippenstein. The addition of hydrogen atoms to diacetylene and the heats of formation of $i - c_4h_3$ and $n - c_4h_3$. *J. Phys. Chem. A*, 109:4285–4295, 2005.

[122] S. J. Miller, J. A.and Klippenstein and S. H. Robertson. Theoretical analysis of the reaction between vinyl and acetylene: quantum chemistry and solution of the master equation. *J. Phys. Chem. A*, 104:7525–7536, 2000.

[123] P. Mitchell and M. Frenklach. Monte carlo simulation of soot aggregation with simultaneous surface growth - why primary particles appear spherical. *Proc. Comb. Inst.*, 27:1507–1514, 1998.

[124] P. Mitchell and M. Frenklach. Particle aggregation with simultaneous surface growth. *Phys. Rev. E*, 67:061407–1–061407–11, 2003.

[125] N. W. Moriarty, N. J. Borwm, and M. Frenklach. *J. Phys. Chem. A*, 103:7127–7135, 1999.

[126] N. W. Moriarty and M. Frenklach. Ab initio study of naphthalene formation by addition of vinylacetylene to phenyl. *Proc. Comb. Inst.*, 28:2563–2568, 2000.

[127] M. E. Mueller, G. Blanquart, and H. Pitsch. A joint volume-surface model of soot aggregation with the method of moments. *Proc. Comb. Inst.*, 32:submitted, 2008.

[128] Y. Murakami, K. Mitsui, K. Naito, T. Itoh, T. Kobayashim, and N. Fujii. Kinetics and oxidation mechanism of cyclopentadiene behind the shock waves. *Shock Waves*, 13:149–154, 2003.

[129] Y. Murakami, T. Saejung, C. Ohashi, and N. Fujii. Investigation of a new pathway forming naphthalene by the recombination reaction of cyclopentadienyl radicals. *Chem. Letters*, 12:1112–1113, 2003.

[130] Y. Nagano. *J. Chem. Therm.*, 33:377–388, 2001.

[131] Y. Nagano. *J. Chem. Therm.*, 34:377–383, 2002.

[132] K. G. Neoh, J. B. Howard, and A. F. Sarofim. *Soot Oxidation in Flames.* Plenum Press, New York, 1981.

[133] T. L. Nguyen, J. Peeters, and L. Vereecken. Theoretical reinvestigation of the o + c_6h_6 reaction: Quantum chemical and statistical rate calculations. *J. Phys. Chem. A*, 111:3836–3859, 2007.

[134] T. L. Nguyen, L. Vereecken, X. J. Hou, M. T. Nguyen, and J. Peeters. Potential energy surfaces, product distributios, and thermal rate coefficients of the reaction of o with c_2h_4: a comprehensive theoretical study. *J. Phys. Chem. A*, 33:7489–7499, 2005.

[135] M. A. Oehlschlaeger, D. F. Davidson, and R. K. Hanson. High-temperature thermal decomposition of benzyl radicals. *J. Phys. Chem. A*, 110:6649–6653, 2006.

[136] M. A. Oehlschlaeger, D. F. Davidson, and R. K. Hanson. Investigation of the reaction of toluene with molecular oxygen in shock-heated gases. *Comb. Flame.*, 147:195–208, 2006.

[137] M. A. Oehlschlaeger, D. F. Davidson, R. K. Hanson, W. Tsang, H. Hippler, and J. Troe. High temperature ethane and propane decomposition. *Proc. Comb. Inst.*, 30:1119–1127, 2005.

[138] V. Oja and E. M. Suuberg. *J. Chem. Eng. Data*, 43:486–492, 1998.

[139] D. B. Olson and J. C. Pickens. The effects of molecular structure on soot formation ii. diffusion flames. *Comb. Flame*, 62:43–60, 1985.

[140] A. H. Park and S. N. Rogak. A one-dimensional model for coagulation, sintering, and surface growth of aerosol agglomerates. *Aerosol Sci. Technol.*, 37:947–960, 2003.

[141] R. I. A. Patterson and Kraft M. Models for the aggregate structure of soot particles. *Comb. Flame*, 151:160–172, 2007.

[142] C. Pels Leusden. *Experimentelle und Theoretische Untersuchung der Russbildung in Laminaren Gegenstromdiffusionsflammen.* PhD thesis, RWTH Aachen, 2001.

[143] C. Pels Leusden and N. Peters. Experimental and numerical analysis of the influence of oxygen on soot formation in laminar counterflow flames of acetylene. *Proc. Comb. Inst.*, 28:2619–2625, 2000.

[144] G. Pengloan. *A Kinetic Study of Several Aromatic Coumpounds Oxidation : Applied to Pollutants Formation in Car Engines.* PhD thesis, 2001.

[145] P. Pepiot-Desjardins and H. Pitsch. An efficient error propagation based reduction method for large chemical kinetic mechanisms. *Comb. Flame*, accepted, 2008.

[146] L. R. Petzold. A differential/algebraic system solver. Technical Report SAND82-8637, Sandia National Laboratories, 1982.

[147] H. Pitsch. FlameMaster, a C++ computer program for 0D combustion and 1D laminar flame calculations.

[148] H. Pitsch, E. Riesmeir, and N. Peters. Unsteady flamelet modeling of soot formation in turbulent diffusion flames. *Comb. Science Tech.*, 158:389–406, 2000.

[149] K. S. Pitzer. *J. Am. Chem. Soc.*, 68:2209–2212, 1946.

[150] K. S. Pitzer and W. D. Gwinn. *J. Chem. Phys.*, 10:428–440, 1942.

[151] S. E. Pratsinis. Simultaneous nucleation, condensation, and coagulation in aerosol reactors. *J. Colloid Interface Sci.*, 124:416–428, 1988.

[152] E. Prosen, R. Gilmont, and F. Rossini. *J. Res. NBS*, 34:65–70, 1945.

[153] Z. Qin, H. Yang, and W. C. Jr. Gardiner. Measurement and modeling of shock-tube ignition delay for propene. *Comb. Flame*, 124:246–254, 2001.

[154] H Richter, O. A. Mazyar, R. Sumathi, W. H. Green, J. B. Howard, and J. W. Bozzelli. Detailed kinetic study of the growth of small polycycli aromatic hydrocarbons. 1. 1-naphthyl + ethyne. *J. Phys. Chem. A*, 105:1561–1573, 2001.

[155] M. J. A. Rickard, J. M. Hall, and E. L. Petersen. Effect of silane addition on acetylene ignition behind reflected shock waves. *Proc. Comb. Inst.*, 30:1915–1923, 2005.

[156] K. Roy. *Kinetische Untersuchung zur Hochtemperaturpyrolyse und -oxidation von Cyclopentadien un Cyclopentadienyl mit Hilfe der Stosswellentechnik*. PhD thesis, DLR, 1999.

[157] G. Rozenchan, D. L. Zhu, C. K. Law, and S. D. Tse. Outward propagation, burning velocities, and chemical effects of methane flames up to 60 atm. *Proc. Comb. Inst.*, 29:1461–1469, 2002.

[158] J. Sancho-Garcia and A. Perez-Jimenez. *J. Phys. B: At. Mol. Opt. Phys.*, 35:1509–1523, 2002.

[159] H.J. Schmid, S. Tejwani, C. Artelt, and W. Peukert. Monte carlo simulation of aggregate morphology for silmutaneous coagulation and sintering. *J. Nanopart. Res.*, 6:613–626, 2004.

[160] M Schmitt, C. Ratzer, C. Jacoby, and W. Leo Meerts. *J. Mol. Struct.*, 742:123–130, 2005.

[161] M. Schuetz, C. A.and Frenklach. Nucleation of soot: Molecular dynamics simulations of pyrene dimerization. *Proc. Comb. Inst.*, 29:2307–2314, 2002.

[162] A. P. Scott and L. Radom. *J. Phys. Chem.*, 100:16502–16513, 1996.

[163] D. J. Seery and C. T. Bowman. An experimental and analytical study of methane oxidation behind shock waves. *Comb. Flame*, 14:37–47, 1970.

[164] J. H. Seinfeld. Wiley & Sons, 2006.

[165] R. Seiser, L. Truett, D. Trees, and K. Seshadri. Structure and extinction of non-premixed n-heptane flames. *Proc. Comb. Inst.*, 27:649–657, 1998.

[166] J. P. Senosiain, , S. J. Klippenstein, and J.A. Miller. Oxidation pathways in the reaction of diacetylene with oh radicals. *Proc. Comb. Inst.*, 31:185–192, 2007.

[167] J. P. Senosiain, S. J. Klippenstein, and J. A. Miller. The reaction of acetylene with hydroxyl radicals. *J. Phys. Chem. A*, 17:6045–6055, 2005.

[168] J. P. Senosiain, S. J. Klippenstein, and J. A. Miller. Pathways and rate coefficients for the decomposition of vinoxy and acetyl radicals. *J. Phys. Chem. A*, 17:5772–5781, 2006.

[169] J. P. Senosiain, S. J. Klippenstein, and J. A. Miller. Reaction of ethylene with hydroxyl radicals: a theoreticl study. *J. Phys. Chem. A*, 21:6960–6970, 2006.

[170] J. P. Senosiain and J. A. Miller. The reaction of n- and i-c4h5 radicals with acetylene. *J. Phys. Chem. A*, 111:3740–3747, 2007.

[171] T. Seta, M. Nakajima, and A. Miyoshi. High-temperature reactions of oh radicals with benzene and toluene. *J. Phys. Chem. A*, 110:5081–5090, 2006.

[172] R. A. Shandross, J. P. Longwell, and J. B. Howard. Noncatalytic thermocouple coating for low-pressure flames. *Comb. Flame*, 85:282–284, 1991.

[173] C. Sheng and J. W. Bozzelli. Ab initio molecular orbital and density functional analysis of acetylene plus o_2 reactions with chemkin evaluation. *Int. J. Chem. Kinet.*, 32:623–641, 2000.

[174] A. A. Shestov, K. V. Popov, I. R. Slagle, and V. D. Knyazev. Kinetics of the reaction between vinyl radical and ethylene. *Chem. Phys. Letters*, 408:339–343, 2005.

[175] J. Singh, M. Blathasar, M. Kraft, and W. Wagner. Stochastic modeling of soot particle size and age distributions in laminar premixed flames. *Proc. Comb. Inst.*, 30:1457–1465, 2005.

[176] J. Singh, R. I. A. Patterson, M. Kraft, and H. Wang. Numerical simulation and sensitivity analysis of detailed soot particle size distribution in laminar premixed ethylene flames. *Combust. Flame*, 145:117–127, 2006.

[177] A. W. Slayden and J. F. Liebman. *Chem. Rev.*, 101:1541–1566, 2001.

[178] G. P. Smith, D. M. Golden, F. Frenklach, N. W. Moriarty, B. Eiteneer, M. Goldenberg, C. T. Bowman, R. K. Hanson, S. Song, W. C. Jr. Gardiner, V. V. Lissianski, and Z. Qin. http://www.me.berkeley.edu/grimech/.

[179] W. V. Steele, R. D. Chirico, A. Nguyen, I. A. Hossenlopp, and N. K. Smith. *Am. Inst. Chem. Eng. Symp. Ser(AIChE Symp. Ser)*, pages 138–, 1990.

[180] S.I. Stoliarov, V.D. Knyazev, and I.R. Slagle. Computational study of the mechanism and product yields in the reaction systems $c_2h_3 + ch_3 \leftrightarrows c_3h_6 \leftrightarrows h + c_3h_5$ and $c_2h_3 + ch_3 \rightarrow ch_4 + c_2h_2$. *J. Phys. Chem. A*, 106:6952–6966, 2002.

[181] A. Streitwieser. *Molecular orbital theory for Organic Chemists*. Willey, New York, 1961.

[182] I. V. Tokmakov and M. C. Lin. Kinetics and mechanism of the oh+c6h6 reaction: A detailed analysis first first-principles calculations. *J. Phys. Chem. A*, 106:11309–11326, 2002.

[183] I. V. Tokmakov and M. C. Lin. Combined quantum chemical/RRKM-ME computational study of the phenyl + ethylene, vinyl + benzene, and h + styrene reactions. *J. Phys. Chem. A*, 108:9697–9714, 2004.

[184] I. V. Tokmakov, L. V. Moskaleva, and M. C. Lin. Quantum chemical/vrrkm study on the thermal decomposition of cyclopentadiene. *Int. J. Chem. Kin.*, 36:139–151, 2003.

[185] A. Tregrossi, A. Ciajolo, and R. Barbella. The combustion of benzene in rich premixed flames at atmospheric pressure. *Comb. Flame*, 117:553–561, 1999.

[186] M. S. Tsurikov, K. P. Geigle, V. Kruger, Y. Schneider-Kuhnle, W. Stricker, R. Luckerath, R. Hadef, and M. Aigner. Laser-based investigation of soot formation in laminar premixed flames at atmospheric and elevated pressures. *Comb. Sci. Tech.*, 117:1835–1862, 2005.

[187] A. Tsuzuki, T. Uchimaru, K. Matsumura, M. Mikami, and K. Tanabe. *J. Chem. Phys.*, 110:2858–2861, 1999.

[188] C. M. Vagelopoulos and F. N. Egolfopoulos. Direct experimental determination of laminar flame speeds. *Proc. Comb. Inst.*, 27:513–519, 1998.

[189] A. van Maaren, D. S. Thung, and L. P. H. Degoey. Measurement of flame temperature and adiabatic burning velocity of methane/air mixtures. *Comb. Sci. Tech.*, 96:327–344, 1994.

[190] V. Vasudevan, D. F. Davidson, and R. K. Hanson. Shock tube measurements of toluene ignition times and oh concentration time histories. *Proc. Comb. Inst.*, 30:1155–1163, 2005.

[191] A. Violi. Modeling of soot particle inception in aromatic and aliphatic premixed flames. *Comb. Flame*, 139:279–287, 2004.

[192] A. Violi, A. F. Sarofim, and G. A. Voth. Kinetic monte carlo-molecular dynamics approach to model soot inception. *Comb. Science Tech.*, 176:991–1005, 2004.

[193] C. Vovelle. personal communication, 2008.

[194] H Wang. A new mechanism for initiation of free-radical chain reactions during high-temperature, homogeneous oxidation of unsaturade hydrocarbons: ethylene, propyne and allene. *Int. J. Chem. Kinet.*, 33:698–706, 2001.

[195] H. Wang and K. Brezinsky. Computational study on the thermochemistry of cyclopentadiene derivatives and kinetics of cyclopentadienone thermal decomposition. *J. Phys. Chem. A*, 102:1530–1541, 1998.

[196] H. Wang and M. Frenklach. Enthalpies of formation of benzenoid aromatic molecules and radicals. *J. Phys. Chem.*, 97:3867–3874, 1993.

[197] H. Wang and M. Frenklach. Calculations of rate coefficient for the chemically activated reactions of acetylene with vinylic and aromatic radicals. *J. Phys. Chem.*, 98:11465–11489, 1994.

[198] H. Wang and M. Frenklach. A detailed kinetic modeling study of aromatics formation in laminar-premixed acetylene and ethylene flames. *Comb. Flame*, 110:173–221, 1997.

[199] NIST chemistry webbook. http://webbook.nist.gov/chemistry.

[200] D. Wong and M. Schuetz, C. A.and Frenklach. Modelling particle shape and composition of soot particles in laminar premixed flames. *International Workshop on Combustion Generated Fine Carbon Particles*, 2007.

[201] D. Wong and M. Schuetz, C. A.and Frenklach. Molecular dynamics simulations of PAH dimerization. *International Workshop on Combustion Generated Fine Carbon Particles*, 2007.

[202] F. Xu, P. B. Sunderland, and G. M. Faeth. Soot formation in laminar premixed ethylene/air flames at atmospheric pressure. *Combust. Flame*, 108:471–493, 1997.

[203] Z. F. Xu and M. C. Lin. Ab initio kinetics for the unimolecular reaction $c_6h_5oh \rightarrow co + c_5h_6$. *J. Phys. Chem. A*, 110:1672–1677, 2006.

[204] B. Zhao, K. Uchikawa, and H Wang. A comparative study of nanoparticles ion premixed flames by scanning mobility particle sizer, small angle neutron scattering, and transmission electron microscopy. *Proc. Comb. Inst.*, 31:851–860, 2007.

[205] B. Zhao, Z. Yang, M. V. Johnston, H Wang, A. S. Wexler, M. Balthasar, and M. Kraft. Measurements and numerical simulation of soot particle size distribution functions in a laminar premixed ethylene-oxygen-argon flame. *Comb. Flame*, 133:173–188, 2003.

[206] B. Zhao, Z. Yang, Z. Li, , M. V. Johnston, and H Wang. Particle size distribution function of incipient soot in laminar premixed ethylene flames: effet of flame temperature. *Proc. Comb. Inst.*, 30:1441–1448, 2005.

[207] X. Zhong and J. W. Bozzelli. Thermochemical and kinetic analysis on the addition reactions of h, o, oh, and ho_2 with 1,3 cyclopentadiene. *Int. J. Chem. Kinet.*, 29:893–913, 1997.

[208] X. Zhong and J. W. Bozzelli. Thermochemical and kinetic analysis of the h, oh, ho_2, o, and o_2 association reactions with cyclopentadienyl radical. *J. Phys. Chem.*, 20:3537–3555, 1998.

[209] R. S. Zhu, Z. F. Xu, and M. C. Lin. Ab initio studies of alkyl radical reactions: comnination and disproportioanation reacstion of ch_3 with c_2h_5, and the decomposition of chemically activated c_3h_8. *J. Chem. Phys.*, 120:6566–6573, 2004.

[210] A. Zucca, D. L. Marchisio, A. A. Barressi, and R. O. Fox. Implementation of the population balance equation in CFD codes for modelling soot formation in turbulent flames. *Chem. Eng.Sci.*, 61:87–95, 2006.